# **Springer Theses**Recognizing Outstanding Ph.D. Research

Matthias Kühne

# Lithium Intercalation in Bilayer Graphene Devices



# **Springer Theses**

Recognizing Outstanding Ph.D. Research

### Aims and Scope

The series "Springer Theses" brings together a selection of the very best Ph.D. theses from around the world and across the physical sciences. Nominated and endorsed by two recognized specialists, each published volume has been selected for its scientific excellence and the high impact of its contents for the pertinent field of research. For greater accessibility to non-specialists, the published versions include an extended introduction, as well as a foreword by the student's supervisor explaining the special relevance of the work for the field. As a whole, the series will provide a valuable resource both for newcomers to the research fields described, and for other scientists seeking detailed background information on special questions. Finally, it provides an accredited documentation of the valuable contributions made by today's younger generation of scientists.

# Theses are accepted into the series by invited nomination only and must fulfill all of the following criteria

- They must be written in good English.
- The topic should fall within the confines of Chemistry, Physics, Earth Sciences, Engineering and related interdisciplinary fields such as Materials, Nanoscience, Chemical Engineering, Complex Systems and Biophysics.
- The work reported in the thesis must represent a significant scientific advance.
- If the thesis includes previously published material, permission to reproduce this must be gained from the respective copyright holder.
- They must have been examined and passed during the 12 months prior to nomination.
- Each thesis should include a foreword by the supervisor outlining the significance of its content.
- The theses should have a clearly defined structure including an introduction accessible to scientists not expert in that particular field.

More information about this series at http://www.springer.com/series/8790

# Matthias Kühne

# Lithium Intercalation in Bilayer Graphene Devices

Doctoral Thesis accepted by the Max Planck Institute for Solid State Research, Stuttgart, Germany



Author
Dr. Matthias Kühne
Max Planck Institute for Solid State
Research
Stuttgart, Germany

Supervisor
Dr. Jurgen H. Smet
Max Planck Institute for Solid State
Research
Stuttgart, Germany

ISSN 2190-5053 ISSN 2190-5061 (electronic) Springer Theses ISBN 978-3-030-02365-2 ISBN 978-3-030-02366-9 (eBook) https://doi.org/10.1007/978-3-030-02366-9

Library of Congress Control Number: 2018962121

#### © Springer Nature Switzerland AG 2018

This work is subject to copyright. All rights are reserved by the Publisher, whether the whole or part of the material is concerned, specifically the rights of translation, reprinting, reuse of illustrations, recitation, broadcasting, reproduction on microfilms or in any other physical way, and transmission or information storage and retrieval, electronic adaptation, computer software, or by similar or dissimilar methodology now known or hereafter developed.

The use of general descriptive names, registered names, trademarks, service marks, etc. in this publication does not imply, even in the absence of a specific statement, that such names are exempt from the relevant protective laws and regulations and therefore free for general use.

The publisher, the authors and the editors are safe to assume that the advice and information in this book are believed to be true and accurate at the date of publication. Neither the publisher nor the authors or the editors give a warranty, express or implied, with respect to the material contained herein or for any errors or omissions that may have been made. The publisher remains neutral with regard to jurisdictional claims in published maps and institutional affiliations.

This Springer imprint is published by the registered company Springer Nature Switzerland AG The registered company address is: Gewerbestrasse 11, 6330 Cham, Switzerland

# **Supervisor's Foreword**

Since the discovery of graphene, there has been a surge in activity on two-dimensional (2D) layered materials. A whole field of science has emerged, with researchers vigorously investigating their production, characterization, and application. It has become feasible to handle and manipulate individual atomic sheets of many such materials as well as to integrate them into functional devices. In recent years, this has allowed the exploration of new avenues in physics, chemistry, and materials science. Yet processes at the nanometer scale easily transcend borders between traditional academic fields. Innovative interdisciplinary approaches are therefore required, which may in their own right open up entirely new perspectives.

As a matter of fact, layered materials consist of atomic planes held together by van der Waals forces. Due to the weak nature of these forces, however, interlayer gaps remain. These deserve closer attention as they allow for the insertion and storage of ionic species (intercalation). This aspect is highly intriguing from a fundamental point of view, since ion insertion affects many properties of the host material in a non-trivial manner. Yet in a straightforward fashion, it may be exploited for electrochemical energy storage. In current Li-ion batteries, graphite is widely used as negative electrode material. It is reversibly intercalated with Li-ions during charge—discharge cycles. Despite such a large-scale application, only very few experiments have been dedicated to controlling and probing intercalation at the level of single-crystalline host materials consisting of only few atomic sheets. With the advent of exfoliation of a single or a few layers of 2D materials, these have now come within reach.

In this book, Matthias Kühne summarizes successful first investigations on the Li-intercalation of bilayer graphene. Two graphene sheets stacked upon each other provide only one gap to host guest ions. It thus represents the smallest conceivable 2D system for the study of intercalation chemistry. Today, high-quality bilayer graphene single crystals are easily available in the laboratory. Matthias Kühne succeeded in selectively integrating these into a miniaturized electrochemical cell architecture, obtaining electric gate control over the intercalation process. An ion-mediating substance (electrolyte) was implemented such as to connect a nanostructured bilayer graphene device with a lithium metal counter electrode,

without fully covering the former. Magnetotransport techniques established in the field of low-dimensional electron physics were then deployed to reveal the impact of Li-ions residing between the carbon sheets. Not only do they transfer a noticeable amount of charge to the electronic states of the adjacent graphene sheets, they also act as scattering centers for electrons. Within the detection limit of the experiments, Li-ions were further shown to reside exclusively between graphene sheets. There, they diffuse faster than in bulk graphite and even faster than sodium chloride (common salt) in water. This record chemical diffusion coefficient for Li could be directly extracted from time-dependent measurements of the Hall effect. A complementary set of experiments, performed both in-situ and ex-situ, corroborates these findings.

This thesis puts forward a creative new approach to investigate and exploit intercalation chemistry. Combining electrochemical means with the machinery of solid-state nanophysics, important steps are made toward the controlled insertion of ions in a 2D system. Although this work focuses on bilayer graphene, the procedures described are directly transferable to other 2D materials or van der Waals heterostructures. The proposed device architecture also opens doors to the application of local probe techniques that cannot be used in the study of bulk systems. In future, these may yield direct insights into intercalation-induced phenomena down to the atomic scale. Together with experiments discussed here, they will foster our understanding of ion transport and storage in 2D materials. Differences with respect to bulk systems clearly seem to exist, but further research is needed for their full identification and potential exploitation.

Stuttgart, Germany September 2018 Dr. Jurgen H. Smet

# **Abstract**

The implementation of a novel electrochemical cell architecture consisting of a solidified polymer electrolyte confined at and covering only a small part of the perimeter of a patterned bilayer graphene device has enabled the operation of bilayer graphene as a mixed (electronic and ionic) conductor.

The gate-controlled reversible intercalation of Li-ions into bilayer graphene was demonstrated on the basis of in situ measurements of both the charge carrier transport and the Raman scattering response. Due to charge transfer from the intercalant to the electronic states of bilayer graphene, the longitudinal resistivity  $\rho_{xx}$  of the latter changes in a characteristic manner as the system gets more electron-doped. For the Fermi energy  $\epsilon_F$  lying in the conduction band,  $\rho_{xx}$  drops continuously as the Li-density  $n_{\text{Li}}$  increases. A concomitant blueshift of the Raman G band could be demonstrated, consistent with experiments performed on electrostatically gated bilayer graphene devices. Independent evidence for successful Li-intercalation was extracted from low-temperature magnetotransport measurements of weak localization. This quantum interference effect proves sensitive to an increase in the elastic intervalley scattering rate  $\tau_i^{-1}$ , induced by intercalating Li-ions. Note that this enhancement proves equally reversible upon delithiation as the aforementioned effects.

We commonly observe the open edges of successfully intercalated bilayer graphene devices to be decorated with Li-rich material. Attributing these decorations to immobilized reaction products of the highly reactive intercalant, we exploit the implications of this finding to identify efficient Li-diffusion pathways. We determine Li-ions to reside in between graphene sheets only, since diffusion in bilayer graphene stops at natural junctions with single-layer graphene and characteristic edge decorations emerge at inner edges of macroscopic holes etched within a bilayer graphene device.

We employ time-dependent in situ Hall transport measurements that reflect the density of intercalated lithium  $n_{\rm Li}$  via the amount of electrons induced through charge transfer. A time-base synchronized measurement of  $n_{\rm Li}$  at different positions along an elongated bilayer provides unprecedented direct access to the intercalant

viii Abstract

diffusion kinetics due to the directionality of the device layout. Employing a numerical solution to Fick's second law, we extract for the first time the chemical diffusion coefficient  $D^{\delta}$  of Li in bilayer graphene:  $D^{\delta}$  up to  $7 \times 10^{-5} \text{cm}^2/\text{s}$  at room temperature. This exceeds all experimental values reported from room temperature studies on bulk graphite. Li-diffusion in bilayer graphene is thus greatly enhanced, indicating that this material behaves in a distinct way compared to bulk graphite. Such a conclusion could be supported by other obvious differences between both materials, such as the different dimensionality: Bilayer graphene is a 2D material, while bulk graphite retains a 3D character. This manifests especially in the characteristic stage ordering during intercalation, for which we found no evidence in bilayer graphene. Alternatively, however, the obtained record values of  $D^{\delta}$  might also point toward an intrinsically higher in-plane Li-diffusivity in bulk graphite, which is not perfectly probed in experiments. Reasons might lie in the typical use of composite electrodes as well as in the extraction of  $D^{\delta}$  from measurement on multi-crystalline samples where diffusion along the c-axis might intermix.

The device concept with a local on-chip electrochemical cell implemented here is immediately transferable to other 2D materials as well as thin films. The marriage of electrochemical cell methods with magnetotransport tools commonly deployed in the physics of low-dimensional electron systems offers access to powerful transport characterization methods previously not available in the context of ionic transport and diffusion. The immediate accessibility of the mixed conductor surface also offers the prospect of deploying local probe and surface analysis techniques to study the local kinetics and ordering of the intercalant otherwise hidden underneath the electrolyte. The device layout may thus promote a paradigm shift on the use of electrolytes in on-chip experiments.

# Acknowledgements

#### I would like to thank

Dr. Jurgen Smet for the possibility to work in his group and for his relentless support. Without his guidance and continuous optimism concerning this work, it would hardly have been as successful.

Prof. Dr. Jörg Wrachtrup for co-examining this thesis.

Prof. Dr. Jürgen Janek for co-examining this thesis.

Prof. Dr. Klaus von Klitzing for his support and enthusiasm.

Prof. Dr. Joachim Maier and Dr. Jelena Popovic for most valuable input and a fruitful collaboration. I would also like to acknowledge many discussions with (former) members of Prof. Maier's department that helped at various stages of this work, notably with Dr. Dominik Samuelis, Dr. Rotraut Merkle, and Dr. Nils Ohmer.

Dr. Pavel Ostrovsky for a fruitful collaboration and valuable insights on theory. All (former) members of Dr. Jurgen Smet's research group. Special thanks go to Dr. Federico Paolucci as he introduced the electrolyte to the group. In addition, I am furthermore especially grateful to Dr. Benedikt Friess, Patrick Herlinger, Dr. Daniel Kärcher, and Dr. Ding Zhang who helped me grow up in the group. Thanks also to Dr. Thomas Beringer, Ioannis Caltzidis, Dr. Joseph Falson, Sven Fecher, Manuel Sanchez Friedeberg, Johannes Geurs, Dr. Youngwook Kim, Pranoti Kshirsagar, Dr. Johannes Nübler, Dr. Ramu Pradip, Leila Raafat, Wafa Rouabeh, Ebrahim Sajadi, Daniela Tabrea, Dr. Yijin Zhang, and Patrik Zielinski for input in one way or another.

Steffen Wahl, Gunther Euchner, Sanela Göres, and Yvonne Link for invaluable technical support. I am grateful also for the occasional help of Manfred Schmid, Ingo Hagel, and Steffen Pischke.

Prof. Dr. Jürgen Weis as well as Bernhard Fenk, Achim Güth, Marion Hagel, Thomas Reindl, and Ulrike Waizmann for access to the clean room and support with everything related.

x Acknowledgements

Prof. Dr. Ulrich Starke and Tolga Acartürk for ToF-SIMS and discussions.

Dr. Ute Zschieschang for surface functionalization.

Ruth Jenz for all administrative help.

All other people at the Max Planck Institute for Solid State Research, a place which I experienced as a most conducive environment for working and more.

My family for unconditional support at all times.

Dominique for her love.

# **Contents**

1		oduction	1 6
2	Elec	etronic Properties	9
	2.1	Single Layer Graphene	9
	2.2		11
	2.3		14
	2.4		17
	2.5		18
	2.6	· · · · · · · · · · · · · · · · · · ·	23
	2.7		26
			28
		2.7.2 Integer Quantum Hall Effect	31
			32
	2.8		34
	2.9	· · · · · · · · · · · · · · · · · · ·	37
	Refe		38
3	Elec	etrochemical Device Setup and Fabrication	43
	3.1		43
		3.1.1 The $\text{Li}_x\text{C}_6$ System	45
		3.1.2 The Solid Electrolyte Interphase	47
	3.2	Solid Polymer Electrolyte	48
			49
			51
	3.3		53
	3.4		57
	Refe	erences	57

xii Contents

4	Lith	iation Studies	61
	4.1	In situ Electronic Transport at Zero Magnetic Field	61
	4.2	In situ Raman Spectroscopy	65
	4.3	In situ Magnetotransport	70
	4.4	Low-Temperature Magnetotransport	73
	4.5	Summary	78
	Refe	rences	78
5	Con	ductivity Corrections from Quantum Interferences	81
	5.1	Quantum Interferences in Graphene Single- and Bilayers	81
		5.1.1 Quantum Interferences in Single Layer Graphene	83
		5.1.2 Quantum Interferences in Bilayer Graphene	84
	5.2	Weak Localization in Li-intercalated Bilayer Graphene	85
		5.2.1 Dephasing	89
	5.3	Summary	90
	Refe	prences	91
6	Inte	rcalate Diffusion Pathways	93
	6.1	Edge Decorations	93
	6.2	Bilayer Graphene/Single Layer Graphene Junctions	99
	6.3	Summary	101
	Refe	erences	101
7	Inte	rcalate Diffusion Kinetics	103
	7.1	Li Diffusion in Graphite	103
	7.2	Measurement Setup for Intercalate Diffusion Studies	106
	7.3	Numerical Solution to Fick's Second Law	108
	7.4	Li Diffusion Kinetics in Bilayer Graphene	110
	7.5	Summary	113
	Refe	erences	113
Aŗ	pend	ix A: Notes on the Tight-Binding Approach	115

# **Abbreviations and Symbols**

#### **Abbreviations**

2D Two-dimensional

2DES Two-dimensional electron system

3D Three-dimensional

AFM Atomic force microscopy

ARPES Angle-resolved photoemission electron spectroscopy

BEMA Bisphenol A ethoxylate dimethacrylate

BLG Bilayer graphene
BZ Brillouin zone
CE Counter electrode
CNP Charge neutrality point
DFT Density functional theory

DOS Density of states

GIC Graphite intercalation compound

hBN Hexagonal boron nitride HES Higher-energy sub-band

HOPG Highly oriented pyrolytic graphite IQHE Integer quantum Hall effect

IR Infrared spectroscopy
LES Lower-energy sub-band

LL Landau level

OCV Open-circuit voltage
OTS N-octadecyltrichlorosilane

PEGMA Poly(ethylene glycol) monomethyl ether

monomethacrylate

PMMA Poly(methyl methacrylate)

PVA Poly(vinyl alcohol)
QI Quantum interference
SdH Shubnikov–de Haas

SEI Solid electrolyte interphase

SEM Scanning electron microscopy

SLG Single-layer graphene

STS Scanning tunneling spectroscopy
TFSI Bis(trifluoromethane)sulfonimide

ToF-SIMS Time-of-flight secondary ion mass spectrometry

UCF Universal conductance fluctuation

UV Ultraviolet

WAL Weak anti-localization
WE Working electrode
WL Weak localization

### **Symbols**

A Area

a Real space lattice constant

 $a_0$  Distance between neighboring carbon atoms in graphene

 $a_1, a_2$  (Real space) lattice vectors

α Band index

 $B = |\mathbf{B}|$  Strength of the magnetic field  $\mathbf{B}$ 

 $B_*$  Magnetic field associated with intravalley chiral symmetry

breaking

 $B_{\phi}$  Magnetic field associated with phase coherence  $B_{i}$  Magnetic field associated with intervalley scattering

 $b_1, b_2$  (Reciprocal space) lattice vectors

C Capacitance

cc-axis lattice constantcParticle concentrationcSpeed of light

D (Self-) diffusion coefficient  $D^{\delta}$  Chemical diffusion coefficient

d Thickness

 $\delta$  Landau level degeneracy E = |E| Strength of the electric field E

*e* Elementary charge

€ Energy

 $\epsilon_0$  Vacuum permittivity  $\epsilon_F$  Fermi energy

 $\epsilon_r$  Relative permittivity

**F** Force

f<sub>SdH</sub> Frequency of Shubnikov–de Haas oscillations

Φ Magnetic flux

 $\Phi_0$  Magnetic flux quantum

 $\Phi_B$  Berry phase  $\gamma_0, \gamma_0, \gamma_1, \gamma_2, \gamma_3, \gamma_4$  Hopping integrals

 $h = 2\pi\hbar$  Planck constant I Electrical current J Particle flux

j Electrical current density  $k_B$  Boltzmann constant  $k_F$  Fermi wave vector

 $k_i, k_s$  Incident and scattered photon wave vectors

 $k_a, k_{a'}$  Phonon wave vectors

 $\kappa$  Wave vector with respect to  $\mathbf{K}^{(')}$ 

 $\kappa_F$  Fermi wave vector with respect to  $\mathbf{K}^{(')}$ 

L Length

 $l_*$  Intravalley chiral symmetry breaking length

 $l_{\phi}$  Phase coherence length  $l_{i}$  Intervalley scattering length

 $l_{\rm tr}$  Mean free path  $\lambda$  Laser wavelength

 $\lambda_i, \lambda_s$  Wavelengths of incident and scattered light

M Molar concentration

 $M_n$  Number average molecular weight

 $m^*$  Effective mass  $m_e$  Electron rest mass  $\mu$  Chemical potential

*μ* Mobility

 $\mu_q$  Quantum mobility

Charge carrier density

 $n_{eh}$  Density range associated with electron-hole puddles  $n_{imp}$  Charge carrier density induced by doping from impurities

 $n_{\text{Li}}$  Li-ion density v Filling factor

 $\omega_c$  Cyclotron frequency

 $\omega_i, \, \omega_s$  Incident and scattered photon frequencies

 $\omega_q, \, \omega_{q'}$  Phonon frequencies

 $\omega_{\mathcal{C}}$  Pseudospin winding number

p Pressure

 $p_F$  Fermi momentum

Q, q Charge R Gas constant R Resistance  $R_H$  Hall coefficient  $R_s$  Sheet resistance

 $R_{xx}$ ,  $R_{xy}$  Longitudinal and transverse resistance

 $\rho$ ,  $\hat{\rho}$  Resistivity (tensor)

 $\rho_{xx}$ ,  $\rho_{xy}$  Longitudinal and transverse resistivity

 $\sigma$ ,  $\hat{\boldsymbol{\sigma}}$  Conductivity (tensor)

 $\sigma_a, \sigma_c$  In-plane and out-of-plane conductivity in graphite

 $\sigma_{xx}$ ,  $\sigma_{xy}$  Longitudinal and transverse conductivity

T Temperature t Time

*t*<sub>+</sub> Lithium transference number

 $\tau_*$  Intravalley chiral symmetry breaking time

 $au_{ee}$  Electron–electron scattering time in the diffusive regime

 $au_i$  Intervalley scattering time  $au_N$  Nyquist scattering time  $au_q$  Quantum lifetime  $au_{
m tr}$  Transport time heta Contact angle heta Voltage  $heta_G$  Gate voltage

 $U_{\text{OCV}}$  Open-circuit voltage

 $U_{xx}$ ,  $U_{xy}$  Longitudinal and transverse voltage drop

 $egin{array}{ll} oldsymbol{v}, \, oldsymbol{v}_D & ext{Drift velocity} \\ oldsymbol{v}_F & ext{Fermi velocity} \\ \end{array}$ 

W Width

 $\xi$  Valley index

# Chapter 1 Introduction



1

Intercalation designates the insertion of atomic or molecular species into suitable spaces within the structure of a host material. An important class of host materials are layered, crystalline solids. Examples are graphite, hexagonal boron nitride, black phosphorous, layered chalcogenides, and sheet silicates. The atoms of these materials more strongly within each constituting layer than across the gap between neighboring layers. It is inside these gaps, named galleries, that foreign atomic or molecular species can be accommodated. Their insertion typically maintains the host material's integrity and often proves reversible. However, the uptake of guest species implies the formation of a new chemical compound. Its properties (mechanical, electrical, optical, catalytic, etc.) may differ significantly from the ones of the pristine host. Think of the swelling/shrinking of clays in wet/dry conditions, respectively. This ancient observation illustrates how drastic the impact of intercalation can be. As such, it may represent a challenge to be met. Efforts have been made, though, to harness its potential for diverse applications. Over 1000 years ago, intercalation was key to the production of eggshell china [1]. Today it is being exploited in various fields including energy storage, chemical synthesis, and catalysis. Intercalation nonetheless continues to be a fascinating topic for basic science, appealing to researchers across disciplines. The volume edited by Wittingham and Jacobson [2] may serve as a general introduction to the field, with many additional aspects covered in Refs. [3– 6].

If one were to name a truly emblematic host material for intercalation chemistry, graphite would certainly be a number one choice. Its readiness to incorporate a vast number of guest species is truly remarkable. Scientific publications on the subject can be traced back at least to the work of Schafhäutl in 1840 [7]. As of today, graphite has been reportedly intercalated with literally hundreds of different atomic and molecular species. Reasons for this exceptional character lie in its structural properties. Graphite consists of stacked sheets of carbon atoms arranged in a planar honeycomb lattice, termed graphene sheets, see Fig. 1.1a, b. In each sheet,  $\pi$ -electrons form an extended 2D electronic system with semiconducting properties and zero band

1 Introduction

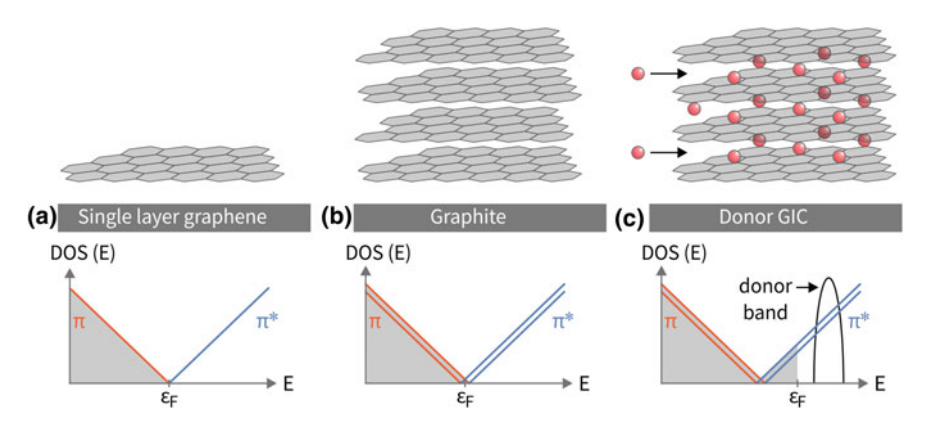


**Fig. 1.1** Schematic crystal structure (upper row) and electronic structure of **a** single layer graphene, **b** graphite, and **c** a donor graphite intercalation compound (GIC). Here, DOS(E) is the density of states as a function of energy E, and  $\epsilon_F$  is the Fermi energy.  $\pi$ -bonding ( $\pi^*$ -antibonding) states form the valence (conduction) band. Grey shaded areas in the lower row indicate filled electronic states. Red spheres represent the intercalant. Lower row adapted from Ref. [16] by permission of Oxford University Press, USA

gap [8, 9]. In Fig. 1.1a, we schematically show the electronic density of states (DOS) near the Fermi level  $\epsilon_F$  for single layer graphene. Here, the filled  $(\pi)$  valence band touches the empty  $(\pi^*)$  conduction band at a single point of vanishing DOS. Due to weak (yet finite) interlayer coupling, bulk graphite acquires a slightly modified—semimetallic—character, see Fig. 1.1b. This structure allows graphite to participate in intercalation reactions just as well as an oxidizer or as a reducer (amphoteric character). The graphene sheets themselves being particularly inert, reacted species are accommodated in the galleries between carbon layers according to the general intercalation reaction

$$xX + C_6 \longrightarrow X_x C_6. \tag{1.1}$$

In the graphite intercalation compound (GIC) thus formed, there is a transfer of charge between intercalate and graphene layers. If the species X donates (receives) electrons to (from) the graphene sheets, the GIC is termed donor-type (acceptor-type). An associated shift of the Fermi level  $\epsilon_F$  reflects the degree of this charge transfer, see Fig. 1.1c. GICs can be expected to acquire a more metallic character as DOS( $\epsilon_F$ ) increases with  $\epsilon_F$  being moved relative to its position in pristine graphite. A related increase in phase space may even lead to emergent phenomena such as superconductivity. CaC<sub>6</sub>, [10] YbC<sub>6</sub>, [10] and BaC<sub>6</sub> [11] are recent examples of GICs in which this effect has been disclosed [12]. The phenomenology one may encounter in GICs is however rich in general, a comprehensive review of which surpasses the scope of this work. The interested reader is referred to the seminal review by Dresselhaus and Dresselhaus [13] as well as the two volumes edited by Zabel and Solin [14, 15]. In addition, a textbook was presented more recently by Enoki et al. [16].

1 Introduction 3

The intercalation of graphite with lithium was first reported by Hérold in 1955 [17]. Like all alkali metals, lithium forms a donor GIC (i.e., electrons are transfered from the Li intercalate to the graphene sheets). Though initially obtained by chemical vapor transport, [17] the 1970s saw a surge in activity on the lithiation of graphite immersed in an electrolyte solution containing a dissolved Li salt. An early account on Li-intercalation *via* electrochemical reduction of graphite was then put forward by Besenhard [18]. A driving force behind these activities was the search for novel electrochemical energy storage solutions that culminated in Sony's release of the first commercial Li-ion battery in 1991. The active material of its negative electrode was (and typically still is at the time of this writing) graphite (C<sub>6</sub>), which—during charging and discharging—is reversibly intercalated with Li according to

$$xLi^{+} + xe^{-} + C_{6} \rightleftharpoons Li_{r}C_{6}, \tag{1.2}$$

with  $0 \le x \le 1$ . Here, Li-ions (Li<sup>+</sup>) are supplied *via* the electrolyte, while electrons (e<sup>-</sup>) are supplied *via* the external electrical circuit. Both ions and electrons are transported and stored inside Li<sub>x</sub>C<sub>6</sub>, which thus is a mixed conducting material. Beyond its obvious relevance for energy storage, this electrochemical route to intercalation allows for the controlled insertion of ions using an electrical power supply. Basic research has embraced this technique ever since, for instance to enable a range of in situ studies during repeated intercalation/deintercalation cycles. For the reader interested in a broader perspective on relevant electrochemical aspects, Refs. [19, 20] may serve as a starting point.

Graphene was introduced above as a single layer of carbon atoms that graphite is made of. Its properties alone fill entire books, such as the one edited by Aoki and Dresselhaus [21]. However, it was only in 2004 that a single graphene sheet could in fact be isolated from bulk graphite [22]. For this achievement, Geim and Novoselov were awarded the Nobel prize in physics in 2010. Since then, we learned to handle and investigate individual atomic sheets of many layered materials: an entire new field of research, coined 2D materials, was born. It has become even possible to recombine such sheets into so-called van der Waals heterostructures, [23] which have no analog in nature. These advances open many new prospects for intercalation research. For instance, one may study host systems of reduced size in dedicated manner, down to the fundamental limit of a single gallery. One could investigate effects induced by a controlled, relative rotation between adjacent atomic layers. Or one might explore previously entirely unaccessible systems: artificial stacks of 2D materials. All this can be combined in straight forward manner with both fabrication and investigation techniques available to the study of low-dimensional systems, such as nanolithography or local probe techniques. Throughout the last decades, also efforts for integrating electrolytes with on-chip electronics have increased [24]. First steps in exploring the intercalation of 2D materials have been made [25]. Many more can yet be done.

In this thesis, we explore the mixed conducting properties of bilayer graphene. With only one gallery between its two carbon sheets, it may be regarded as the most fundamental unit suited for intercalation studies. We implement a novel

4 1 Introduction

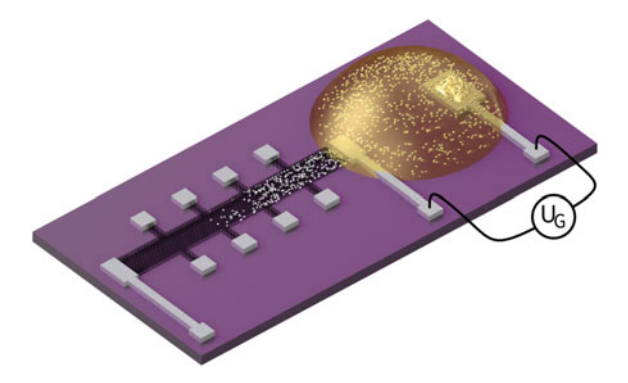


Fig. 1.2 Schematic electrochemical device design (not to scale) with bilayer graphene (black) in a Hall bar geometry on a  $SiO_2$ -terminated silicon substrate (violet). Electrodes (grey) either enable electronic transport measurements or serve as a counter electrode to control the lithiation (via the gate voltage  $U_G$ ). The electrolyte (yellow) covers the bilayer only at one end. Li-ions are represented by white spheres

electrochemical cell architecture, where the redox-reaction forcing lithium intercalation according to Eq. 1.2 is localized at one end of the bilayer, only, see Fig. 1.2. Similar to a Li-ion battery, varying the gate voltage  $U_G$  with respect to a counter electrode, applied across a Li-ion containing electrolyte, allows for the controlled lithiation/delithiation of bilayer graphene. However, unlike a practical graphitic electrode, which is typically a composite containing powdered graphite and additives such as binders, here we study one well defined single-crystalline sample at a time. The device layout schematically given in Fig. 1.2 furthermore has the following advantages:

- The geometry lends itself to the use of magnetotransport machinery known from mesoscopic low-dimensional physics. Further facilitated by current nanofabrication methods to both pattern and electrically contact individual graphene single-crystals, meaningful quantities such as the conductivity or the charge carrier density can be extracted in a straightforward manner.
- A considerable part of bilayer graphene is uncovered from the electrolyte. This
  avoids disorder the latter may induce when applied directly on top of a sensitive
  surface [26–29]. By leaving it uncovered, we prevent any potential shielding or
  deterioration of the intrinsic properties of our sample. Furthermore, local probe
  techniques else disturbed by the presence of the electrolyte may well be applied.
- The intercalate diffusion is directed. Upon local intercalation at one end of the
  device, lithium should diffuse such as to minimize concentration gradients across
  the bilayer. This diffusion should continue into the uncovered part, where the
  directionality may be exploited, for example, to extract information about the
  diffusion kinetics.

1 Introduction 5

This thesis is organized as follows:

**Chapter 2: Electronic properties** We give an introduction to relevant electronic properties and to the charge carrier transport in bilayer graphene, partially in comparison to the case of single layer graphene for instructive reasons. An understanding of bilayer graphene's intrinsic properties is necessary for revealing changes induced during lithiation/delithiation. Most of the discussion is highlighted by exemplary measurements on a bilayer graphene device.

Chapter 3: Electrochemical device setup and fabrication In the absence of studies on bilayer graphene, we introduce the phenomenology of the electrochemical lithiation of graphite. Processes are discussed that happen during lithiation both within  $\text{Li}_x \text{C}_6$  as well as at the interface with the electrolyte. We then present the polymer electrolyte used, including its properties and positioning capabilities. The fabrication of bilayer graphene devices studied in this work (as in Fig. 1.2) is explained thereafter.

**Chapter 4: Lithiation studies** We perform in situ measurements of the charge carrier transport in bilayer graphene devices as well as of their Raman scattering response during gate-controlled electrochemical lithiation/delithiation cycles. From these, we provide evidence for the reversible intercalation of Li-ions and their diffusion into the uncovered area of bilayer graphene. We furthermore discuss a magnetotransport study of one of our most lithiated devices.

Chapter 5: Conductivity corrections from quantum interferences Quantum interference corrections to the conductivity in graphene single layers and bilayers are introduced. They provide access to characteristic time scales governing the charge carrier transport, one of which we find to be sensitive to the presence of intercalated Li-ions. From low-temperature magnetotransport measurements, we thus provide corroborating evidence for the reversible intercalation of Li-ions in our bilayer graphene devices.

**Chapter 6: Intercalate diffusion pathways** Even though it is plausible that lithium intercalates in between the two carbon sheets of bilayer graphene, it is challenging to distinguish whether Li-ions are located underneath, above or in between the two graphene layers. Combining a series of ex situ characterization methods with specific device designs, we unambiguously identify a single efficient lithium diffusion pathway in our devices: in between graphene sheets, only.

Chapter 7: Intercalate diffusion kinetics Using time-resolved in situ electronic transport measurements we gain unprecedented direct access to the intercalate diffusion kinetics in our bilayer graphene devices. After an introduction to intercalate diffusion as described by Fick's laws, we describe an appropriate numerical solution allowing us to extract the chemical diffusion coefficient  $D^{\delta}$  of Li in bilayer graphene. We demonstrate ultrafast lithium diffusion exceeding diffusion in bulk graphite by an order of magnitude and even surpassing diffusion of sodium chloride in liquid water.

6 1 Introduction

Parts of the results presented in this dissertation are published elsewhere: M. Kühne, F. Paolucci, J. Popovic, P. M. Ostrovsky, J. Maier, and J. H. Smet. Ultrafast lithium diffusion in bilayer graphene. *Nature Nanotechnology* **12**, 895–900 (2017)

#### References

- 1. Weiss, A.: Ein Geheimnis des chinesischen Porzellans. Angew. Chemie 75, 755–762 (1963)
- Wittingham, M.S., Jacobson, A.J. (eds.): Intercalation Chemistry. Materials Science and Technology. Academic Press, New York (1982)
- 3. Lévy, F. (ed.): Intercalated layered materials. Physics and Chemistry of Materials with Layered Structures, vol. 6. D. Reidel Publishing Company, Dordrecht (1979)
- 4. Dresselhaus, M.S. (eds.): Intercalation in Layered Materials. NATO ASI Series. Series B: Physics, vol. 148. Springer Science+Business Media, New York (1986)
- Legrand, A.P., Flandrois, S., (eds.): Chemical Physics of Intercalation. NATO ASI Series. Series B: Physics, vol. 172. Springer Science+Business Media, New York (1987)
- Bernier, P., Fischer, J.E., Roth, S., Solin, S.A. (eds.): Chemical Physics of Intercalation II. NATO ASI Series. Series B: Physics, vol. 305. Springer Science+Business Media, New York (1993)
- Schafhaeutl, C.: Ueber die Verbindungen des Kohlenstoffes mit Silicium, Eisen und anderen Metallen, welche die verschiedenen Gallungen von Roheisen, Stahl und Schmiedeeisen bilden. J. Prakt. Chem. 21, 129–157 (1840)
- Novoselov, K.S., et al.: Two-dimensional gas of massless Dirac fermions in graphene. Nature 438, 197–200 (2005)
- 9. Zhang, Y., Tan, Y.-W., Stormer, H.L., Kim, P.: Experimental observation of the quantum Hall effect and Berry's phase in graphene. Nature **438**, 201–204 (2005)
- 10. Weller, T.E., Ellerby, M., Saxena, S.S., Smith, R.P., Skipper, N.T.: Superconductivity in the intercalated graphite compounds C<sub>6</sub>Yb and C<sub>6</sub>Ca. Nat. Phys. 1, 39–41 (2005)
- Heguri, S., et al.: Superconductivity in the graphite intercalation compound BaC<sub>6</sub>. Phys. Rev. Lett. 114, 247201 (2015)
- Smith, R.P., et al.: Superconductivity in graphite intercalation compounds. Physica C 514, 50–58 (2015)
- Dresselhaus, M.S., Dresselhaus, G.: Intercalation compounds of graphite. Adv. Phys. 30, 139– 326 (1981)
- Zabel, H., Solin, S.A. (eds.): Graphite Intercalation Compounds I. Springer Series in Materials Science, vol. 14. Springer, Heidelberg (1990)
- 15. Zabel, H., Solin, S.A. (eds.): Graphite Intercalation Compounds II. Springer Series in Materials Science, vol. 18. Springer, Heidelberg (1992)
- Enoki, T., Endo, M., Suzuki, M.: Graphite Intercalation Compounds and Applications. Oxford University Press, Oxford (2003)
- Hérold, A.: Recherches sur les composés d'insertion du graphite. Bull. Soc. Chim. France 187, 999–1012 (1955)
- Besenhard, J.O.: The electrochemical preparation and properties of ionic alkali metal-and NR<sub>4</sub>-graphite intercalation compounds in organic electrolytes. Carbon 14, 111–115 (1976)
- Daniel, C., Besenhard, J.O. (eds.): Handbook of Battery Materials. Wiley-VCH, Weinheim (2011)
- Julien, C., Mauger, A., Vijh, A., Zaghib, K.: Lithium Batteries. Springer International Publishing, Cham (2016)
- 21. Aoki, H., Dresselhaus, M.S. (eds.): Physics of Graphene. NanoScience and Technology. Springer International Publishing, Cham (2014)
- Novoselov, K.S., et al.: Electric field effect in atomically thin carbon films. Science 306, 666–669 (2004)

References 7

23. Novoselov, K.S., Mishchenko, A., Carvalho, A., Castro Neto, A.H.: 2D materials and van der Waals heterostructures. Science **353**, aac9439 (2016)

- 24. Bisri, S.Z., Shimizu, S., Nakano, M., Iwasa, Y.: Endeavor of iontronics: from fundamentals to applications of ion-controlled electronics. Adv. Mater. **29**, 1607054 (2017)
- 25. Wan, J., et al.: Tuning two-dimensional nanomaterials by intercalation: materials, properties and applications. Chem. Soc. Rev. 45, 6742–6765 (2016)
- Gallagher, P., et al.: A high-mobility electronic system at an electrolyte-gated oxide surface. Nat. Commun. 6, 6437 (2015)
- 27. Ovchinnikov, D., et al.: Disorder engineering and conductivity dome in ReS<sub>2</sub> with electrolyte gating. Nat. Commun. **7**, 12391 (2016)
- 28. Browning, A., et al.: Evaluation of disorder introduced by electrolyte gating through transport measurements in graphene. Appl. Phys. Expr. **9**, 065102 (2016)
- Petach, T.A., et al.: Disorder from the bulk ionic liquid in electric double layer transistors. ACS Nano 11, 8395–8400 (2017)

# **Chapter 2 Electronic Properties**



The electronic properties of single layer graphene and bilayer graphene have been subject to many scientific works, reviews of which have been published, e.g., by Castro Neto et al. [1], McCann and Koshino [2] and Koshino and Ando [3]. A concise overview of aspects relevant to the understanding of the following chapters is given hereafter. The discussion proceeds from the crystal and electronic band structures of both single layer and bilayer graphene to the transport of charge carriers in such two-dimensional materials, also in the presence of an applied magnetic field.

# 2.1 Single Layer Graphene

Single layer graphene consists of carbon atoms arranged in a two-dimensional honeycomb structure, see Fig. 2.1a. The distance between neighboring atoms is only  $a_0 = 1.42 \,\text{Å}$ . This crystal structure is stabilized by strong sp<sup>2</sup>-bonds, the formation of which requires three out of four valence electrons per C atom. The remaining valence electron resides in the out-of-plane  $2p_z$ -orbitals, the overlap of which forms so-called  $\pi$ -electronic states close to the Fermi level  $\epsilon_F$ . As the Bravais lattice of single layer graphene is hexagonal (lattice vectors  $a_1$  and  $a_2$  in Fig. 2.1a with the lattice constant  $a = |a_1| = |a_2| = \sqrt{3} \cdot a_0 = 2.46 \,\text{Å}$ ) with a two-atomic basis, there are in fact two such  $2p_z$ -electrons per unit cell (grey area in Fig. 2.1a) resulting in two  $\pi$ -electronic bands. In intrinsic single layer graphene, one of these bands—the valence band—is completely filled while the other one—the conduction band—is completely empty with  $\epsilon_F$  lying between the two. There is however no gap between valence and conduction band, as reveals a plot of their dispersion shown for the 1st Brillouin zone (BZ) in Fig. 2.1c, d. For the sake of orientation, Fig. 2.1b shows the (again hexagonal) reciprocal lattice with the primitive lattice vectors  $b_1$  and  $b_2$  (where  $|b_1| = |b_2| = 4\pi/\sqrt{3}a$ ) as well as the 1st BZ (grey area) in which the high symmetry points  $\Gamma$ , M, K, and K' are labeled. A particularity of single layer graphene are

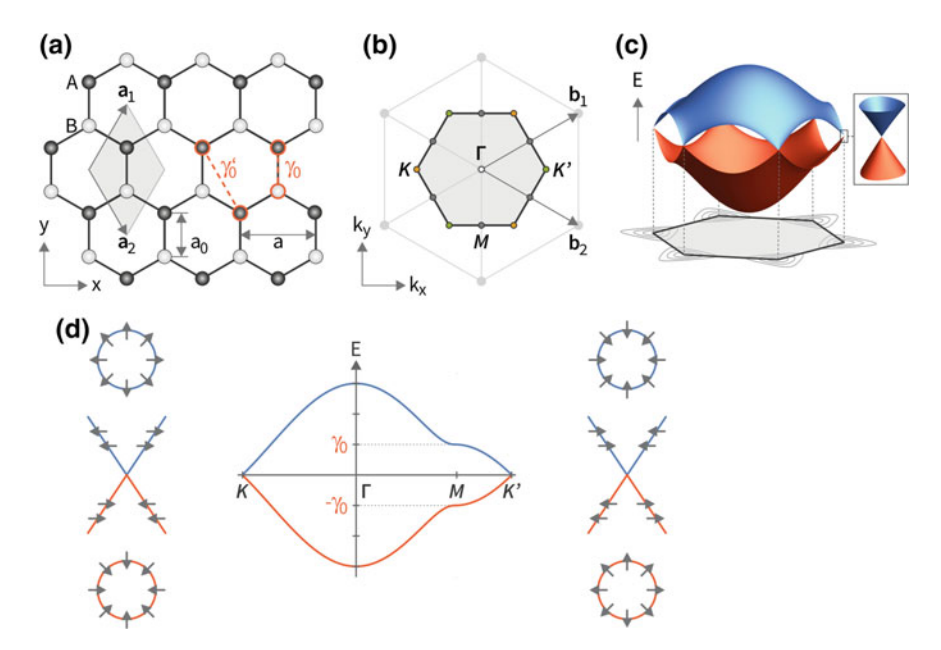


Fig. 2.1 Single layer graphene. a Crystal structure with the lattice vectors  $a_1$  and  $a_2$ , the lattice constant  $a = \sqrt{3} \cdot a_0 = 2.46$  Å, and the elementary unit cell (grey area). Red dashed lines indicate nearest and next-nearest neighbor coupling, parametrized by  $\gamma_0$  and  $\gamma_0'$ , respectively. **b** Reciprocal space with the lattice vectors  $b_1$  and  $b_2$ , the 1st Brillouin zone (BZ, grey area), and the high-symmetry points  $\Gamma$ , M, K, and K'. **c** Dispersion of the two  $\pi$ -electronic bands in the 1st BZ, calculated from Eq. A.2 using  $\gamma_0 = 3$  eV and  $\gamma_0' = 0.1$  eV. The inset shows the approximately linear dispersion in the vicinity of the K-point (Dirac cone). **d** Dispersion of electronic states along high-symmetry lines in the 1st BZ (here,  $\gamma_0'$  is neglected). Arrows indicate the pseudospin orientation for the valence and conduction band in the vicinity of the  $K^{(1)}$ -point

the band contact points at  $K^{(\prime)}$  with approximately linear dispersion in their vicinity: so-called Dirac points. Due to the simultaneous absence of electronic states at precisely  $\epsilon_F$  and of a band gap, single layer graphene has been labeled a zero-gap semiconductor.

In real devices, the typical range of charge carrier densities in single layer graphene hardly exceeds a few  $10^{13}$  cm<sup>-2</sup>, corresponding to  $|\epsilon_F| \le 1$  eV. Accordingly, the electronic states most relevant to further discussion lie near  $K^{(\prime)}$  where their wave function can effectively be described by a two-component spinor  $\psi = (\psi_A, \psi_B)$ , with  $\psi_A$  ( $\psi_B$ ) the amplitude on sublattice A (B). Using the valley index  $\xi = +1$  ( $\xi = -1$ ) for the K (K') valley, the spinor obeys

$$\xi v_F \sigma(-i\hbar \nabla) \psi = \epsilon \psi, \tag{2.1}$$

resulting in

$$\epsilon(\kappa) = \hbar v_F \kappa, \tag{2.2}$$

with the Fermi velocity  $v_F \approx c/300$ , the wave vector relative to the Dirac point  $\kappa = |\mathbf{k} - \mathbf{K}^{(\prime)}|$ , and the vector of Pauli matrices  $\mathbf{\sigma} = (\sigma_x, \sigma_y)^{\mathsf{T}}$ . Equation 2.1 resembles the Dirac equation, in analogy to the solution of which antiparticles are represented by holes and spin is represented by sublattice occupation, referred to as pseudospin. More than just a mathematical requirement, the pseudospin is connected to a real (lattice) angular momentum  $\hbar/2$  [4, 5]. Its orientation is furthermore locked to  $\kappa$ . This property is characterized by the pseudospin winding number  $\omega_C$ , a topological invariant defining the number of rotations of the pseudospin when moving  $\kappa$  on a closed path  $\mathcal C$  around  $\mathbf K^{(\prime)}$  [6, 7]. In single layer graphene,  $\omega_C = -\alpha \xi$  ( $\alpha \xi$  is the chirality) with the band index  $\alpha = +1$  ( $\alpha = -1$ ) for conduction (valence) band. The pseudospin orientation for the electronic states at different momenta near  $\mathbf K^{(\prime)}$  is shown in Fig. 2.1d.

The aforementioned aspects of the electronic structure have intriguing consequences for the behavior of charge carriers in single layer graphene, some of which have been reviewed in Ref. [8]. To just mention a few, one should certainly note the unusual half-integer quantum Hall effect in graphene, [9, 10] caused by the Berry phase  $\Phi_B = \pi$  which is related to the pseudospin winding number as  $\Phi_B = \pi \omega_C$  [11]. This Berry phase furthermore induces a phase shift of  $\pi$  to the Shubnikov-de Haas oscillations in single layer graphene [9, 10, 12]. Another striking consequence is the suppression of charge carrier backscattering [13–15].

### 2.2 Bilayer Graphene

Bilayer graphene consists of two graphene sheets stacked upon each other. Unless stated otherwise, bilayer graphene denotes the Bernal-stacked crystal structure [16] depicted in Fig. 2.2a, obtained through a relative rotation of the two carbon layers by 60°. As a consequence, one sublattice of the upper layer (A2) is exactly on top of one sublattice of the lower layer (B1). The other two sublattices B2 (upper layer) and A1 (lower layer) do not sit on top of each other. Each atom B2 (A1) is rather located above (below) the center of the triangle formed by the three nearest atoms A1 (B2). The unit cell of bilayer graphene consequently contains four atoms, with the sites A2, B1 and A1, B2 referred to as dimer and non-dimer sites, respectively. Although the coupling between both layers is finite (van der Waals interaction), its overall magnitude is much weaker than the in-plane bonding. This is directly reflected in the much wider interlayer spacing  $c \approx 3.35$  Å, as compared to the in-plane nearest neighbor distance  $a_0 = a/\sqrt{3} \approx 1.42 \,\text{Å}$ . Nonetheless, this way of stacking is the energetically most favorable, hence also most abundant in natural graphite from which samples in this work are obtained. For the sake of completeness, the reciprocal lattice of bilayer graphene is shown in Fig. 2.2b, which is identical to the one of single layer graphene.

<sup>&</sup>lt;sup>1</sup>The general case of an arbitrary relative rotation angle is commonly referred to as twisted bilayer graphene. The special case of 0° relative rotation (where each C atom in the upper layer is located above a C atom in the lower layer) is referred to as AA stacking.

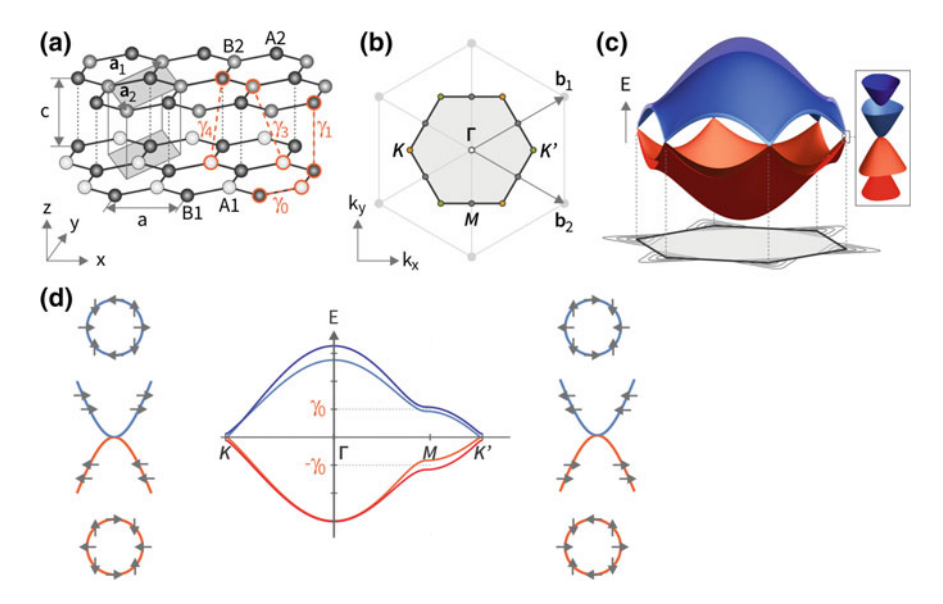


Fig. 2.2 Bilayer graphene. a Crystal structure with the lattice vectors  $a_1$  and  $a_2$ , the lattice constant a=2.46 Å, the interlayer distance c=3.35 Å, and the elementary unit cell (right prism with grey diamond-shaped base faces). Red dashed lines indicate coupling between different atomic sites, parameterized by  $\gamma_0$ ,  $\gamma_1$ ,  $\gamma_3$ , and  $\gamma_4$ . b Reciprocal space with the 1st Brillouin zone (BZ, grey area) and the high-symmetry points  $\Gamma$ , M, K, and K' (similar to single layer graphene). c Dispersion of the four  $\pi$ -electronic bands in the 1st BZ, calculated from Eq. A.4 using the values mentioned in the main text. The inset shows the dispersion in the vicinity of the K-point. d Dispersion of electronic states along high-symmetry lines in the 1st BZ. Arrows indicate the pseudospin orientation for valence and conduction band in the vicinity of the  $K^{(\prime)}$ -point

In the single-particle picture, the structure of bilayer graphene's  $\pi$ -electronic states can be calculated following a tight-binding approach, see Appendix A. Due to interactions between its two carbon layers, the description is more advanced than in the case of single layer graphene and can be deduced from a model established for bulk graphite by Slonczewski, Weiss and McClure [17, 18]. The parameters relevant for bilayer graphene are one intralayer nearest-neighbor hopping parameter  $\gamma_0$ , three interlayer hopping parameters  $\gamma_1$ ,  $\gamma_3$ ,  $\gamma_4$  (see Fig. 2.2a) and the energy difference between dimer and non-dimer sites  $\Delta'$  [2]. Values for these parameters reported from different experiments are stated in Table 2.1. The spread in the experimental values is due to different techniques having different sensitivity to individual parameters, and whether interaction-induced corrections to the values are taken into account or not. The dispersion of the  $\pi$ -electronic states in the 1st Brillouin zone shown in Fig. 2.2c, d is calculated for the parameter set reported by Kuzmenko et al. [19], i.e.,  $\gamma_0 = 3.16 \,\text{eV}$ ,  $\gamma_1 = 0.381 \,\text{eV}$ ,  $\gamma_3 = 0.38 \,\text{eV}$ ,  $\gamma_4 = 0.14 \,\text{eV}$ , and  $\Delta' = 0.022 \,\text{eV}$ . One may in principle further introduce the parameter U quantifying the energy difference between the two carbon layers, a finite value of which opens a gap in the energy spectrum [20].

Reference	[20] <sup>a</sup>	[21] <sup>b</sup>	[22] <sup>c</sup>	[23] <sup>c</sup>	[19] <sup>c</sup>	[24] <sup>d</sup>	[25] <sup>e</sup>
γ0	_	2.9	3	_	3.16(3)	3.43(1)	3.1
γ1	_	0.3	0.40(1)	0.404(10)	0.381(3)	_	_
γ3	0.12	0.1	0.3	_	0.38(6)	_	_
γ4	_	0.12	0.15(4)	_	0.14(3)	$0.063(1)\gamma_0$	0.22
$\Delta'$	_	_	0.0183	_	0.022(3)	-	_

**Table 2.1** Values of bilayer graphene band structure parameters in eV

Apart from there being four  $\pi$ -bands in bilayer graphene instead of two as in single layer graphene, the overall impression of the dispersion is one of striking similarity when comparing Figs. 2.2c to 2.1c. This stems from the weakness of the interlayer coupling merely resulting in a rather small overall correction in energy to the electronic states. Also the approximately linear dependence on momentum  $\kappa$ defined relative to the corners of the 1st Brillouin zone is retained, except in the very vicinity of  $K^{(\prime)}$ , where the dispersion is parabolic [26]. This becomes apparent in the inset to Fig. 2.2c. Here, the two low-energy bands stem from non-dimer atomic sites A1 and B2, while the two bands from the dimer sites A2 and B1 are split-off roughly by the value of  $\gamma_1$ . The main qualitative effect of  $\gamma_3$  is trigonal warping of the  $\pi$ bands, illustrated by the projection of conduction band isoenergy lines close to  $K^{(\prime)}$ onto the  $k_x - k_y$  plane in Fig. 2.2c with the 1st Brillouin zone shown by the grey area.  $\gamma_4$  mainly introduces an electron-hole asymmetry, most apparent in Fig. 2.2d, where the dispersion along high-symmetry lines in the 1st Brillouin zone is drawn. In line with the argument made for the case of single layer graphene above, the part of the electronic spectrum usually accessible in transport experiments including the ones of this work lies in the vicinity of  $K^{(\prime)}$ . One may describe charge carriers in this part of the spectrum by four-component spinor wave functions obeying a reduced, effective Hamiltonian with eigenvalues isotropic in  $\kappa = |\mathbf{k} - \mathbf{K}^{(\prime)}|$  neglecting contributions from  $\gamma_3, \gamma_4, \Delta'$  [2, 27]:

$$\epsilon_{\alpha}^{\pm}(\kappa) = \alpha \left[ \sqrt{3 \left( \frac{a \gamma_0 \kappa}{2} \right)^2 + \left( \frac{\gamma_1}{2} \right)^2} \pm \frac{\gamma_1}{2} \right].$$
 (2.3)

Here, we use the band index  $\alpha = +1$  ( $\alpha = -1$ ) for the conduction (valence) bands and + (-) for the split-off dimer (low energy non-dimer) bands, respectively. Frequent use of Eq. 2.3 is made throughout this work.

In addition to differences regarding the dispersion of electronic states in bilayer graphene as compared to single layer graphene, also the chiral properties are different. In bilayer graphene, the pseudospin winding number is  $\omega_C = -2\alpha\xi$ , with the valley

<sup>&</sup>lt;sup>a</sup>Angle-resolved photoemission spectroscopy

<sup>&</sup>lt;sup>b</sup>Raman spectroscopy

<sup>&</sup>lt;sup>c</sup>Infrared spectroscopy

<sup>&</sup>lt;sup>d</sup>Analysis of the effective mass extracted from Shubnikov-de Haas measurements

<sup>&</sup>lt;sup>e</sup>Scanning tunneling spectroscopy

index  $\xi = +1$  ( $\xi = -1$ ) for states at K(K'). The pseudospin orientation for the electronic states at different momenta in bilayer graphene near  $K^{(\prime)}$  is shown in Fig. 2.2d. It can be seen, that the pseudospin rotates twice as fast on a closed path  $\mathcal{C}$  around  $K^{(\prime)}$  than in the case of single layer graphene, compare with Fig. 2.1d. Consequently, the charge carriers have the (trivial) Berry phase  $\Phi_B = 2\pi$ , [26, 27] equivalent to  $\Phi_B = 0$  [7].

Charge carriers in bilayer graphene have properties profoundly different from the ones in single layer graphene. For example, the pseudospin winding number of  $\pm 2$  leads to the conventional integer quantum Hall effect with a series of plateaus in  $\sigma_{xy}$  at values of  $4e^2/h$  except for a characteristic step across the charge neutrality point of  $8e^2/h$ , [7, 26] see Fig. 2.13. And in contrast to suppressed backscattering in single layer graphene, charge carriers in bilayer graphene have anti-Klein properties, i.e., they have zero transmission at normal incidence on a potential barrier [14, 28].

### 2.3 Fermi-Level Dependence of Electronic Properties

In practical devices made of single layer graphene or bilayer graphene as they are used in this work, the Fermi level  $\epsilon_F$  usually resides at electronic states in the vicinity of  $K^{(\prime)}$ . As will be discussed in Sect. 2.5,  $\epsilon_F$  is easily controlled and may be tuned to sit in the valence band, the conduction band, in between the two (i.e., at the charge neutrality point, CNP), or even in the split-off bands in the case of bilayer graphene. Within  $\pm 1\,\mathrm{eV}$  around the CNP, the dependence on  $\epsilon_F$  for a few important properties is shown in Fig. 2.3 for both single layer graphene (left column) and bilayer graphene (right column), starting with the approximate dispersion of electronic states near  $K^{(\prime)}$  (top) calculated from Eqs. 2.2 and 2.3, respectively.

The first row of Fig. 2.3 shows the approximate density of states (DOS), which reaches zero exactly at charge neutrality in the case of single layer graphene. In bilayer graphene, the total DOS (black line) shows sudden jumps known as van Hove singularities at  $\epsilon = \pm \gamma_1 \approx 0.39\,\mathrm{eV}$  where the split-off bands set in. Contributions to the total DOS from individual bands are plotted in the respective colors used in the schematic dispersion around  $K^{(\prime)}$  in the top of Fig. 2.3. As  $\epsilon_F$  is moved away from the CNP at  $\epsilon = 0\,\mathrm{V}$ , more and more electronic states get populated (depleted) in the conduction (valence) band, thereby increasing the density of free charge carriers

$$n(\epsilon_F) = \int_0^{\epsilon_F} DOS(\epsilon) d\epsilon.$$
 (2.4)

If  $\epsilon_F > 0$  ( $\epsilon_F < 0$ ) the carriers are electrons (holes), respectively, the properties of which are symmetric with respect to the CNP-at least within the approximation of Eqs. 2.2 and 2.3.  $n(\epsilon_F)$  is plotted in the second row of Fig. 2.3, from where it should be noted that  $n(\epsilon_F = 0) = 0$  for both single layer and bilayer graphene. Furthermore,  $n(\epsilon_F)$  of bilayer graphene shows a much steeper increase as soon as  $|\epsilon_F| > \gamma_1$ , due to the higher DOS available thanks to the second subband.

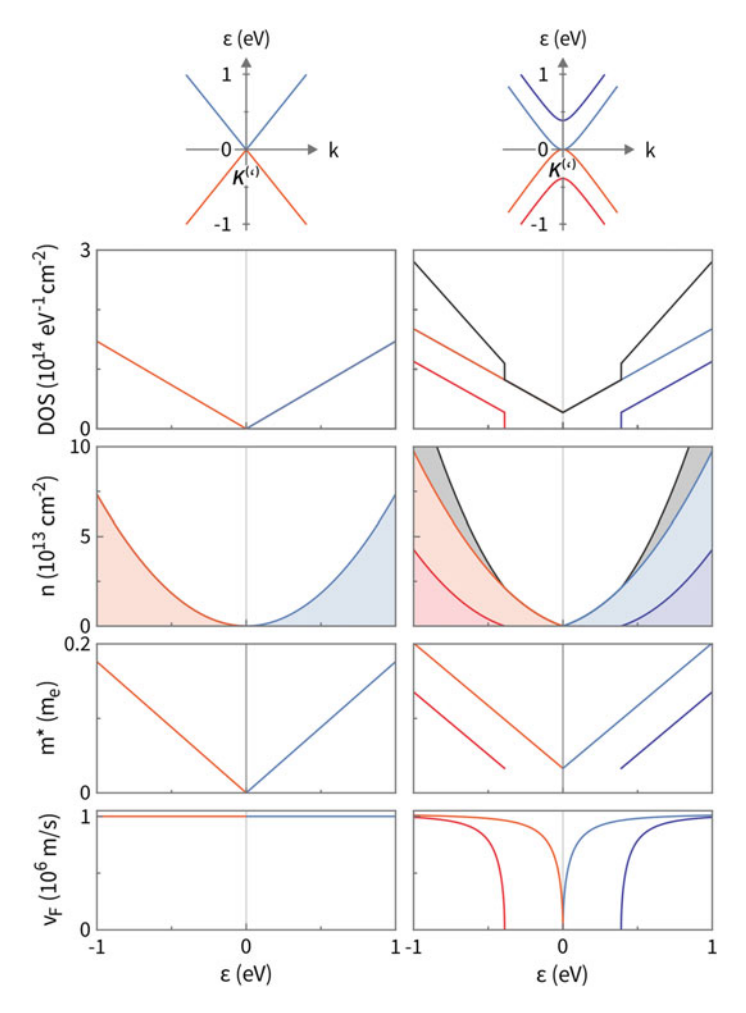


**Fig. 2.3** Energy dependence of the density of states (DOS), charge carrier density n, effective mass  $m^*$ , and Fermi velocity  $v_F$  (from top to bottom) near  $K^{(\prime)}$  for single layer graphene (left) and bilayer graphene (right). The approximate low-energy dispersion of electronic states near  $K^{(\prime)}$  is plotted above from Eqs. 2.2 and 2.3, respectively. Properties of individual bands are drawn in the respective color, while their sum is drawn in black

Next we consider the charge carrier effective mass  $m^*$ , which within the approximation of an isotropic band  $E(\kappa)$  can be defined as [24, 29], <sup>2</sup>

$$m^* = \hbar^2 \kappa \left(\frac{\partial \epsilon}{\partial \kappa}\right)^{-1}.$$
 (2.5)

 $<sup>^{2}</sup>m^{*} = \hbar^{2} \left(\frac{\partial^{2} \epsilon}{\partial k^{2}}\right)^{-1}$  only holds for parabolic bands.

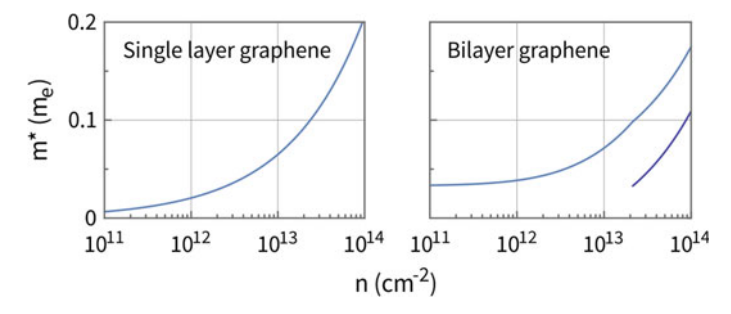


Fig. 2.4 Effective mass  $m^*$  as a function of charge carrier density n for the conduction band(s) of single layer graphene (left) and bilayer graphene (right)

In both single layer graphene and bilayer graphene,  $m^*$  depends on the momentum  $\kappa = |\mathbf{k} - \mathbf{K}^{(\prime)}|$  and increases for each band as  $|\epsilon_F|$  increases, due to the non-parabolic band-dispersion [9, 10, 24, 30].  $m^*$  is plotted in the third row of Fig. 2.3. The main difference lies in the effective mass being zero at the CNP in single layer graphene, while  $m^*(\epsilon = 0 \, \mathrm{eV}) \approx 0.033 \cdot m_e$  stays finite in bilayer graphene. Here,  $m_e$  is the electron rest mass. In Fig. 2.4,  $m^*$  is plotted as a function of the charge carrier concentration n for both materials. In the case of bilayer graphene (right panel), it can be seen that a constant effective mass of  $m^* \approx 0.033 \cdot m_e$  yields a good description for  $n \lesssim 10^{12} \, \mathrm{cm}^{-2}$ .

We further introduce the Fermi velocity  $v_F$ , which is related to the Fermi momentum  $p_F = \hbar \kappa_F$  via the effective mass  $m^*$  as  $\hbar k_F = v_F m^*$ . Using Eq. 2.5,

$$v_F = \frac{\hbar \kappa_F}{m^*} = \frac{1}{\hbar} \left. \frac{\partial \epsilon}{\partial \kappa} \right|_{\kappa = \kappa_F},\tag{2.6}$$

which we plot in the last row of Fig. 2.3. It can be seen, that within the approximation of Eq. 2.2,  $v_F \approx 1 \cdot 10^6$  m/s is constant for single layer graphene. In bilayer graphene,  $v_F$  varies strongly with  $\epsilon$ , approaching the single layer graphene value at higher  $|\epsilon|$  and going to zero at each band onset, at least within the approximation of Eq. 2.3. Note that beyond the single-particle picture,  $v_F$  has been demonstrated to be dependent on the charge carrier concentration n due to electron-electron interactions [31]. Conditions to reveal such interaction effects are however not met in most experimental works on graphene including this, unless utmost care is taken to reduce the charge inhomogeneity commonly found in practical devices (see Sect. 2.5). This can in principle be achieved, for instance in suspended graphene flakes of extreme quality [32, 33].

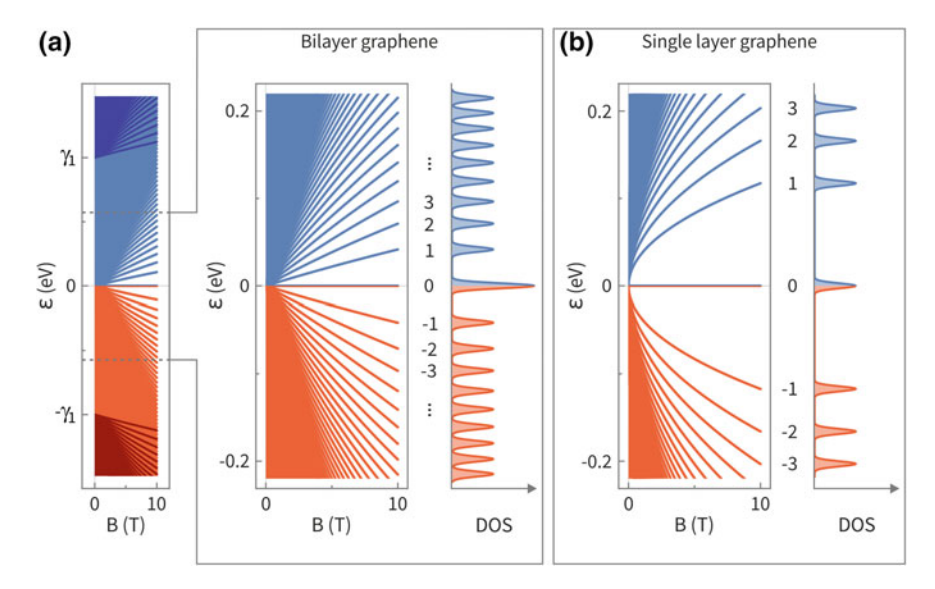


Fig. 2.5 Landau levels (LLs) in **a** bilayer graphene and **b** single layer graphene calculated from Eqs. 2.8 and 2.7, respectively, using  $\gamma_0 = 3.16 \, \text{eV}$  and  $\gamma_1 = 0.39 \, \text{eV}$ 

## 2.4 Electronic Properties at Finite Magnetic Field

Moving charge carriers subject to a magnetic field of strength B = |B| experience the Lorentz force  $F = q(v \times B)$ , forcing them to move on so-called cyclotron orbits perpendicular to B. Here, v and q are velocity and charge of the charge carriers, respectively. As a result of quantum mechanics, these cyclotron orbits are quantized and associated to a discrete set of highly degenerate energy levels, so-called Landau levels (LLs). The degeneracy  $\delta$  of each LL increases with increasing B and is given by the ratio of the magnetic flux  $\Phi = A \cdot B$  threading the area A and the flux quantum  $\Phi_0 = h/e$ , i.e.,  $\delta = \Phi/\Phi_0$ . LLs may be further degenerate, e.g., if the Zeeman energy remains negligible.

We proceed restricting ourselves to the situation where charge carriers are confined to two dimensions (x and y) and are subject to a perpendicular magnetic field  $\mathbf{B} = (B_x, B_y, B_z)^T = (0, 0, B)^T$ , as this configuration is used throughout this work. For illustration purposes we begin with the case of such charge carriers hosted in single layer graphene, the LL energies of which can be approximately described as [1]

$$\epsilon_n = \operatorname{sgn}(n) v_F \sqrt{2e\hbar B|n|},$$
(2.7)

with the LL index  $n = 0, \pm 1, \pm 2...$  Equation 2.7 describes LLs for electrons (n > 0), holes (n < 0), as well as a zeroth LL shared by both types of charge carriers, see Fig. 2.5b. The  $\sqrt{B}$ -dependence of the levels, their non-equidistance at a given value of B as well as the B-independent level at  $\epsilon = 0$  are characteristic properties

of the Dirac electronic system in single layer graphene. Note that all LLs are fourfold degenerate due to the two spin and two valley degrees of freedom, i.e., the degeneracy is  $\delta(B) = 4eB/h$ .

In bilayer graphene, the approximate parabolicity of the  $\pi$ -electronic bands in the vicinity of  $K^{(\prime)}$  at B=0 gives rise to a very different LL spectrum, see Fig. 2.5a. The LL energies can be stated as [27, 34]

$$\epsilon_n = \operatorname{sgn}(n) \sqrt{\frac{\gamma_1^2}{2} + \left(|n| + \frac{1}{2}\right) E_1^2 \pm \sqrt{\frac{\gamma_1^4}{4} + \left(|n| + \frac{1}{2}\right) \gamma_1^2 E_1^2 + \frac{E_1^4}{4}}}, \quad (2.8)$$

where  $n=0,\pm 1,\pm 2$  and  $E_1^2=3a^2\gamma_0^2eB/2\hbar$ . Equation 2.8 also yields LLs for electrons (n>0), holes (n<0), as well as a zeroth LL shared by both types of charge carriers. Additional LLs from the split-off bands (+ instead of – in Eq. 2.8) set in at energies  $|\epsilon|\geq \gamma_1$  (dark blue and dark red lines in Fig. 2.5a). In contrast to the case of single layer graphene, LLs in bilayer graphene show an almost linear dependence on B, making them appear almost equidistant in energy at a given value of B. Furthermore, the B-independent LL at  $\epsilon=0$  has an eightfold degeneracy, while all others are fourfold degenerate as in single layer graphene. This difference between both systems is apparent in Fig. 2.5, where the density of states (DOS) at  $B=10\,\mathrm{T}$  shows a series of broadened LLs of equal magnitude, except for the zeroth LL in bilayer graphene whose degeneracy is doubled.

The LL spectra of both single layer graphene and bilayer graphene as well as consequences thereof have been confirmed by many experimental works. Among the most direct spectroscopic methods apt to reveal and distinguish the introduced LL structures are scanning tunneling spectroscopy [35–37] and Raman spectroscopy [38]. The magnetotransport of charge carriers shows characteristics very much determined by the respective LL spectrum, as will be discussed in the following after an introduction to the zero-field transport.

# 2.5 Electronic Transport in the Absence of a Magnetic Field

The transport of charge carriers confined to two dimensions can be captured within the framework of the classical Drude model, according to which an applied electric field E drives an electrical current of density

$$i = \sigma E \tag{2.9}$$

along the sample. Equation 2.9 defines the electrical conductivity  $\sigma$ , which relates to the density n and mobility  $\mu$  of charge carriers according to

$$\sigma = ne\mu, \tag{2.10}$$

in the case of a single type of charge carriers dominating the overall transport behavior. Here,  $\mu$  is a measure of the charge carriers' drift velocity  $\mathbf{v}_D$  induced per electric field strength E and can be defined as

$$\mu = \frac{|\boldsymbol{v}_D|}{E} = \frac{e\tau_{\text{tr}}}{m^*},\tag{2.11}$$

where  $\tau_{\rm tr}$  is the transport time (average time between scattering events) and  $m^*$  is the effective mass of the charge carriers. Both  $\sigma$  and n can be experimentally determined using a suitable measurement setup, allowing to extract parameters such as  $\mu$  and  $\tau_{\rm tr}$ .

To measure the conductivity  $\sigma$ , we impose a constant current I on a twodimensional device of width W and monitor the longitudinal voltage drop  $U_{xx}$  (i.e., along the current flow direction) between two voltage probes separated by a length L. In a linear four-point geometry as for the bilayer graphene device shown in Fig. 2.6a, the leads used to impose the current are different from the ones used to sense the voltage drop. From the measured resistance  $R = U_{xx}/I$  we can extract the conductivity  $\sigma$  (which is the inverse of the resistivity  $\rho$ ) if W and L are known:

$$\sigma = 1/\rho = \frac{L}{W}R^{-1}.\tag{2.12}$$

To tune the charge carrier density, we take advantage of designing our 2D structure on top of an electrically conducting substrate separated by an insulating layer of thickness d and dielectric constant  $\epsilon_r$ , see Fig. 2.6a. Assuming a simple parallel plate capacitor model with areal capacitance  $C/A = \epsilon_0 \epsilon_r/d$ , one can relate the electric field induced charge carrier density  $\Delta n$  to the applied backgate voltage  $U_G$  as

$$\Delta n = \frac{Q}{e \cdot A} = \frac{U_G \cdot C}{e \cdot A} = \epsilon_0 \cdot \epsilon_r \cdot \frac{U_G}{e \cdot d}, \tag{2.13}$$

where Q/A is the induced charge per unit area on the 2D structure and  $\epsilon_0$  the vacuum permittivity. In our case, the insulating material is thermally grown SiO<sub>2</sub> with  $d \approx 300\,\mathrm{nm}$  and  $\epsilon_r \approx 3.9$ , hence  $C/A \approx 11.5\,\mathrm{nF}\cdot\mathrm{cm}^{-2}$  and  $\Delta n/U_G \approx 7.2\cdot10^{10}\,\mathrm{cm}^{-2}\mathrm{V}^{-1}$ . The charge carrier density can be determined more precisely from magnetotransport measurements, as will be introduced in the following Sect. 2.6. The simple parallel plate capacitor model however finds wide application in the field and has repeatedly been demonstrated to quantitatively agree well with experiments [9, 10, 26]. A limit to this technique is set by the breakdown field of the gate dielectric, which is on the order of a few MV/cm in the relevant case of thermal SiO<sub>2</sub>, [39] i.e., on the order of several tens of V for our  $d=300\,\mathrm{nm}$  thick SiO<sub>2</sub>. Consequently, the range within which n can be varied using this field-effect method with a solid gate dielectric

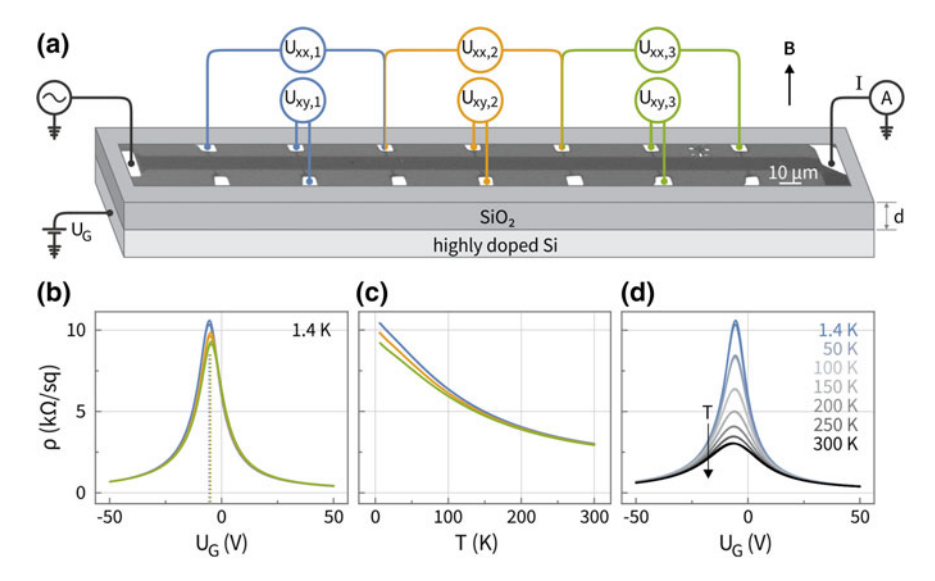


Fig. 2.6 a Optical micrograph of a bilayer graphene device combined with the schematic experimental setup used for measuring both longitudinal and transverse voltage drops  $U_{xx,i}$  and  $U_{xy,i}$  in different sections  $i=\{1,2,3\}$  of the device. **b-d** Resistivity  $\rho$  measured at B=0 T as a function of backgate voltage  $U_G$  and/or temperature T. The line colors in  $(\mathbf{b},\mathbf{c})$  correspond to the three sections of the device. The traces in  $(\mathbf{c})$  were measured at  $U_G\approx -5$  V. In  $\mathbf{d}$  we show data from section i=1 of the device

is on the order of a few  $10^{12} \text{cm}^{-2}$ . It usually proves safe in our experiment to keep  $|U_G| \le 50 \,\text{V}$  in order to prevent dielectric breakdown, i.e.,  $|\Delta n| \le 3.6 \cdot 10^{12} \text{cm}^{-2}$ .

The resistivity  $\rho$  of the bilayer graphene device shown in Fig. 2.6a measured at different temperatures T and at different backgate voltages  $U_G$  is plotted in Fig. 2.6b–d. Here,  $\rho$  was extracted simultaneously at three different sections of the device, each of width  $W=8\mu\mathrm{m}$  and length  $L=80\mu\mathrm{m}$ , labeled  $i=\{1,2,3\}$  in the figure (blue, orange, green lines respectively). The almost perfect overlap of the data shown in Fig. 2.6b, c demonstrates the overall device homogeneity and degree of reproducibility of the measurement. At all temperatures T, the dependence of  $\rho$  on  $U_G$  shows a strong peak at some value  $U_{\mathrm{CNP},i}$  with respect to which  $\rho(U_G)$  appears symmetric. This observation is general and applies to both single layer and bilayer graphene devices, including all that are subject to this work.  $\rho(U_G)$  reflects the particular band structure near  $K^{(\ell)}$  with a peak in  $\rho$  at the charge neutrality point (CNP), where a minimum number of charge carriers is present to participate in transport. As  $\epsilon_F$  is tuned away from the CNP by increasing  $|U_G - U_{\mathrm{CNP},i}|$ ,  $\rho$  drops as more and more states get populated. At  $U_G < U_{\mathrm{CNP},i}$  the bilayer becomes increasingly hole-doped, while at  $U_G > U_{\mathrm{CNP},i}$  it becomes increasingly electron-doped. The symmetry of the measured

<sup>&</sup>lt;sup>3</sup> Although higher values of  $|\Delta n|$  have successfully been achieved by this method, dielectric break-down remains a fundamental limit to field effect gating, making it difficult to reach values beyond  $|\Delta n| = 10^{13} \, \text{cm}^{-2}$ .

 $\rho(U_G)$  with respect to  $U_{\rm CNP,i}$  reflects the high degree of symmetry between electron and hole states in the sample, as expected from the band structure considerations in Sect. 2.2. The shift of the CNP with respect to  $U_G=0\,{\rm V}$  can be attributed to doping from impurities, [40] i.e., residuals from processing steps during device fabrication as well as adsorbed species from the environment. Careful device processing can lead to  $U_{\rm CNP,i}\approx 0$ . The data shown in Fig. 2.6b, d is a satisfying example of careful sample preparation, with  $U_{\rm CNP,1}\approx -5.65\,{\rm V}$ ,  $U_{\rm CNP,2}\approx -5.15\,{\rm V}$ , and  $U_{\rm CNP,3}\approx -4.75\,{\rm V}$  showing little spread across the device. Furthermore, the two curves obtained from ramping  $U_G$  up and down (both plotted for each contact pair i in Fig. 2.6b as well as for each T in Fig. 2.6d) nearly perfectly overlap, i.e., there is only a minimal amount of dipolar adsorbates typically known to induce significant hysteresis in this type of measurement [41, 42].

Introducing  $n_{\text{imp,i}} = -\epsilon_0 \epsilon_r U_{\text{CNP,i}}/(ed)$  as the charge carrier density locally induced from residual doping in section  $i = \{1, 2, 3\}$  of the bilayer graphene device shown in Fig. 2.6a, we can convert the applied backgate voltage  $U_G$  into an absolute charge carrier density  $n = n_{\text{imp,i}} + \Delta n(U_G)$ . In Fig. 2.7a, the same data of  $\rho$  from Fig. 2.6b is plotted now as a function of n. Within the given range of n, three transport regimes can be identified, separated in Fig. 2.7a by black dotted lines at  $\pm n_{eh}$ : at  $n < -n_{eh}$  ( $n > n_{eh}$ )  $\epsilon_F$  is in the valence (conduction) band, i.e., bilayer graphene is hole (electron) doped. For  $|n| \le n_{eh}$ , i.e., close to charge neutrality, it was shown that charged impurities in the substrate imprint a spatially varying potential landscape onto the device, so-called electron-hole puddles [43]. The false color plot in the inset of Fig. 2.7a is an illustration of the possible spatial distribution of electron-hole puddles in our sample, with amplitudes in the doping level on the order of  $\pm 3 \cdot 10^{11}$  cm<sup>-2</sup>. An additional potential profile extracted along the dotted black line is shown in the inset. Spatial density fluctuations on this order of magnitude are commonly observed in single layer graphene [43–47] and bilayer graphene [48] samples on thermal SiO<sub>2</sub>.

According to the procedure of Couto et al. [46], we extract  $n_{eh}$  from a log-log plot of  $\sigma(n)$ , see Fig. 2.7b. Here,  $n_{eh}$  can be determined from the crossing between the constant value of minimum conductivity  $\log(\sigma_{\min})$  (black lines) and the linearly extrapolated value of  $\log \sigma$  at high n (blue (red) line for electron (hole) doped regime). The graphs in Fig. 2.7b illustrate this procedure for all three sections of the device shown in Fig. 2.6a, with  $n_{eh} \approx 3.3 \pm 0.3 \cdot 10^{11}$  cm<sup>-2</sup> showing negligible spread of values obtained from the different sections as well as from the electron and hole doped sides, respectively. At the time of this writing there is no means to reduce the amplitude of the electron-hole puddles in bilayer graphene devices on SiO<sub>2</sub>, which consequently are consistently observed in all our devices. As the charge carrier transport in this regime involves two participating species (electrons and holes), a two-carrier model may be used to approximate its description [49]. As we shall typically be interested in charge carrier density ranges much higher than  $n_{eh}$ , we will

<sup>&</sup>lt;sup>4</sup>The amplitude of electron-hole puddles may in fact be a lot reduced by encapsulating bilayer graphene in hexagonal boron nitride (hBN). Alternatively, electron-hole puddles can be avoided altogether when bilayer graphene is suspended. Choosing either option, at the time of this writing it is challenging to produce devices of big enough size as needed for the experiments conducted in this work. We have therefore refrained from pursuing them here.

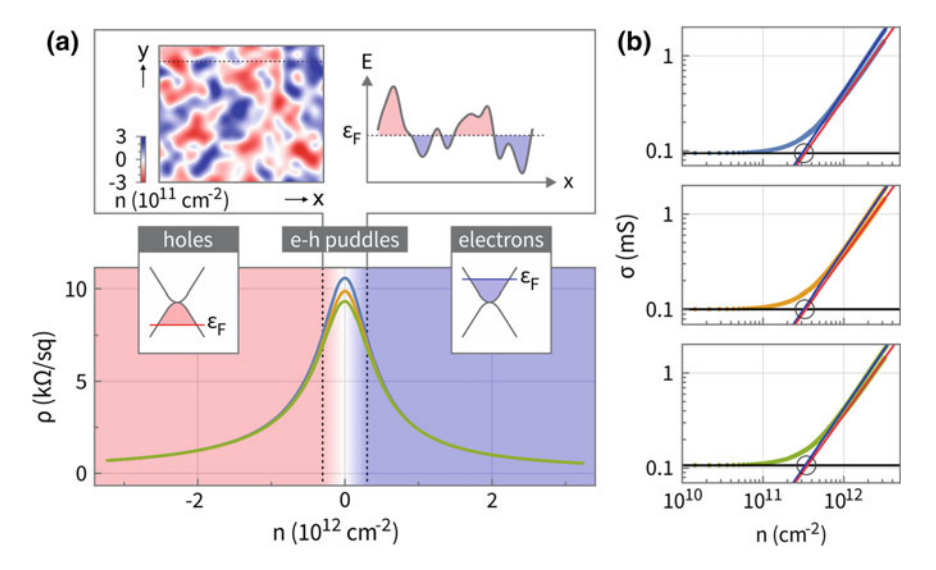


Fig. 2.7 Charge carrier transport in bilayer graphene as a function of charge carrier density n at  $T=1.4~\rm K|$ . a Resistivity  $\rho$  of the device shown in Fig. 2.6a. Inserts highlight three different transport regimes: hole-doped, electron-doped and electron-hole puddles. The latter is further illustrated by the typical spatial density fluctuations as well as an associated potential profile taken along the dashed line in the false color plot. b Conductivity  $\sigma$  (inverse of the data plotted in (a)) in log-log plot, used to determine the magnitude of the density fluctuations  $n_{eh}$  in the electron-hole puddle regime

however not have a closer look at this part of the transport regime. Note, that these electron-hole puddles may cause a significant insulating behavior in bilayer graphene around charge neutrality, due to activated carrier transport between electron and hole puddles [50, 51]. This is indeed what we observe in our device (see Fig. 2.6c, d) in agreement with reports from other experiments [24, 52]. Far away from the charge neutrality point, bilayer graphene may actually show metallic behavior [24].

In the case of a single type of charge carriers dominating the overall transport behavior, we can extract their mobility  $\mu = \sigma/(ne)$  from the presented measurements following the Drude approach, see Fig. 2.8a. While the result shows again little variation on the section of the bilayer graphene device, we find  $\mu$  to depend on n, with  $\mu$  increasing as |n| increases (at least for  $|n| \gg n_{eh}$  within the given density range). Additionally, there is a slight difference between the electron and hole doped regime. The first observation, common for bilayer graphene devices on SiO<sub>2</sub>, was shown to be due to the mobility limited by Coulomb scattering scaling as  $\mu_C \propto n$  [52, 53]. The second observation likely reflects an asymmetry between repulsive and attractive scattering (i.e., a different scattering cross section for electrons and holes) as in single layer graphene [54]. The measured mobility values in excess of  $2000 \, \mathrm{cm}^2/\mathrm{Vs}$  are an order of magnitude lower than some of the highest values reported for single layer graphene on SiO<sub>2</sub>, [55] but well in the range of values reported for

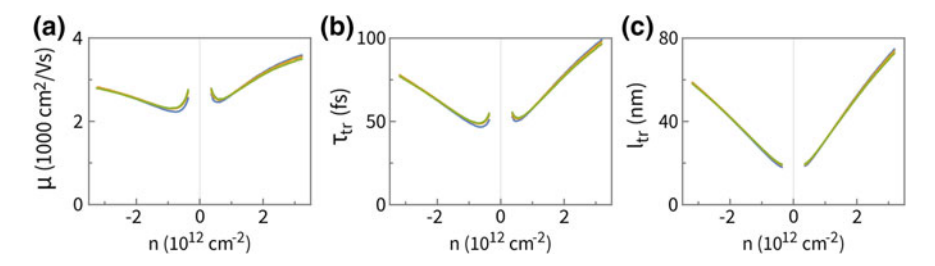


Fig. 2.8 Charge carrier mobility  $\mu$  (a), transport time  $\tau_{\rm tr}$  (b), and mean free path l (c) as a function of the charge carrier density n for the three different sections of the bilayer graphene device shown in Fig. 2.6a at  $T=1.4\,{\rm K}$ 

bilayer graphene devices [54]. The lower mobility has been related to the greater importance of scattering from charged impurities in bilayer graphene [53].

We can also extract the transport time  $\tau_{\rm tr} = \mu m^*/e$  of bilayer graphene, where  $m^*$  is determined using Eq. 2.5 from considering the approximative band dispersion (Eq. 2.3). Within the accessible charge carrier density range  $|n| < 3.5 \cdot 10^{12} \, {\rm cm}^{-2}$ ,  $m^*$  is however almost constant with its zero-density value being  $m^* \approx 0.033 \cdot m_e$ , see Fig. 2.4. Hence, the dependence of  $\tau_{\rm tr}$  on n largely reflects the behavior of  $\mu(n)$ , see Fig. 2.8b. The transport time  $\tau_{\rm tr}$  is on the order of  $\approx 50-100$  fs and increases with increasing |n|. The order of magnitude is in agreement with typical low-temperature values observed in bulk conductors [56].

In Fig. 2.8c, we further plot the mean free path  $l_{\rm tr} = v_F \cdot \tau_{\rm tr}$  between collisions.  $l_{\rm tr}$  reflects the strong increase of  $v_F(|n|)$  and the overall increase of  $\tau_{\rm tr}(|n|)$  for  $|n| \gg n_{eh}$  in the given range of n, i.e., the value of  $l_{\rm tr}$  is smallest (largest) near (far away from) the charge neutrality point. In comparison with the lateral dimensions of the bilayer graphene device (see Fig. 2.6a),  $l_{\rm tr}$  is more than one order of magnitude smaller. The charge carrier transport is thus in the diffusive regime, validating a posteriori the application of the Drude model. This is the case for all samples studied in this work.

## 2.6 Classical Magnetotransport

The discussion on charge carrier transport in the presence of an applied magnetic field  $\mathbf{B}$  is restricted hereafter to the situation where  $\mathbf{B} = (0, 0, B)^T$  only has a z-component oriented perpendicular to a two-dimensional transport layer in the x-y-plane with a current I flowing in x-direction, as applies to bilayer graphene in our case, see Fig. 2.6a. Within the Drude model, due to the Lorentz force  $\mathbf{F} = q\mathbf{v} \times \mathbf{B}$  acting on the charge carriers with charge q per carrier and velocity  $\mathbf{v}$ , the resistivity acquires a tensorial form  $\hat{\boldsymbol{\rho}}$  with longitudinal and transverse components  $\rho_{xx} = \rho_{yy}$  and  $\rho_{xy} = -\rho_{yx}$ , respectively:

$$\hat{\boldsymbol{\rho}} = \begin{pmatrix} \rho_{xx} & \rho_{xy} \\ \rho_{yx} & \rho_{yy} \end{pmatrix} = \begin{pmatrix} \rho_{xx} & \rho_{xy} \\ -\rho_{xy} & \rho_{xx} \end{pmatrix}.$$

It can be shown that for the case of a single charge carrier type of density n per unit area participating in the current [56]

$$\rho_{xx} = \rho_0$$
 and  $\rho_{xy} = \frac{B}{nq} = R_H B,$  (2.14)

where  $\rho_0 = m^*/(ne^2\tau_{tr})$  is the zero-field resistivity (using Eqs. 2.10 and 2.11) and  $R_H = 1/nq$  is a material parameter, the so-called Hall coefficient. The longitudinal resistivity  $\rho_{xx}$  remains unchanged, since in equilibrium the transverse field associated with the Hall voltage  $U_{xy} = I\rho_{xy}$  balances the Lorentz force. The most prominent result of this so-called Hall effect is the linear dependence of  $\rho_{xy}(B)$ , the slope of which gives access to both sign and density of the charge carriers. Knowing the sign of the charge carriers, we adopt a common practice from the field of research on 2D electron systems: in the figures shown in this work, we plot  $\rho_{xy} > 0$  at B > 0 for electron transport, respectively  $\rho_{xy} < 0$  at B > 0 for hole transport.

 $\rho_{xx}$  and  $\rho_{xy}$  are related to the longitudinal and transverse resistances  $R_{xx}$  and  $R_{xy}$ , conveniently measurable in a four-probe configuration when using a Hall bar geometry as shown in Fig. 2.6a. Taking the geometry into account, these quantities are related as follows:

$$\rho_{xx} = \frac{W}{L} \cdot R_{xx}$$
 and  $\rho_{xy} = R_{xy}$ ,

where W and L are the probed sample width and length, respectively.<sup>5</sup>  $\hat{\rho}$  relates to the conductivity tensor

$$\hat{\boldsymbol{\sigma}} = \begin{pmatrix} \sigma_{xx} & \sigma_{xy} \\ \sigma_{yx} & \sigma_{yy} \end{pmatrix} = \begin{pmatrix} \sigma_{xx} & \sigma_{xy} \\ -\sigma_{xy} & \sigma_{xx} \end{pmatrix}$$

as  $\hat{\boldsymbol{\rho}} = \hat{\boldsymbol{\sigma}}^{-1}$ , i.e.,

$$\sigma_{xx} = \frac{\rho_{xx}}{\rho_{xx}^2 + \rho_{xy}^2}$$
 and  $\sigma_{xy} = \frac{-\rho_{xy}}{\rho_{xx}^2 + \rho_{xy}^2}$ . (2.15)

It follows that

$$\sigma_{xx} = \frac{\sigma_0}{1 + (\omega_c \tau_{tr})^2} \quad \text{and} \quad \sigma_{xy} = -\frac{\sigma_0 \omega_c \tau_{tr}}{1 + (\omega_c \tau_{tr})^2}, \quad (2.16)$$

<sup>&</sup>lt;sup>5</sup>Dimensions and aspect ratios of the used Hall bars were optimized in order to minimize errors of geometrical origin [57].

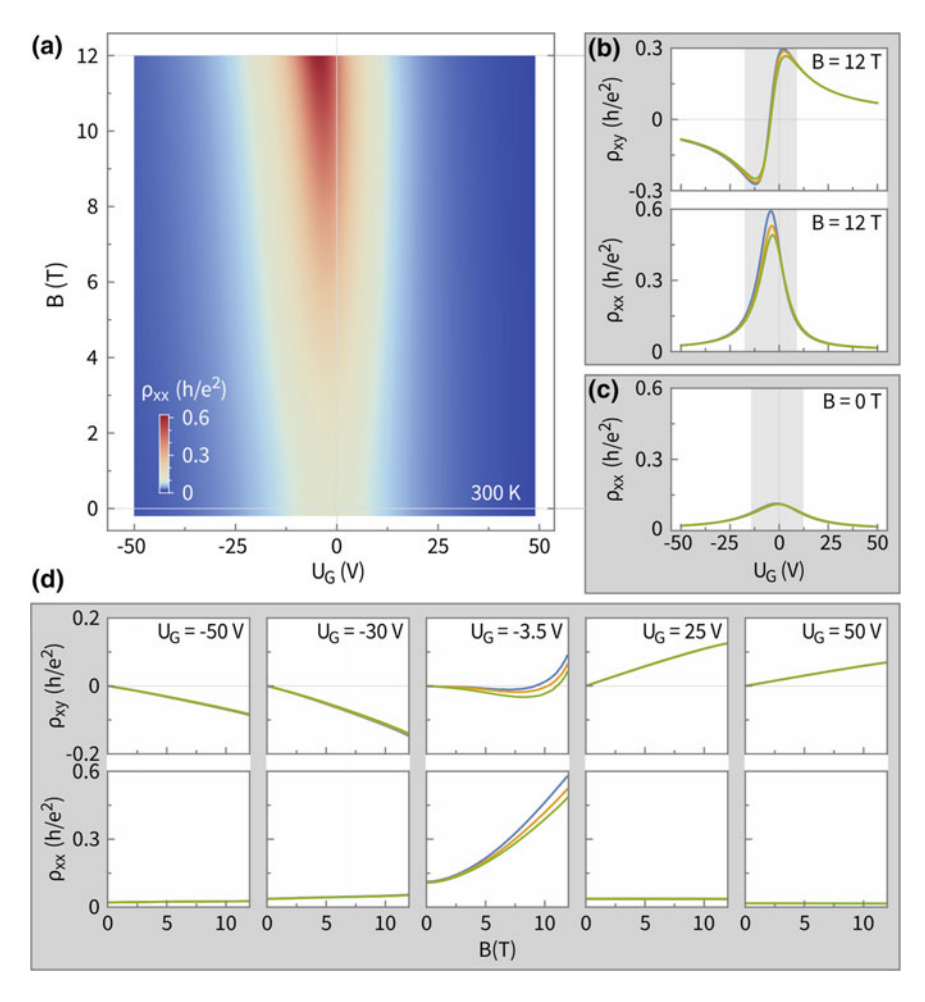


Fig. 2.9 Magnetotransport of charge carriers in the bilayer graphene device shown in Fig. 2.6a at 300 K. a False color plot of the longitudinal resistivity  $\rho_{xx}$  as a function of applied backgate voltage  $U_G$  and magnetic field B measured in device section i=1. b-d Line traces of  $\rho_{xx}$  and  $\rho_{xy}$  at (b)  $B=12\,\mathrm{T}$ , c  $B=0\,\mathrm{T}$ , and d different values of  $U_G$ . The three different line colors correspond to the three different sections of the device as denominated in Fig. 2.6a

where we use the zero-field conductivity  $\sigma_0 = 1/\rho_0 = ne^2 \tau_{\rm tr}/m^*$  and  $\omega_c \tau_{\rm tr} = \mu B$  with the cyclotron frequency  $\omega_c = |q|B/m^*$ .

We briefly discuss the room-temperature magnetotransport behavior of charge carriers in the bilayer graphene device shown in Fig. 2.6a based on measured data given in Fig. 2.9. Here, both  $\rho_{xx}$  and  $\rho_{xy}$  are plotted in units of  $h/e^2 \approx 25.812, 81 \Omega$ . The three colors of the line traces correspond to the three different sections  $i = \{1, 2, 3\}$  of the device, as in Fig. 2.6. Figure 2.9a is a false color plot of  $\rho_{xx}$  measured as a function of applied backgate voltage  $U_G$  and magnetic field strength B in section

i=1. Two line traces of  $\rho_{xx}$ , extracted at  $B=12\,\mathrm{T}$  and  $B=0\,\mathrm{T}$ , are additionally plotted in Fig. 2.9b, c, respectively, showing little spread among the different sections of the device. The zero-field traces in Fig. 2.9c compare to the room-temperature data in Fig. 2.6d, featuring a single maximum in  $\rho_{xx}$  at charge neutrality (at  $U_{\text{CNP}i}$  with  $i = \{1, 2, 3\}$ ) and a decrease in  $\rho_{xx}$  approximately symmetric in  $U_G$  with respect to  $U_{\text{CNP}_i}$ . The same holds for  $\rho_{xx}(U_G)$  measured at all accessible magnetic field values, see Fig. 2.9a.<sup>6</sup> At  $U_G \gg U_{\text{CNP,i}}$  ( $U_G \ll U_{\text{CNP,i}}$ ) we observe no significant dependence of  $\rho_{xx}$  on B, as only electrons (holes) participate in the charge carrier transport and the Drude model applies. This is most apparent in the  $\rho_{xx}(B)$  traces shown in Fig. 2.9d, extracted at  $U_G = -50 \text{ V}, -30 \text{ V}, 25 \text{ V}, \text{ and } 50 \text{ V}$ . As expected, the associated traces of  $\rho_{xy}(B)$ , however, show a linear B-field dependence in agreement with Eq. 2.14. According to the sign of the slope, the charge carriers at  $U_G \gg U_{\text{CNPi}} (U_G \ll U_{\text{CNPi}})$ are clearly electrons (holes), respectively. Extracting the charge carrier densities  $n(U_G)$  from this data by applying Eq. 2.14, one may confirm the estimation of  $n(U_G)$ from the capacitive model introduced in Sect. 2.5 [9]. While the agreement is typically good, the Hall measurement yields the more exact values.

When tuning  $U_G$  across the charge neutrality point,  $\rho_{xy}(U_G)$  features a smooth zero crossing due to the coexistence of both electrons and holes (see Fig. 2.9b), analogous to observations in single layer graphene [49]. Concomitantly, a longitudinal magnetoresistance  $\rho_{xx}$  is observed, significant however only within an interval  $\Delta U_G$  around the charge neutrality point as highlighted by the grey shaded area in the figure. According to the central panel of Fig. 2.9d,  $\rho_{xx}(B)$  measured at  $U_G = -3.5$  V shows a quadratic dependence on B, and possibly a transition to a linear magnetoresistance at high values of B. A similar measurement on bilayer graphene was reported by Vasileva et al. [58], who demonstrate that this magnetotransport behavior can be captured within a two-fluid model adopted from Ref. [59]. As throughout this work we shall not focus on this low-charge carrier density region of the transport, we refer the interested reader to Refs. [58, 59] for more details.

## 2.7 Quantum Magnetotransport

At low temperatures T, the magnetotransport behavior of charge carriers tends to show a significantly different behavior than near room temperature, since quantum effects get increasingly important. The understanding of these effects is relevant, as their accurate description gives direct access to key parameters of the system. The most pronounced effects observable in our bilayer graphene devices are Shubnikov-de Haas (SdH) oscillations, the integer quantum Hall effect (IQHE), as well as quantum interference (QI) corrections to the conductivity. In this work, the first two are

<sup>&</sup>lt;sup>6</sup>A slight shift of the charge neutrality point as a function of time (seemingly as a function of *B*, sweeped from high to low values in our experiment) might be related to recontamination of bilayer graphene by adsorbates during this room-temperature measurement, performed in our cryogen-free magnet system with the sample space warmed-up after weeks of low-temperature measurements.

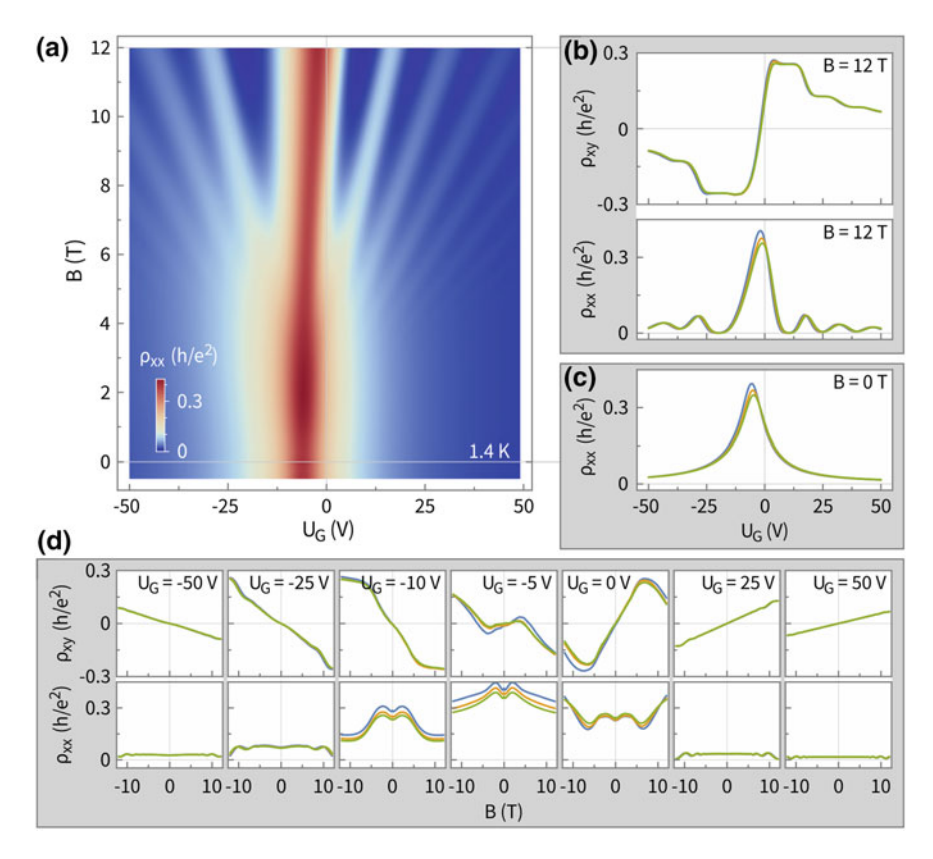


Fig. 2.10 Magnetotransport of charge carriers in the bilayer graphene device shown in Fig. 2.6a at 1.4 K. a False color plot of the longitudinal resistivity  $\rho_{xx}$  as a function of applied backgate voltage  $U_G$  and magnetic field B measured in device section i = 1. b–d Line traces of  $\rho_{xx}$  and  $\rho_{xy}$  at (b) B = 12 T, c B = 0 T, and d different values of  $U_G$ . The three different line colors correspond to the three different sections of the device as denominated in Fig. 2.6a

mainly considered for characterization purposes, with SdH oscillations providing access to the density n, the mobility  $\mu$ , and the effective mass  $m^*$  of the charge carriers, and the IQHE being a characteristic of bilayer graphene's unique electronic structure. The manifestation of QIs bears information about several time scales governing the charge carrier transport in bilayer graphene, and is the subject of Chap. 5. Here, we restrict ourselves to first giving an overview on the magnetotransport of charge carriers in bilayer graphene, as measured in the device shown in Fig. 2.6a at T=1.4 K, see Fig. 2.10. We then briefly discuss SdH oscillations in Sect. 2.7.1, the IQHE in Sect. 2.7.2, and QIs in Sect. 2.7.3. In each of these sections, the emphasis is on the phenomenology of these effects in our magnetotransport measurements and which information, relevant to this work, we can extract.

Figure 2.10 summarizes the dependence of  $\rho_{xx}$  and  $\rho_{xy}$  on the applied magnetic field strength B as well as the backgate voltage  $U_G$  at 1.4 K, analogous to the presen-

tation of the room temperature data in Fig. 2.9. Again, both  $\rho_{xx}$  and  $\rho_{xy}$  are plotted in units of  $h/e^2 \approx 25.812, 81 \Omega$ , and the three colors of the line traces correspond to the three sections  $i = \{1, 2, 3\}$  of the device, as in Fig. 2.6. At first glance, the false color plot of  $\rho_{xx}$  in Fig. 2.10a demonstrates a strikingly different behavior of the charge carriers than at room temperature (Fig. 2.9a). The familiar dependence of  $\rho_{xx}(U_G)$  at B = 0 T (compare Fig. 2.10c to Fig. 2.6b) evolves into a more complicated lineshape at  $B = 12 \,\mathrm{T}$ , see Fig. 2.10b. Here, next to a resistance maximum at charge neutrality ( $U_{\text{CNP}i}$  for the three segments  $i = \{1, 2, 3\}$ ), we observe additional maxima of decreasing magnitude as  $|U_G|$  is tuned away from  $U_{\text{CNPi}}$ . In between some of them, regions of zero longitudinal resistivity  $\rho_{xx}$  are accompanied by plateaus in the Hall resistivity  $\rho_{xy}$ , a manifestation of the IQHE [26, 60]. Maxima and minima in  $\rho_{xx}$  are observed down to  $B \approx 4 \,\mathrm{T}$ . These are SdH oscillations, apparent especially in the line traces  $\rho_{xx}(B)$  at fixed values of  $U_G$  in Fig. 2.10d. In the central three panels of this figure, the trained eye may recognize a tiny peak in  $\rho_{xx}$  around B = 0 T, which is caused by QIs. Our data in Fig. 2.10 is representative of other magnetotransport measurements on bilayer graphene reported in the literature [26, 58]. The apparent shift of the charge neutrality point with B (see Fig. 2.10a) might be related to electron-hole asymmetry and to the Hall resistivity being a non-monotonous function of B in the electron-hole puddle regime [58]. In this work we shall, however, focus on regions in charge carrier density where a single charge carrier type dominates the transport. This clearly applies to the data taken at  $|U_G| \ge 25 \,\mathrm{V}$  in Fig. 2.10d, where the traces of  $\rho_{xy}$  retain their overall linear dependence on B as observed at room temperature in Fig. 2.9d, in accordance with Eq. 2.14.

#### 2.7.1 Shubnikov-De Haas Oscillations

Shubnikov-de Haas (SdH) oscillations in the longitudinal magnetoresistivity are caused by the B-dependent variation in the chemical potential due to Landau quantization as introduced in Sect. 2.4. Resistivity minima (maxima) appear when the Fermi energy  $\epsilon_F$  resides in between Landau levels (in the center of a Landau level). In order for SdH oscillations to be observed, Landau level (LL) broadening must be overcome. The latter is set by the quantum lifetime  $\tau_q$ , which is a measure of how long a charge carrier remains in a momentum eigenstate in the presence of scattering [61, 62]. From the onset of SdH oscillations in B one may derive the so-called quantum mobility  $\mu_q$  as the uncertainty principle requires LL broadening in energy due to charge carrier scattering,  $\Delta \epsilon = \hbar/\tau_q$ , to be smaller than the cyclotron energy  $\hbar \omega_c$  (gap between neighboring LLs) where  $\omega_c = eB/m^*$ , i.e. (using Eq. 2.11),

$$\mu_a B \gg 1. \tag{2.17}$$

<sup>&</sup>lt;sup>7</sup>In contrast to the transport time  $\tau_{tr}$  it takes into account the total scattering probability, while the former is weighted toward large-angle scattering.

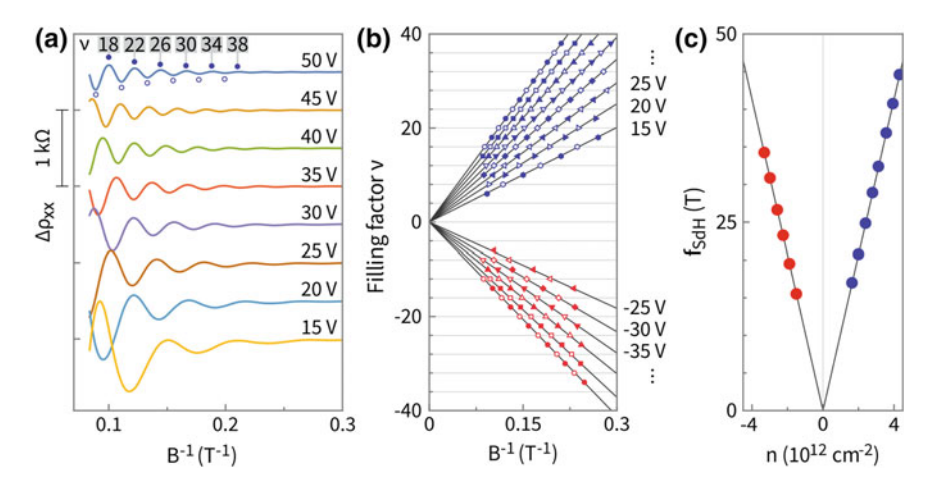


Fig. 2.11 Shubnikov-de Haas (SdH) oscillations measured at different backgate voltages  $|U_G| \le 50 \text{ V}$ . The data is recorded in Sect. 1 of the bilayer graphene device shown in Fig. 2.6a. **a**  $\Delta \rho_{xx}$  values at T=1.4 K plotted with a constant offset. Minima (open symbols) and maxima (filled symbols) of SdH oscillations with associated filling factors  $\nu$ . **b** Filling factor fan chart of the extracted minima (open symbols) and maxima (filled symbols) of the SdH oscillations ( $\Delta \rho_{xx}$ ). **c** Frequency  $f_{\text{SdH}}$  of SdH oscillations as a function of charge carrier density n

Figure 2.11 shows SdH oscillations in the longitudinal magnetoresistivity measured in section i = 1 of the bilayer graphene device shown in Fig. 2.6a at different values of the applied backgate voltage  $U_G$ . In Fig. 2.11a the variation in the magnetoresistivity  $\Delta \rho_{xx}$  is plotted as function of inverse magnetic field strength  $B^{-1}$ for  $U_G = 15 \,\mathrm{V}, \ldots, 50 \,\mathrm{V}$ . The gate voltage is varied in steps of 5 V and the data is recorded at T = 1.4 K. SdH oscillations with a single frequency component  $f_{SdH}$  can clearly be seen in each data set starting from  $B \approx 4 \,\mathrm{T}$  (compare with Fig. 2.10) yielding  $\mu_a \approx 2500 \, \mathrm{cm}^2/\mathrm{Vs}$  on the same order of magnitude as values of  $\mu$  in Fig. 2.8a. Minima (open symbols) and maxima (filled symbols) can directly be extracted as illustrated for the trace at  $U_G = 50 \,\mathrm{V}$ . Using the charge carrier density n extracted from a simultaneous measurement of the Hall voltage, one can determine the filling factor v = nh/Be (number of filled LLs) for each value of B as indicated in the figure. The step size of  $\Delta \nu = 4$  between adjacent maxima (or minima) of the SdH oscillations evidences the fourfold degeneracy  $\delta = 4$  of the LLs in bilayer graphene. This allows us to calculate the charge carrier density n directly from each SdH oscillation as

$$n = \frac{\delta}{\Phi_0} \cdot f_{\text{SdH}} = \frac{4 \cdot e}{h} \cdot f_{\text{SdH}}.$$
 (2.18)

According to Eq. 2.18, a complementary approach to identify  $\delta$  is to plot  $f_{\rm SdH}$  as a function of n, see Fig. 2.11c. For both electrons and holes, we can extract a linear dependence  $f_{\rm SdH} = \beta |n|$  with  $\beta = (1.03 \pm 0.01) \cdot 10^{-15}$  Tm<sup>2</sup>. Since  $\beta = \Phi_0/\delta$  with  $\Phi_0 = h/e \approx 4.14 \cdot 10^{-15}$  Tm<sup>2</sup>, we get  $\delta = 4$ .

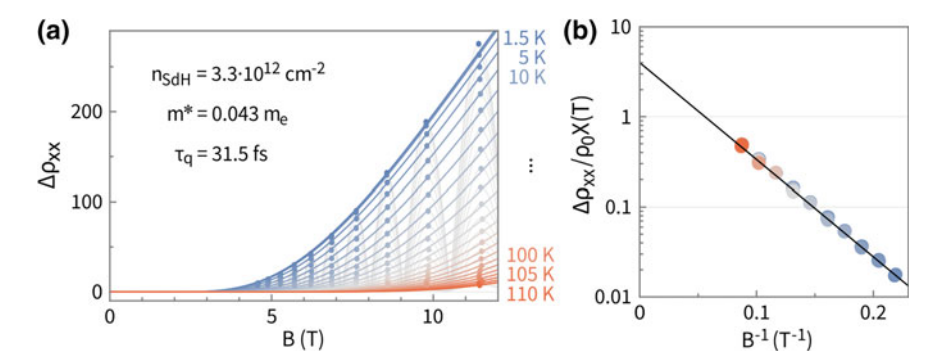


Fig. 2.12 Temperature dependence of SdH oscillation amplitudes at an electron density  $n_{\rm SdH} = 3.3 \cdot 10^{12} \, {\rm cm}^{-2}$ . Data was recorded between  $T = 1.4 \, {\rm K}$  and  $T = 110 \, {\rm K}$  in steps of 5 K from  $T = 5 \, {\rm K}$ . a Amplitude of SdH oscillations  $\Delta \rho_{xx}$  (light grey lines), positions of extrema (dots), and fits to Eq. 2.19 (solid colored lines) using the given values for  $m^*$  and  $\tau_q$ . b Dingle plot: The SdH oscillation amplitude  $\Delta \rho_{xx}$  normalized by  $\rho_0(T)$  and corrected for thermal damping by X(T) plotted against reciprocal field. The solid line is a fit to the data constrained to go through the theoretical value of 4 at  $B^{-1} = 0$ 

We can further prove the trivial Berry phase  $\Phi_B$  in bilayer graphene as follows. In the fan chart shown in Fig. 2.11b open (filled) symbols represent minima (maxima) of the SdH oscillations in  $\rho_{xx}(B)$ . At each value of  $U_G$ , the points fall on straight lines extrapolating to  $\nu = 0$  at  $B^{-1} = 0$ . Minima of SdH oscillations in bilayer graphene are found at integer multiples of  $\delta$ , corresponding to the conventional case of SdH oscillations in a 2DES with a parabolic band dispersion [63]. Despite the same LL degeneracy  $\delta$ , in single layer graphene the oscillations would be shifted featuring maxima instead of minima in  $\rho_{xx}(B)$  at integer multiples of  $\delta$ , due to the non-trivial Berry phase  $\Phi_B = \pi$  [9, 10].

SdH oscillations also provide a measure of the effective mass  $m^*$ , which we may extract together with the quantum lifetime  $\tau_{\rm q}$  from the temperature dependent amplitude  $\Delta\rho_{xx}$ . As an example, we measured SdH oscillations at an electron density of  $n_{\rm SdH}=3.3\cdot 10^{12}\,{\rm cm}^{-2}$  (determined according to Eq. 2.18) at  $T=1.4\,{\rm K}$  as well as between  $T=5\,{\rm K}$  and  $T=110\,{\rm K}$  in steps of 5 K. After subtracting the non-oscillating component of each trace  $\rho_{xx}(B)$ , we plot the absolute value of SdH oscillations as grey lines in Fig. 2.12a. The dependence of the oscillation amplitude  $\Delta\rho_{xx}$  on B and T can be described as [64]

$$\Delta \rho_{xx} = 4\rho_0 X(T) \exp\left(-\frac{\pi}{\omega_c \tau_q}\right), \quad \text{with} \quad X(T) = \frac{2\pi^2 k_B T/\hbar \omega_c}{\sinh\left(2\pi^2 k_B T/\hbar \omega_c\right)}. \quad (2.19)$$

Here, X(T) is a thermal damping factor and  $k_B$  is the Boltzmann constant. We identify well-resolved extrema of the oscillations (dots in Fig. 2.12a) in order to find a least-square fit of  $\Delta \rho_{xx}(B)$  for all temperatures simultaneously, using Eq. 2.19 with  $m^*$  and  $\tau_q$  as the only free parameters. The best fit (solid colored lines in the figure) is obtained using  $m^* = 0.043 \cdot m_e$  and  $\tau_q = 31.5$  fs. The Dingle plot of

 $\Delta \rho_{xx}$  normalized by  $\rho_0(T)$  and corrected for temperature by X(T) in Fig. 2.12b demonstrates the accurate description of SdH oscillation amplitudes by Eq. 2.19 using these parameters.

From this analysis we learn that at the given electron density,  $m^*$  is in fact  $\approx 10\%$  smaller than what we expect according to our description in Sect. 2.3. This finding is in close agreement with an analysis from Zou et al. [24] and could be accounted for when using different values of the bilayer graphene band structure parameters  $\gamma_0$  and  $\gamma_4$  (stated in Table 2.1), the latter of which we neglect altogether in our simplified band description (Eq. 2.3). The extracted value of the quantum lifetime  $\tau_q = 31.5$  fs is in good agreement with values reported for both single and bilayer graphene samples on SiO<sub>2</sub> [24, 62]. When compared to the transport time, which we determine to be  $\tau_{tr} = 84$  fs using Eqs. 2.16 and 2.11 with both  $m^*$  and  $n_{SdH}$  as extracted in the preceding analysis, we obtain the ratio  $\tau_{tr}/\tau_q = 2.67$ . This is a representative value for graphene samples prepared on SiO<sub>2</sub> and identifies long-ranged disorder potentials to dominate charge carrier scattering [62]. In addition to charged impurities, random strain fluctuations are likely their major source [46, 65]. Further support for this assertion is given in Chap. 5.

#### 2.7.2 Integer Quantum Hall Effect

At high magnetic fields, the minima of SdH oscillations in  $\rho_{xx}$  develop into extended regions in B and n with zero longitudinal resistivity as can be seen in Fig. 2.10a, b. They are accompanied by plateaus in the Hall resistivity with values  $\rho_{xy} = h/e^2 \cdot \nu^{-1}$ , where  $\nu$  is a non-zero integer. This is the so-called integer quantum Hall effect (IQHE) [60]. Using Eq. 2.15 with  $\rho_{xx} = 0$ , it follows that  $\sigma_{xy} = -\rho_{xy}^{-1}$ . The exact sequence of plateaus observed in an experiment depends on the Landau level (LL) degeneracy  $\delta$ . In single layer graphene,  $\delta = 4$  (two spin and two valley degrees of freedom, see Sect. 2.4) leads to a ladder of equal steps in  $\sigma_{xy}$  with  $\Delta \sigma_{xy} = \delta \cdot e^2/h = 4e^2/h$ , [9, 10] see the red line in Fig. 2.13a. Due to the zeroth LL being shared in equal parts by electrons and holes, plateaus appear around integer filling factors  $\nu = \pm 2, \pm 4, \pm 10...$  [9, 10]. In bilayer graphene,  $\delta = 4$  is retained except for the eightfold degeneracy of the zeroth LL (two spin, two valley, and two orbital degrees of freedom, see Sect. 2.4). One observes a single corresponding step of  $\Delta \sigma_{xy} = 8e^2/h$  and plateaus in  $\sigma_{xy}$  around  $\nu = \pm 4, \pm 8, \pm 12...$ , [26] see the green line in Fig. 2.13a.

According to Ref. [66], multilayers consisting of N Bernal-stacked graphene sheets should in fact show plateaus at

$$\sigma_{xy} = \pm \frac{4e^2}{h} \left( \frac{N}{2} + M \right), \tag{2.20}$$

where M is a non-negative integer. This finding is a consequence of the pseudospin winding number (or degree of chirality) of the charge carriers in the respec-

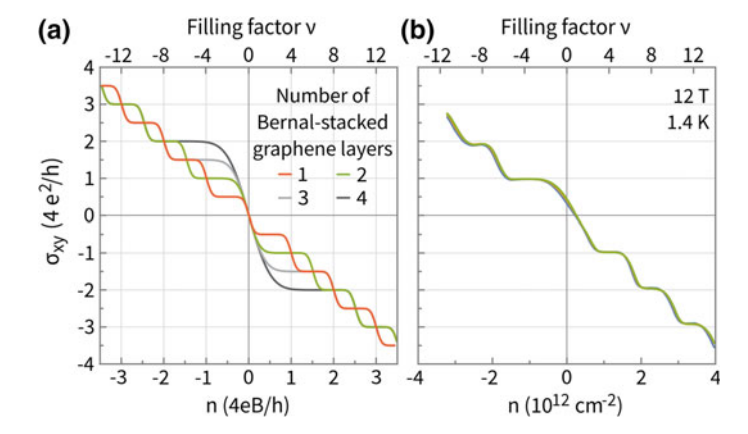


**Fig. 2.13** Manifestation of the integer quantum Hall effect (IQHE) in the transverse magnetoconductivity  $\sigma_{xy}$  as a function of charge carrier density n or filling factor v at a fixed value of B. a Schematic traces of  $\sigma_{xy}(n)$  expected for single layer graphene and for 2, 3, and 4 Bernal-stacked graphene layers. b  $\sigma_{xy}(n)$  of the bilayer graphene device shown in Fig. 2.6a, measured at B = 12 T and T = 1.4 K

tive material [7, 66]. The 4N-fold degeneracy of the zeroth LL (respectively the difference between the positive and negative solution of Eq. 2.20 for M=0, i.e.,  $\Delta \sigma_{xy} = N \cdot 4e^2/h$ ) is obviously a characteristic of the number N of Bernal-stacked layers. For 3-layer graphene and 4-layer graphene, the accordingly expected values of  $\Delta \sigma_{xy} = 12e^2/h$  and  $\Delta \sigma_{xy} = 16e^2/h$  have been experimentally verified, see Refs. [67–69]. Corresponding schematic traces of  $\sigma_{xy}$  are shown in Fig. 2.13a.

We convert our data of  $\rho_{xy}$  and  $\rho_{xx}$  shown in Fig. 2.10b, measured as a function of backgate voltage  $U_G$  and at  $B=12\,\mathrm{T}$ , to the magnetoconductivity  $\sigma_{xy}$  using Eq. 2.15. The obtained traces are plotted in Fig. 2.13b as a function of charge carrier density n, calculated from  $U_G$  using the plate capacitor model (Eq. 2.13). The non-zero value of  $\sigma_{xy}$  at charge neutrality may be related to electron-hole asymmetry [58]. We observe well-developed plateaus at  $-8e^2/h$ ,  $-4e^2/h$ ,  $4e^2/h$ ,  $8e^2/h$ , and  $12e^2/h$ , i.e., at filling factors  $\nu=\pm 4,\pm 8$ , and  $\pm 12$ . This sequence is a distinct characteristic of bilayer graphene. The IQHE thus provides a tool to identify the number of layers of a few-layer graphene sample.

# 2.7.3 Quantum Interferences

Interferences between different paths of diffusively propagating charge carriers in a 2D system can induce corrections to its Drude conductivity [70]. For these corrections to appear, charge carriers need to maintain phase coherence during their motion and time-reversal symmetry should hold. Then, the probability amplitudes associated with their travelling along different paths may yield a net interference. The important

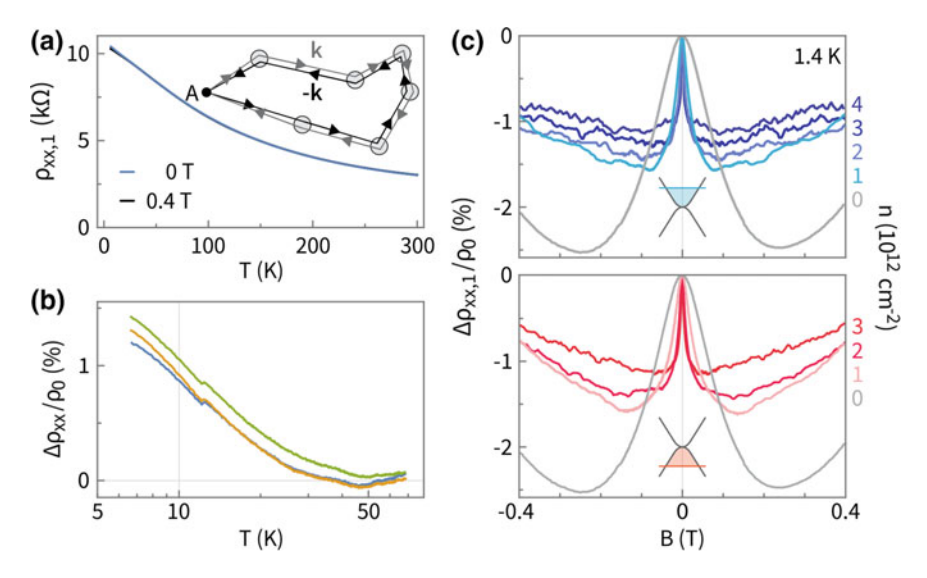


Fig. 2.14 Quantum interferences (QIs) in the bilayer graphene device shown in Fig. 2.6a. a Temperature dependence of the longitudinal resistivity  $\rho_{xx,1}$  measured in Sect. 1 of the device at charge neutrality and both at B=0T (blue line) and at B=0.4T (black line). Corrections from QIs are suppressed at B=0.4T. Closed counter-propagating charge carrier trajectories, relevant for QIs, are schematically shown as an inset (grey circles are elastic scattering events). b Temperature dependence of QI-caused corrections to  $\rho_{xx}$  at charge neutrality: plotted is  $[\rho_{xx}(B=0)-\rho_{xx}(B=0.4\text{ T})]/\rho_{xx}(B=0)$  for all three sections of the device. c Magnetic field dependence of  $\rho_{xx}$  showing suppression of QI corrections measured at T=1.4 K for different charge carrier densities n. Plotted is  $[\rho_{xx,1}(B)-\rho_{xx,1}(B=0)]/\rho_{xx,1}(B=0)$  for electrons (upper panel, blue traces), holes (lower panel, red traces), as well as for the electron-hole puddle regime (grey traces)

paths to be considered are closed trajectories of counter-propagating sense, as illustrated in the inset to Fig. 2.14a. Here, a trajectory starting at point A returns to point A via a sequence of scattering events (grey circles), either in clockwise or counterclockwise direction. Depending on details of the system, the interference between such two paths can be either constructive or destructive, resulting in an increased or a reduced probability of backscattering, respectively. Consequently, the conductivity is either reduced or enhanced, two phenomenological results called weak localization and weak anti-localization, respectively. The first scenario is found to generally apply to bilayer graphene, [71, 72] and we shall give a short introduction to its phenomenology in the following.

Figure 2.14 summarizes data measured in the device shown in Fig. 2.6a. At decreasing temperatures T, where the phase coherence length  $l_{\phi}$  gets large due to the suppression of phase-randomizing inelastic scattering events, quantum interference (QI) corrections to  $\rho_{xx}$  are readily evidenced by the application of a small out-of-plane magnetic field B. The presence of B breaks time-reversal symmetry and destroys the interference between the two counter-propagating trajecto-

ries by adding an additional phase. In Fig. 2.14a, b, the effect of QIs is revealed as the difference in longitudinal resistivity  $\rho_{xx}$  measured as function of T both with and without an applied magnetic field  $B = 0.4 \,\mathrm{T}$ . A difference in resistivity  $[\rho_{xx}(B=0) - \rho_{xx}(B=0.4 \text{ T})]/\rho_{xx}(B=0)$  on the order of 1%, representative for all samples measured in this work, can be observed. In agreement with theory, [73] the correction actually shows a logarithmic temperature dependence (here for  $T < 30 \,\mathrm{K}$ ), see Fig. 2.14b. Alternatively, one may probe QIs by sweeping B at a fixed temperature T, as shown in Fig. 2.14c. Here, a peak at B = 0 is revealed in the longitudinal magnetoresistivity measured at  $T = 1.4 \,\mathrm{K}$ , plotted as  $[\rho_{xx,1}(B) - \rho_{xx,1}(B=0)]/\rho_{xx,1}(B=0)$ . The observed negative magnetoresistance at low values of B is characteristic for weak localization. The effect persists for all accessed charge carrier densities, with an overall symmetric appearance with respect to a change in carrier type from electrons to holes of the same density (compare upper and lower panel of Fig. 2.14c). In the electron-hole puddle regime near charge neutrality (grey solid line), two charge carrier types contribute to the QI effect. As this regime is not of primary interest to this work, we only note that if a two-band model was to apply in this case, an enhancement of the effect could be expected, [74] which would be in line with our observation.

QIs can thus be readily probed in our bilayer graphene devices, experimentally most conveniently by performing a sweep of B in the low field region as shown in Fig. 2.14c. We shall defer the more detailed discussion to Chap. 5, as the mechanism of QIs is best discussed in detailed comparison to the case of single layer graphene. We close by noting that its theoretical description provides access to characteristic time scales governing the charge carrier transport. The time scale related to elastic scattering of charge carriers between valleys,  $\tau_i$ , will prove to be sensitive to the presence or absence of Li-ions in between the two carbon sheets of bilayer graphene, thus representing a probe to verify their successful intercalation.

## 2.8 Raman Scattering

A different means used in this work to gain information about the electronic properties of graphene systems is the inelastic scattering of light in the visible range, i.e., with photon energies on the order of 1.5-3 eV. With a much lower probability than elastic scattering, a photon of energy  $\hbar\omega_i$  and momentum  $k_i$  incident on graphene can be scattered into a state of energy  $\hbar\omega_s$  and momentum  $k_s$  by one of various processes such as the ones depicted in Fig. 2.15. These processes are inelastic, because the energy of the scattered photon  $\hbar\omega_s$  is smaller than the one of the incident photon  $\hbar\omega_i$  (a so-called Stokes Raman scattering process). The difference in energy is transferred to the graphene system, here in the form of emitted phonons. Importantly, as can be seen in Fig. 2.15, the scattering processes are mediated by excitations in the electronic system. Because these excitations are short-lived, in general they need not correspond to a stationary state of the system, as long as the overall process fulfills energy and momentum conservation. However, due to the absence of a (at

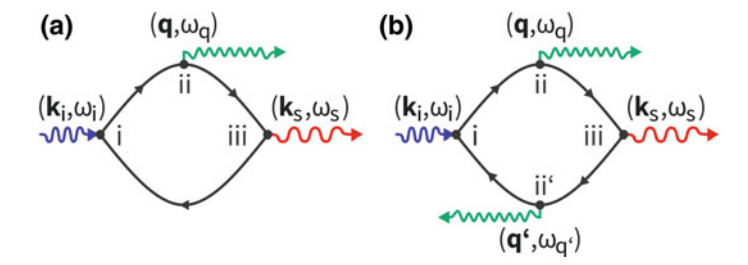


**Fig. 2.15** Feynman diagrams of important contributions to Stokes Raman processes of **a** 1st order and **b** 2nd order. (i) An incident photon (blue line) creates an electron-hole pair (black lines) which decays to another electron-hole pair by (ii) emission of one or two phonons (green lines) before (iii) recombining under emission of a (scattered) photon (red line)

least significant) bandgap in graphene systems, an incident photon of energy  $\hbar\omega_i$  can always create an electron-hole pair in resonance with a real electronic state in the system. The cross-section of such a resonant process is greatly enhanced, explaining the good visibility of several characteristic Raman modes in graphene systems down to the single layer, [75] see Fig. 2.16a. The spectra are plotted as a function of the Raman shift  $\delta\omega = (\lambda_i^{-1} - \lambda_s^{-1})$ , where  $\lambda_i = 488$  nm and  $\lambda_s$  are the wavelengths of the incident and the scattered light, respectively. We will now briefly introduce a selection of three different Raman modes, relevant to this work for different reasons. More information on Raman spectroscopy of graphene systems can be found in Refs. [76, 77].

We first consider the dispersion of vibrational modes in single layer graphene, plotted in Fig. 2.16b along high-symmetry lines in the 1st Brillouin zone (1st BZ). The six phonon branches can be classified into three acoustic (A) and three optical (O) ones, which subdivide into transversal (T) and longitudinal (L) modes with associated in-plane (i) or out-of-plane (o) motion. Note that the branches with out-of-plane motion, oTA and oTO, are the lowest in energy among the acoustic and optical ones, respectively. This consistently reflects the strong in-plane sp<sup>2</sup>-bonding of the crystal, which significantly stiffens the in-plane vibrational modes. In few-layer graphene systems the phonon dispersion does not change considerably due to the weak interlayer interaction. I.e., while all phonon branches become doubly (threefold) degenerate in bilayer graphene and graphite (trilayer graphene), due to the greater number of atoms in the elementary unit cell, their energy remains almost unchanged with usually only a small splitting between degenerate branches  $\leq 20 \, \mathrm{cm}^{-1}$  [78].

This being said, we turn to the first Raman band, present in all graphitic carbon systems (see Fig. 2.16): the G band near  $\approx$ 1580 cm<sup>-1</sup>. It stems from a first order Raman scattering process as illustrated in Fig. 2.15a. It involves the doubly-degenerate (iTO and iLO) high-frequency optical  $E_{2g}$  phonon mode at  $\Gamma$ . The process as well as the atomic displacement pattern of the phonon are schematically shown in the first panel of Fig. 2.16c. Two exemplary scattering events are depicted to illustrate that this process is actually highly off-resonant [77]. Furthermore, the energy of the  $E_{2g}$ -phonon mode is strongly renormalized by interactions with charge carriers in the system. A

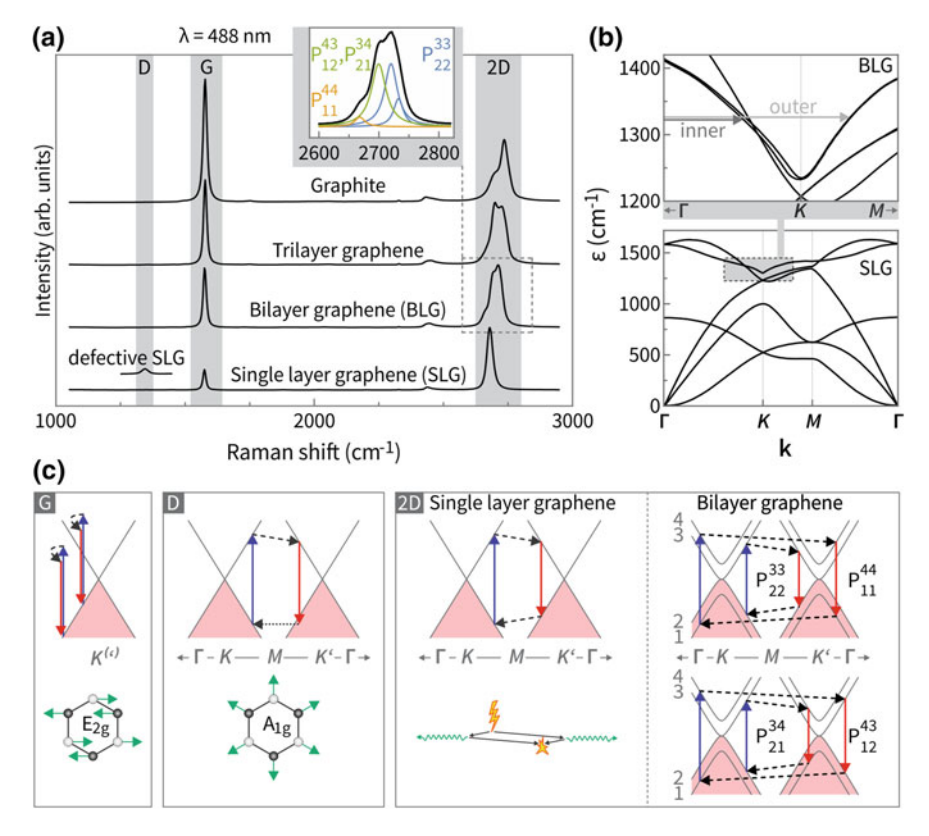


**Fig. 2.16** Raman scattering in graphene systems. **a** Raman scattering spectra measured on Bernal-stacked graphene with 1–3 layers and graphite. The inset is a fit to the experimental bilayer graphene 2D band with four Lorentzians, identified according to Ref. [79] with scattering processes as shown in panel c. Contributions to  $P_{22}^{33}$  split into inner and outer processes. **b** Calculated phonon dispersion for single layer graphene (SLG), with the oTA, iTA, iLA, oTO, iTO, and iLO phonon branches (bottom to top at  $\Gamma$ ). The inset shows the calculated phonon dispersion in the vicinity of K for bilayer graphene (BLG). **c** Processes for the Raman G, D, and 2D bands. Dispersion of electronic states near  $K^{(\prime)}$  (solid grey lines) with occupied states (red shaded areas). Interband transitions with photon absorption (solid blue arrows) and photon emission (solid red arrows). Transitions involving phonon emission (black dashed arrows) and scattering on a defect (black dotted arrow). Atom displacement patterns for the  $E_{2g}$  and  $A_{1g}$  phonon modes involved in the Raman G and D bands of single layer graphene. Real-space Raman process for the Raman 2D band (explained in the main text). Adapted with permission from Ref. [80] (panel b) and Ref. [79] (panels b, c). Copyright 2008 and 2014 by the American Physical Society, respectively. Panel c further adapted by permission from Springer Nature: Ref. [77], copyright 2013

change in their density for instance may affect both the energy and linewidth of the Raman G band [81–83]. This effect is central to Sect. 4.2.

The Raman D band at  $\approx 1300 \, \mathrm{cm}^{-1}$  involves scattering from an iTO phonon mode of momentum  $\boldsymbol{q}$  near  $\boldsymbol{K}$ , the atomic displacement pattern of which corresponds to the breathing-mode of the six-atom carbon rings. As depicted in the second panel of Fig. 2.16c, overall momentum conservation can only be fulfilled with the help of scattering from a defect with momentum transfer  $-\boldsymbol{q}$ . In the absence of defects, this process is suppressed, qualifying the magnitude of this band as a measure of the number of defects in the crystal.

Not defect-activated and therefore always observable is the D-peak overtone, the 2D band. As illustrated in the third panel of Fig. 2.16c, the scattering process yielding this band involves two iTO phonons with finite and opposite wave vector. The dominant triple-resonant electron-hole scattering processes, as depicted in Fig. 2.16c, can be identified considering Raman scattering in real-space [77]. The electron and hole created by the incident light (depicted by a lightning) travel in opposite directions until they are backscattered emitting phonons with opposite q. When they recombine (depicted by a flash), they have travelled total paths of equal length. In Bernal-stacked graphene consisting of more than a single layer, the situation is more complex due to the additional electronic bands available. Therefore, this Raman signal has been early on identified as bearing a strong fingerprint of the layer number [75]. In bilayer graphene, the four  $\pi$ -electronic bands enable different scattering mechanisms, denoted as  $P_{im}^{jl}$  in Fig. 2.16c, where we use the band index of the initial electron i, the excited electron j, the scattered electron l, and the scattered hole m. It was demonstrated, that the bilayer graphene 2D band can be decomposed into four characteristic contributions, [79] as shown in the fit to our experimental data in the inset to Fig. 2.16a.

#### 2.9 Summary

We have introduced the structural and electronic properties of bilayer graphene, both in the absence and in the presence of a quantizing magnetic field applied perpendicular to its carbon planes. As in single layer graphene, the charge carriers live in valleys at the K and K' points in the 1st Brillouin zone, however they show both a different dispersion and a different degree of chirality. Many of the related unique properties of this material can be revealed in the charge carrier transport, which is overall quite well understood. We have introduced essential relations needed to describe the transport and to extract key parameters of the system. Measurements on an exemplary bilayer graphene device, representative for the devices studied in this work, were presented to guide the discussion. Using a backgate, we demonstrated the facility of changing the charge carrier population in bilayer graphene from holes, via a regime of holes and electrons coexisting in puddles, all the way to electrons. Significant related changes in the transport have been highlighted. We shall come back to them, when revealing effects of lithium intercalation on the charge carrier

density. Besides, two unique signatures of bilayer graphene have been identified in (1) the sequence of plateaus in its quantum Hall conductivity and (2) the line shape of its Raman 2D band.

#### References

- 1. Castro Neto, A.H., Guinea, F., Peres, N.M.R., Novoselov, K.S., Geim, A.K.: The electronic properties of graphene. Rev. Mod. Phys. **81**, 109–162 (2009)
- McCann, E., Koshino, M.: The electronic properties of bilayer graphene. Rep. Prog. Phys. 76, 056503 (2013)
- Koshino, M., Ando, T.: Electronic properties of monolayer and multilayer graphene. In: Aoki, H., Dresselhaus, M.S. (eds.) Physics of Graphene. NanoScience and Technology, pp. 173–212. Springer International Publishing, Cham (2014)
- Mecklenburg, M., Regan, B.C.: Spin and the honeycomb lattice: lessons from graphene. Phys. Rev. Lett. 106. 116803 (2011)
- 5. Song, D., et al.: Unveiling pseudospin and angular momentum in photonic graphene. Nat. Commun. **6**, 6272 (2015)
- Fuchs, N.J., Piéchon, F., Goerbig, O.M., Montambaux, G.: Topological Berry phase and semiclassical quantization of cyclotron orbits for two dimensional electrons in coupled band models. Eur. Phys. J. B 77, 351–362 (2010)
- Park, C.-H., Marzari, N.: Berry phase and pseudospin winding number in bilayer graphene. Phys. Rev. B 84, 205440 (2011)
- 8. Young, A.F., Zhang, Y., Kim, P.: Experimental manifestation of Berry phase in graphene. In: Aoki, H., Dresselhaus, M.S. (eds.) Physics of Graphene. NanoScience and Technology, pp. 3–28. Springer International Publishing, Cham (2014)
- Novoselov, K.S., et al.: Two-dimensional gas of massless Dirac fermions in graphene. Nature 438, 197–200 (2005)
- Zhang, Y., Tan, Y.-W., Stormer, H.L., Kim, P.: Experimental observation of the quantum Hall effect and Berry's phase in graphene. Nature 438, 201–204 (2005)
- 11. de Gail, R., Goerbig, M.O., Montambaux, G.: Magnetic spectrum of trigonally warped bilayer graphene: semiclassical analysis, zero modes, and topological winding numbers. Phys. Rev. B **86**, 045407 (2012)
- 12. Mikitik, G.P., Sharlai, Y.V.: Manifestation of Berry's phase in metal physics. Phys. Rev. Lett. **82**, 2147–2150 (1999)
- Ando, T., Nakanishi, T.: Impurity scattering in carbon nanotubes—absence of back scattering.
   J. Phys. Soc. Jpn. 67, 1704–1713 (1998)
- 14. Katsnelson, M.I., Novoselov, K.S., Geim, A.K.: Chiral tunnelling and the Klein paradox in graphene. Nat. Phys. **2**, 620–625 (2006)
- Young, A.F., Kim, P.: Quantum interference and Klein tunnelling in graphene heterojunctions. Nat. Phys. 5, 222–226 (2009)
- 16. Bernal, J.D.: The structure of graphite. Proc. Roy. Soc. Lond. A **106**, 749–773 (1924)
- 17. Slonczewski, J.C., Weiss, P.R.: Band structure of graphite. Phys. Rev. 109, 272-279 (1958)
- 18. McClure, J.W.: Theory of diamagnetism of graphite. Phys. Rev. 119, 606–613 (1960)
- 19. Kuzmenko, A.B., Crassee, I., van der Marel, D., Blake, P., Novoselov, K.S.: Determination of the gate-tunable band gap and tight-binding parameters in bilayer graphene using infrared spectroscopy. Phys. Rev. B **80**, 165406 (2009)
- 20. Ohta, T., Bostwick, A., Seyller, T., Horn, K., Rotenberg, E.: Controlling the electronic structure of bilayer graphene. Science **313**, 951–954 (2006)
- Malard, L.M., et al.: Probing the electronic structure of bilayer graphene by Raman scattering. Phys. Rev. B 76, 201401 (2007)

References 39

 Zhang, L.M., et al.: Determination of the electronic structure of bilayer graphene from infrared spectroscopy. Phys. Rev. B 78, 235408 (2008)

- Li, Z.Q., et al.: Band structure asymmetry of bilayer graphene revealed by infrared spectroscopy. Phys. Rev. Lett. 102, 037403 (2009)
- Zou, K., Hong, X., Zhu, J.: Effective mass of electrons and holes in bilayer graphene: Electron-hole asymmetry and electron-electron interaction. Phys. Rev. B 84, 085408 (2011)
- 25. Yankowitz, M., et al.: Band structure mapping of bilayer graphene via quasiparticle scattering. APL Mater. 2, 092503 (2014)
- 26. Novoselov, K.S., et al.: Unconventional quantum Hall effect and Berry's phase of  $2\pi$  in bilayer graphene. Nat. Phys. **2**, 177–180 (2006)
- 27. McCann, E., Fal'ko, V.I.: Landau-level degeneracy and quantum Hall effect in a graphite bilayer. Phys. Rev. Lett. **96**, 086805 (2006)
- 28. Varlet, A., et al.: Fabry-Pérot interference in gapped bilayer graphene with broken anti-Klein tunneling. Phys. Rev. Lett. **113**, 116601 (2014)
- 29. Ariel, V., Natan, A.: Electron effective mass in graphene. In: 2013 International Conference on Electromagnetics in Advanced Applications (ICEAA), pp. 696–698 (2013)
- 30. Castro, E.V., et al.: Biased bilayer graphene: semiconductor with a gap tunable by the electric field effect. Phys. Rev. Lett. **99**, 216802 (2007)
- 31. Elias, D.C., et al.: Dirac cones reshaped by interaction effects in suspended graphene. Nat. Phys. **7**, 701–704 (2011)
- 32. Bolotin, K.I., et al.: Ultrahigh electron mobility in suspended graphene. Solid State Commun. **146**, 351–355 (2008)
- 33. Du, X., Skachko, I., Barker, A., Andrei, E.Y.: Approaching ballistic transport in suspended graphene. Nat. Nanotech. 3, 491–495 (2008)
- 34. Orlita, M., Potemski, M.: Dirac electronic states in graphene systems: optical spectroscopy studies. Semicond. Sci. Technol. 25, 063001 (2010)
- 35. Li, G., Andrei, E.Y.: Observation of Landau levels of Dirac fermions in graphite. Nat. Phys. 3, 623–627 (2007)
- Li, G., Luican, A., Andrei, E.Y.: Scanning tunneling spectroscopy of graphene on graphite. Phys. Rev. Lett. 102, 176804 (2009)
- Song, Y.J., et al.: High-resolution tunnelling spectroscopy of a graphene quartet. Nature 467, 185–189 (2010)
- 38. Faugeras, C., et al.: Magneto-Raman scattering of graphene on graphite: electronic and phonon excitations. Phys. Rev. Lett. **107**, 036807 (2011)
- 39. Osburn, C.M., Ormond, D.W.: Dielectric breakdown in silicon dioxide films on silicon: I . Measurement and interpretation. J. Electrochem. Soc. 119, 591–597 (1972)
- 40. Schedin, F., et al.: Detection of individual gas molecules adsorbed on graphene. Nat. Mater. 6, 652–655 (2007)
- 41. Kim, W., et al.: Hysteresis caused by water molecules in carbon nanotube field-effect transistors. Nano Lett. 3, 193–198 (2003)
- 42. Lohmann, T., von Klitzing, K., Smet, J.H.: Four-terminal magneto-transport in graphene p-n junctions created by spatially selective doping. Nano Lett. 9, 1973–1979 (2009)
- 43. Martin, J., et al.: Observation of electron-hole puddles in graphene using a scanning single-electron transistor. Nat. Phys. **4**, 144–148 (2008)
- 44. Zhang, Y., Brar, V.W., Girit, C., Zettl, A., Crommie, M.F.: Origin of spatial charge inhomogeneity in graphene. Nat. Phys. 5, 722–726 (2009)
- 45. Deshpande, A., Bao, W., Miao, F., Lau, C.N., LeRoy, B.J.: Spatially resolved spectroscopy of monolayer graphene on SiO<sub>2</sub>. Phys. Rev. B **79**, 205411 (2009)
- 46. Couto, N.J.G., et al.: Random strain fluctuations as dominant disorder source for high-quality on-substrate graphene devices. Phys. Rev. X 4, 041019 (2014)
- 47. Samaddar, S., Yudhistira, I., Adam, S., Courtois, H., Winkelmann, C.B.: Charge puddles in graphene near the Dirac point. Phys. Rev. Lett. 116, 126804 (2016)
- 48. Rutter, G.M., et al.: Microscopic polarization in bilayer graphene. Nat. Phys. 7, 649–655 (2011)

- Wiedmann, S., et al.: Coexistence of electron and hole transport in graphene. Phys. Rev. B 84, 115314 (2011)
- Hwang, E.H., Das Sarma, S.: Insulating behavior in metallic bilayer graphene: Interplay between density inhomogeneity and temperature. Phys. Rev. B 82, 081409 (2010)
- Zou, K., Zhu, J.: Transport in gapped bilayer graphene: the role of potential fluctuations. Phys. Rev. B 82, 081407 (2010)
- 52. Zhu, W., Perebeinos, V., Freitag, M., Avouris, P.: Carrier scattering, mobilities, and electrostatic potential in monolayer, bilayer, and trilayer graphene. Phys. Rev. B **80**, 235402 (2009)
- Adam, S., Das Sarma, S.: Boltzmann transport and residual conductivity in bilayer graphene. Phys. Rev. B 77, 115436 (2008)
- 54. Chen, J.-H., et al.: Charged-impurity scattering in graphene. Nat. Phys. 4, 377–381 (2008)
- 55. Chen, J.-H., Jang, C., Xiao, S., Ishigami, M., Fuhrer, M.S.: Intrinsic and extrinsic performance limits of graphene devices on SiO<sub>2</sub>. Nat. Nanotech. **3**, 206–209 (2008)
- 56. Ashcroft, N.W., Mermin, N.D.: Solid State Physics. Brooks/Cole (1976)
- ASTM F76-08(2016): Standard test methods for measuring resistivity and Hall coefficient and determining Hall mobility in single-crystal semiconductors. ASTM International, West Conshohocken, USA (2016)
- 58. Vasileva, G.Y., et al.: Linear magnetoresistance in compensated graphene bilayer. Phys. Rev. B **93**, 195430 (2016)
- Alekseev, P.S., et al.: Magnetoresistance in two-component systems. Phys. Rev. Lett. 114, 156601 (2015)
- Klitzing, K.V., Dorda, G., Pepper, M.: New method for high-accuracy determination of the fine-structure constant based on quantized Hall resistance. Phys. Rev. Lett. 45, 494

  –497 (1980)
- 61. Hwang, E.H., Das Sarma, S.: Single-particle relaxation time versus transport scattering time in a two-dimensional graphene layer. Phys. Rev. B 77, 195412 (2008)
- 62. Hong, X., Zou, K., Zhu, J.: Quantum scattering time and its implications on scattering sources in graphene. Phys. Rev. B **80**, 241415 (2009)
- 63. Bao, W., et al.: Magnetoconductance oscillations and evidence for fractional quantum Hall states in suspended bilayer and trilayer graphene. Phys. Rev. Lett. **105**, 246601 (2010)
- Coleridge, P.T.: Small-angle scattering in two-dimensional electron gases. Phys. Rev. B 44, 3793–3801 (1991)
- 65. Engels, S., et al.: Limitations to carrier mobility and phase-coherent transport in bilayer graphene. Phys. Rev. Lett. 113, 126801 (2014)
- Min, H., MacDonald, A.H.: Chiral decomposition in the electronic structure of graphene multilayers. Phys. Rev. B 77, 155416 (2008)
- Kumar, A., et al.: Integer quantum Hall effect in trilayer graphene. Phys. Rev. Lett. 107, 126806 (2011)
- 68. Zhang, L., Zhang, Y., Camacho, J., Khodas, M., Zaliznyak, I.: The experimental observation of quantum Hall effect of *l* = 3 chiral quasiparticles in trilayer graphene. Nat. Phys. **7**, 953–957 (2011)
- 69. Grushina, A.L., et al.: Insulating state in tetralayers reveals an even-odd interaction effect in multilayer graphene. Nat. Commun. 6, 6419 (2015)
- Beenakker, C.W.J., van Houten, H.: Quantum transport in semiconductor nanostructures. In: Ehrenreich, H., Turnbull, D. (eds.) Semiconductor Heterostructures and Nanostructures. Solid State Physics, vol. 44, pp. 1–228. Academic Press, Inc., San Diego (1991)
- 71. Gorbachev, R.V., Tikhonenko, F.V., Mayorov, A.S., Horsell, D.W., Savchenko, A.K.: Weak localization in bilayer graphene. Phys. Rev. Lett. 98, 176805 (2007)
- 72. Kechedzhi, K., Fal'ko, V.I., McCann, E., Altshuler, B.L.: Influence of trigonal warping on interference effects in bilayer graphene. Phys. Rev. Lett. **98**, 176806 (2007)
- Altshuler, B.L., Aronov, A.G.: Electron-electron interaction in disordered conductors. In: Efros, A.L., Pollak, M. (eds.) Electron-Electron Interactions in Disordered Systems. Modern Problems in Condensed Matter Sciences, vol. 10, pp. 1–153. North-Holland Physics Publishing, Elsevier Science Publishers B.V., The Netherlands (1985)

References 41

74. Iwabuchi, S., Nagaoka, Y.: Effect of intersubband impurity scattering on the Anderson localization in two dimensional electron systems. J. Phys. Soc. Jpn. **58**, 1325–1333 (1989)

- 75. Ferrari, A.C., et al.: Raman spectrum of graphene and graphene layers. Phys. Rev. Lett. 97, 187401 (2006)
- Malard, L.M., Pimenta, M.A., Dresselhaus, G., Dresselhaus, M.S.: Raman spectroscopy in graphene. Phys. Rep. 473, 51–87 (2009)
- 77. Ferrari, A.C., Basko, D.M.: Raman spectroscopy as a versatile tool for studying the properties of graphene. Nat. Nanotech. **8**, 235–246 (2013)
- Yan, J.-A., Ruan, W.Y., Chou, M.Y.: Phonon dispersions and vibrational properties of monolayer, bilayer, and trilayer graphene: density-functional perturbation theory. Phys. Rev. B 77, 125401 (2008)
- 79. Herziger, F., et al.: Two-dimensional analysis of the double-resonant 2D Raman mode in bilayer graphene. Phys. Rev. Lett. **113**, 187401 (2014)
- 80. Lazzeri, M., Attaccalite, C., Wirtz, L., Mauri, F.: Impact of the electron-electron correlation on phonon dispersion: failure of LDA and GGA DFT functionals in graphene and graphite. Phys. Rev. B **78**, 081406 (2008)
- 81. Pisana, S., et al.: Breakdown of the adiabatic Born-Oppenheimer approximation in graphene. Nat. Mater. **6**, 198–201 (2007)
- 82. Yan, J., Zhang, Y., Kim, P., Pinczuk, A.: Electric field effect tuning of electron-phonon coupling in graphene. Phys. Rev. Lett. **98**, 166802 (2007)
- 83. Das, A., et al.: Monitoring dopants by Raman scattering in an electrochemically top-gated graphene transistor. Nat. Nanotech. 3, 210–215 (2008)

# Chapter 3 Electrochemical Device Setup and Fabrication



For gate-controlled electrochemical lithiation of bilayer graphene devices, we implement the galvanic cell layout schematically shown in Fig. 3.1: bilayer graphenel electrolytelLi metal. Its working principle will be discussed in Sect. 3.1, aspects of which are relevant to understand decisions made for the actual device design. It will become clear that the choice of the electrolyte is critical as it needs to fulfill a series of requirements, not the least our ability to reliably position it and the need to cover the as-prepared bilayer graphene devices only partially. An introduction to the used polymer electrolyte is therefore given in Sect. 3.2, before we turn to the fabrication of our bilayer graphene structures and the electrochemical cell assembly in Sect. 3.3.

#### 3.1 Electrochemical Lithiation of Graphitic Carbon

The scheme shown in Fig. 3.1 closely resembles the one of a Li-ion battery, in which Li-ions are transferred between two Li insertion compounds via a Li-ion conducting electrolyte, while electrons flow via an external circuit. In Fig. 3.2a, we show a schematic of the Li-ion battery first released by Sony in 1991, which uses a pair of electrodes made of graphite and of LiCoO<sub>2</sub>. The open-circuit voltage  $U_{\rm OCV}$  of the cell is defined by the difference between the chemical potential of Li in the two electrodes: [1]

$$U_{\text{OCV}} = \frac{\mu_{\text{Li,c}} - \mu_{\text{Li,a}}}{F},\tag{3.1}$$

where F is the Faraday constant and  $\mu_{\text{Li,c}}$  ( $\mu_{\text{Li,a}}$ ) is the chemical potential of the cathode (anode), respectively. As both  $\mu_{\text{Li,c}}$  and  $\mu_{\text{Li,a}}$  vary during charge/discharge

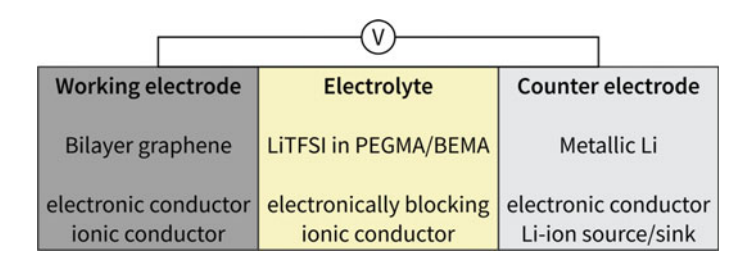


Fig. 3.1 Schematic galvanic cell layout used in this work

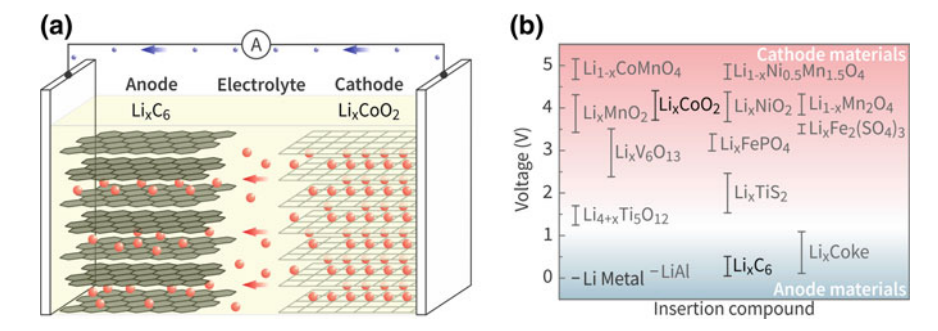


Fig. 3.2 a Schematic Li-ion battery during charging. Electrons flow from the cathode to the anode via an external circuit. Simultaneously, Li-ions (red balls) leaving the cathode move across the electrolyte and are inserted into the anode. The cathode and the anode are primarily made of Li insertion compounds, here  $Li_{1-x}CoO_2$  and  $Li_xC_6$ , respectively. **b** Electrochemical potential ranges of some Li insertion compounds referenced to metallic Li. Panel b adapted with permission of Springer US, from Ref. [1]; permission conveyed through Copyright Clearance Center, Inc

of the battery, <sup>1</sup> Li metal may be used as a reference electrode featuring an invariant chemical potential which we denote as  $\mu_{\text{Li}}^{\text{ref}}$ . In Fig. 3.2b we replot the electrochemical potential ranges of some Li insertion compounds referenced to metallic Li from Ref. [1], in order to illustrate the high (low) electrode potential versus Li qualifying materials such as LiCoO<sub>2</sub> (Li-graphite, stated as Li<sub>x</sub>C<sub>6</sub>) for the cathode (anode) in Li-ion batteries. As we are interested in the graphitic electrode only, we employ the scheme shown in Fig. 3.1, using Li metal as a Li-ion sink/source as well as a reference electrode, rather than using a practical cathode material. We therefore denote our graphitic anode as the working electrode and Li metal as the counter electrode, following conventions in electroanalytical methods.

When the graphitic electrode is electrochemically reduced, Li-ions penetrate into the host crystal structure forming  $\text{Li}_x\text{C}_6$  according to [2]

<sup>&</sup>lt;sup>1</sup>The chemical potential of Li in, e.g., the cathode  $\mu_{\mathrm{Li},c} = \mu_{\mathrm{Li},c}^{\circ} + RT \ln a_c$  contains a standard value at standard conditions  $\mu_{\mathrm{Li},c}^{\circ}$  and an activity ( $a_c$ ) dependent term. The activity depends on the state of charge of the battery.

$$\text{Li}_{x}\text{C}_{6} \rightleftharpoons \text{charge} \times \text{xLi}^{+} + \text{xe}^{-} + \text{C}_{6},$$
 (3.2)

which essentially describes a host/guest solid state redox reaction: the guest ions are taken up within the interlayer gaps of the graphite host, also called galleries. This so-called intercalation of Li-ions may happen via open edges, grain boundaries or certain defect sites [3], but not via the impermeable graphene basal planes, [4] as indicated in the top of Fig. 3.3b. At ambient conditions, a maximum stoichiometry of LiC<sub>6</sub> can be reached, i.e., one Li atom per six carbon atoms.<sup>2</sup> The whole process can be reversed, i.e., during the electrochemical oxidation of Li<sub>x</sub>C<sub>6</sub> lithium de-intercalates. With varying Li content  $0 \le x \le 1$ , both the crystal structure as well as the electronic properties of Li<sub>x</sub>C<sub>6</sub> undergo changes, as will be discussed in Sect. 3.1.1. In Sect. 3.1.2 we briefly shed some light on processes taking place at the interface between a Li (rich) electrode and the electrolyte.

#### 3.1.1 The $Li_xC_6$ System

Crystallographic changes are induced by intercalating Li into bulk graphite, as several phases of varying degree of intercalant ordering (both in-plane and in c-axis direction) may be realized, see Fig. 3.3. While in bulk graphite adjacent carbon planes are commonly AB-stacked, [6] in LiC<sub>6</sub> the most fundamental vertical arrangement of graphene layers (capital letters) and Li-intercalant layers (small greek letters) is  $A\alpha A\alpha A\alpha \dots$  I.e., adjacent graphene layers readjust to accommodate for the high ordering of Li-ions showing an in-plane  $(\sqrt{3} \times \sqrt{3})R30^{\circ}$  superstructure, [7] see Fig. 3.3a. Furthermore, the van der Waals gap between the layers is widened by  $\sim 10\%$  from  $c \approx 3.35$ Å in AB-stacked graphite to  $c \approx 3.70$ Å in LiC<sub>6</sub>, and the in-plane bonds are dilated by  $\sim$ 1%. Upon lowering the Li content x, transitions between different phases occur as can be inferred from the phase diagram shown in Fig. 3.3b. The out-of-plane ordering in bulk samples is determined by the so-called staging phenomenon: a regular sequence in c-axis direction of empty and occupied galleries, schematically illustrated in Fig. 3.3a. It is commonly characterized by the stage index s, which is equal to the number of graphene layers between adjacent occupied galleries. Since staging is naturally absent in bilayer graphene, we will just note that it is believed to be a thermodynamic effect related to the energy required to open the van der Waals gap in order to accommodate the intercalant. The repulsive Coulomb interaction between Li-ions, responsible for different in-plane orders, is found to be less important, leading to a few highly occupied galleries being energetically favorable compared to a random distribution of Li in the bulk [2]. Expectedly, in-plane ordered phases prevail at lowest temperatures, while in-plane disordered (liquid, L) phases are favored at higher temperatures.

Mixed-phase regions are known to make up for most of the reversible charging capacity in  $\text{Li}_x\text{C}_6$  near room temperature. In fact, these regions show up as plateaus in the galvanostatic (constant current) charge and discharge curves of a graphitic electrode. As an illustrative example we show the first 1 1/2 galvanostatic

<sup>&</sup>lt;sup>2</sup>A higher Li density up to LiC<sub>2</sub> may be achieved in high-pressure conditions [5].

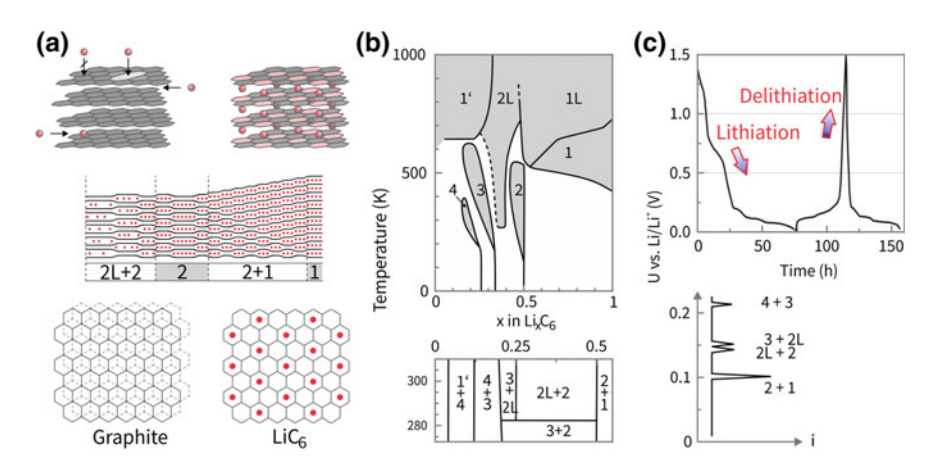


**Fig. 3.3** The Li<sub>x</sub>C<sub>6</sub> system. **a** Schematic of partially intercalated Li<sub>x</sub>C<sub>6</sub> showing stage 1 and 2 regions (center). AB-stacked graphite and  $A\alpha A\alpha$ -stacked LiC<sub>6</sub> are shown below (top view) and above. **b** Phase diagram where single-phase regions (grey shaded areas and black lines) and mixed-phase regions (white areas) are identified with the stage index (number). L indicates a disordered (liquid) phase and 1' is the dilute stage-1 phase. **c** First 1 1/2 galvanostatic discharge/charge cycles of a graphitel1 M LiAsF<sub>6</sub>/PC/EClLi cell. Mixed-phase regions appear as plateaus at low potential versus Li/Li<sup>+</sup>. A schematic voltammetric curve shown below. Top panels in b and c adapted with permission of Springer-Verlag, from Ref. [8], and with permission of the Electrochemical Society, from Ref. [10], respectively. Permission conveyed through Copyright Clearence Center, Inc. Bottom panel in b adapted with permission from Ref. [9]. Copyright 1991 by the American Physical Society. Bottom panel in c adapted with permission of Wiley-VCH, from Ref. [2]. Copyright 2011 Wiley-VCH Verlag & Co. KGaA, Boschstr. 12, 69469 Weinheim, Germany

charge/discharge cycles of a graphitel1 M LiAsF<sub>6</sub>/PC/ECILi cell measured by Fong et al. [10] in Fig. 3.3c, with the aforementioned plateaus readily visible at low potential versus Li/Li<sup>+</sup>. Likewise, in a voltammetric curve (lower panel in Fig. 3.3c) the respective two-phase regions would show up as pronounced spikes in the current. In the case of bilayer graphene, which can be intercalated up to C<sub>6</sub>LiC<sub>6</sub>, [11] phase transitions due to staging would be absent. However, we may infer that the chemical potential  $\mu_{\text{Li}}^{C_6\text{Li}_xC_6}$  of Li in C<sub>6</sub>Li<sub>x</sub>C<sub>6</sub> for  $x \to 1$  is only  $\mu_{\text{Li}}^{C_6\text{Li}_xC_6}(x \to 1) \approx 0.15\text{V}$  vs. Li/Li<sup>+</sup>, i.e., very close to the one of Li in Li metal. At >1.5V versus Li/Li<sup>+</sup>, bilayer graphene would tend to be completely delithiated as  $x \to 0$ . Hence, we expect Li to intercalate into (deintercalate from) bilayer graphene at a low (high) potential versus Li/Li<sup>+</sup>, respectively.

The intercalation of a single Li-ion is accompanied by the charge transfer on the order of 1 e (where e is the elementary charge) to the electronic states of the graphitic host, leaving the Li 2s level unoccupied [5]. This valence charge acts to screen the intercalant ion and is thus rather locally distributed [12, 13]. There are contradictory reports concerning the extent of charge transfer in bulk Li<sub>x</sub>C<sub>6</sub>, [7, 12, 13] which is possibly dependent on the intercalant concentration. In the case of C<sub>6</sub>Li<sub>x</sub>C<sub>6</sub>, recent ab initio calculations favor a more complete, Li density-independent charge transfer on the order of  $\sim$ 0.88e per Li atom, [14, 15] supported by experimental evidence for the full ionization of intercalated Li in C<sub>6</sub>LiC<sub>6</sub> [11]. Assuming a complete charge transfer, the induced electron density in C<sub>6</sub>LiC<sub>6</sub> should amount to  $n \approx 6.36 \cdot 10^{14} \text{cm}^{-2}$ , which

agrees with a reported calculation of  $6.1 \cdot 10^{14}$ ]cm<sup>-2</sup> [16]. It will be demonstrated in Chap. 4, that we can indeed measure these changes in our bilayer graphene devices.

#### 3.1.2 The Solid Electrolyte Interphase

Even though the reversible intercalation of Li into the graphitic carbon electrode is our major interest, the employed electrochemical working scheme entails an aspect that needs to be mentioned. It is related to the interface between alkali-metal (rich) electrodes and a polymer electrolyte, a subject that has been addressed in detail by Peled et al. [17]. According to this reference, it is a well established fact that both electrodes in question, i.e., Li metal as well as  $\text{Li}_x \text{C}_6$ , are covered by the so-called solid-electrolyte interphase (SEI). This SEI is widely considered crucial for the overall device performance, however both its formation reactions and properties are in general not well understood. In the ideal case, the SEI is a thin protective layer which is Li-ion conducting and electronically blocking, the latter being inferred from the insight that SEI formation terminates once it reaches a critical thickness in excess of the electron tunneling length or the characteristic length for dielectric breakdown.

On Li metal, the SEI is believed to be formed almost instantaneously upon contact with the electrolyte, its thickness, morphology and composition depending on the precise nature of the latter. The SEI, resulting from competing reactions with different components and impurities in the electrolyte, tends to contain both inorganic material such as LiF, Li2O or LiOH as well as organic material such as  $Li_2CO_3$  or polymer [17].

A graphitic electrode (such as bilayer graphene) is commonly mounted into an electrochemical cell in the discharged state and thus shows no reactivity at first. In this case, the SEI mostly forms during the first charge cycle. This commonly shows up as an increased charge capacity during the first lithiation compared to the first delithiation. This irreversible capacity loss can be revealed, e.g., by the galvanostatic charge/discharge of an as-assembled cell, see Fig. 3.3c. Here, the first charge process shows a behavior noticeably different from the second one, especially at  $\sim 0.5-1 \mathrm{V}$  versus Li/Li<sup>+</sup>. This is the typical range for SEI formation, although it continues down to 0 V versus Li/Li<sup>+</sup>. Its chemical composition is expected to be rather similar to the one on Li metal, possible differences arising from the different chemical compositions and morphologies of the carbon surfaces [17].

It should be noted that the SEI formation may continue (albeit at a lower rate) during continuous cycling. Furthermore, morphological changes of the electrode surface during operation involving stripping or deposition of Li but also local heating, rendering the SEI electronically conducting, may cause a continuous consumption of the electrolyte in order to restore the SEI [17, 18]. The specific nature of the later, as already mentioned, depends critically on the choice of the electrolyte. Some of the most understood, known to form stable SEIs with Li, are non-aqueous liquid electrolytes with ethylene carbonate-based solvents. Nonetheless, in this work we employ a solid polymer electrolyte, which will be introduced in the next section.

#### 3.2 Solid Polymer Electrolyte

Although less understood than certain non-aqueous liquid electrolytes, especially with respect to its ability of forming a stable SEI with Li, this work rests on using a polymer electrolyte. The major reason for this choice lies in the possibility to integrate a polymer electrolyte into a device by position-controlled drop-casting onto the semiconductor substrate followed by radiation crosslinking. The resulting solid amorphous polymer matrix features both ionic conductivity and mechanical stability, a crucial advantage (for this work) over liquid electrolytes.

According to Gray and Armand [19], a polymer electrolyte is a system comprising a salt dissolved in a high-molecular-weight polar polymer matrix. The Li-salt we use is LiTFSI, see Fig. 3.4d, which consists of a Li<sup>+</sup> cation and a large bis(trifluoromethane)sulfonimide (TFSI) anion, proven particularly successful in its use with polymer electrolytes [19]. As for the polymer matrix, we adopt a recipe proposed by Nair et al. [20] relying on mixing of a dimethacrylic oligomer, i.e., bisphenol A ethoxylate dimethacrylate (BEMA, Fig. 3.4a, average  $M_n = 1700$ ), and a mono methacrylate based reactive diluent, i.e., poly(ethylene glycol) monomethyl ether monomethacrylate (PEGMA, Fig. 3.4b, average  $M_n = 500$ ), with a radical photo-initiator, i.e., 2-hydroxy-2-methylpropiophenone (Da-rocur 1173, Fig. 3.4c). Here, BEMA reportedly readily forms flexible 3D networks with its long poly-ethoxy chains ensuring a high diffusivity of Li-ions inside the polymer matrix [21]. The addition of PEGMA allows to tune the viscosity of the mixture as well as the cross-linking density in the final network, with the pendant ethoxy groups further enhancing the ionic conductivity [20]. During UV exposure (see Fig. 3.5a for details), the initiator decomposes into free radicals which react with PEGMA/BEMA to form the polymer matrix, rendering the material overall soft but solid, with a glass transition temperature below 250 K.

As discussed in Sect. 3.2.1, we identified 0.35 M LiTFSI in PEGMA/BEMA w/w 3:7 with 2–4 wt% photoinitiator as a suitable electrolyte for our experiments, featuring the highest ionic conductivity, a good homogeneity and at the same time a manageable viscosity needed for precise positioning on our  $4 \times 4$  mm<sup>2</sup> Si/SiO<sub>2</sub>

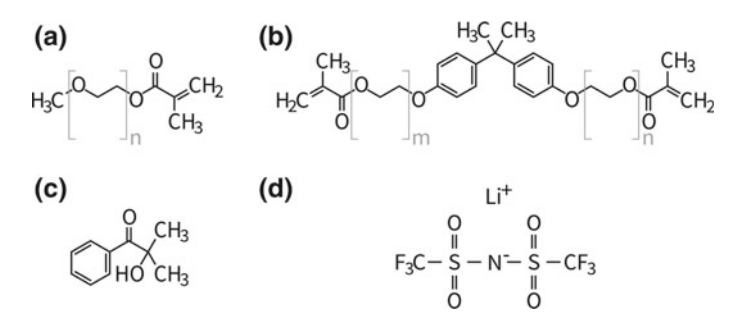
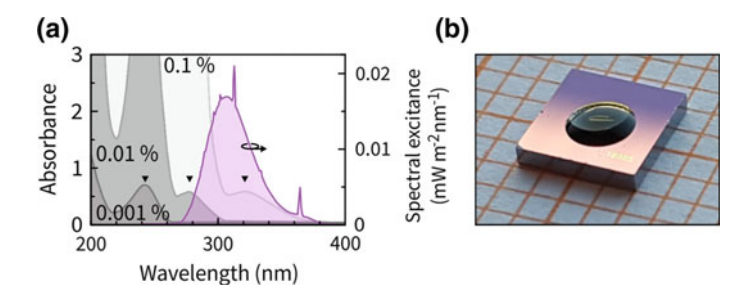


Fig. 3.4 Representations of chemical substances constituting the polymer electrolyte. a PEGMA, b BEMA, c Darocur 1173, and d LiTFSI



**Fig. 3.5** a Absorbance of the photoinitiator Darocur 1173 for different concentrations in acetonitrile (grey shaded graphs), showing three absorption peaks (black triangles). Spectral excitance of the UVB lamp used for radiation crosslinking with a peak near 312 nm (violet graph). **b** Photograph of a drop-casted solid polymer electrolyte on a  $4 \times 4$  mm<sup>2</sup> Si/SiO<sub>2</sub> substrate

substrates. An identical electrolyte was successfully used for electrolyte gating of few-layer graphene samples [22]. Once positioned and solidified, the electrolyte remains exempt from creep or wandering and endures temperature sweeps down to 1.5 K while keeping its room-temperature properties. A photograph of a drop-casted 0.35 M LiTFSI in PEGMA/BEMA w/w 3:7 with 2–4 wt% photoinitiator after UV-curing is shown in Fig. 3.5b.

#### 3.2.1 Characterization of the Solid Polymer Electrolyte

We measured the ionic conductivity of PEGMA/BEMA based solid polymer electrolytes prepared with different w/w ratios and different content of LiTFSI upon UV curing by impedance spectroscopy in a self-made conductivity cell with stainless steel electrodes, for the 1–105 Hz range at ambient temperature. The resulting impedance spectra shown in Fig. 3.6 correspond to the bulk resistance of the polymer electrolytes. They yield ionic conductivities ranging from  $\sigma = 2.8 \cdot 10^{-6}$  S/cm (samples 3 and 4) to  $\sigma = 2.1 \cdot 10^{-5}$  S/cm (sample 7). The higher ionic conductivity observed for the PEGMA/BEMA electrolytes with higher PEGMA content (samples 7 & 8) agrees very well with results reported from Nair et al. [20]. However, the overall viscosity decreases with increasing PEGMA content and renders the handling of individual drops rather difficult. 70 % PEGMA was reported as the maximum percentage yielding a mechanically stable film [20]. However, we obtain a suitable viscosity at a PEGMA/BEMA w/w ratio of 3:7, a mixture in which  $\sim$ 10 wt% of LiTFSI shows best ionic conductivity with complete dissolution of the salt (in sample 6, LiTFSI did not dissolve completely).

According to the observed homogeneity and mechanical properties of the prepared materials, sample 5 ( $\sim$ 0.35 M LiTFSI in PEGMA/BEMA w/w 3:7 with 2–4 wt% photoinitiator) with  $\sigma = 7.9 \cdot 10^{-6}$  S/cm was chosen as a suitable electrolyte for gate-controlled intercalation of our bilayer graphene devices.

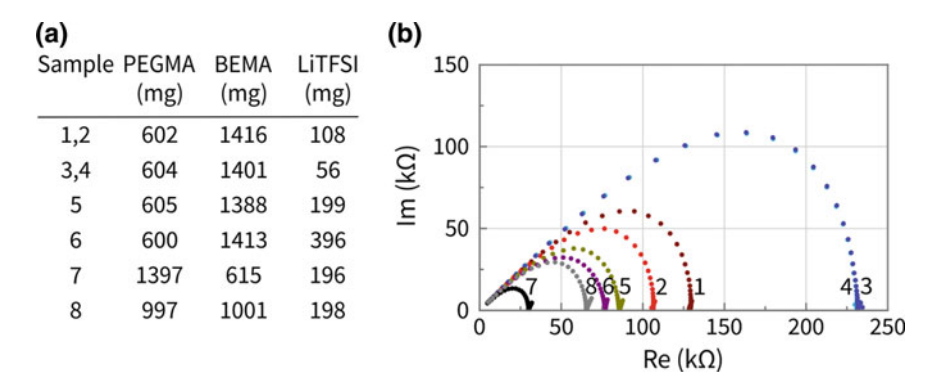


**Fig. 3.6** Characterization of eight different LiTFSI in PEGMA/BEMA solidified polymer electrolyte samples with 2–4 wt% photoinitiator at ambient temperature. **a** The composition of the studied samples. **b** Impedance spectra of all samples

Besides ionic conductivity, the most important parameters for the Li polymer electrolyte performance in a metallic Li cell besides ionic conductivity are Li transference number [23] and interfacial stability. The Li transference number was measured by galvanostatic polarization in a self-made LilelectrolytelLi cell similarly as in Ref. [24] (Fig. 3.7). Upon applying a constant current I, the time dependent voltage change was recorded until the steady state was reached (Fig. 3.7a). When the electrolyte does not react with Li, i.e., the electrolyte resistance  $R_{\rm el}$  remains constant, the Li transference number is determined from  $t_+^{\rm pol} = \frac{IR_{\rm tot,0} - IR_{\rm SEI,0}}{U_\infty - IR_{\rm SEI,0}}$ , where  $U_\infty$  is the steady state voltage.  $R_{\rm SEI,0}$  and  $R_{\rm SEI,\infty}$  are resistances of the solid electrolyte interphase (SEI) before and after the polarization. The first semicircle before and after polarization in Fig. 3.7b indicate a change to the electrolyte conductivity itself, which has to be taken into account ( $\Delta R_{\rm el} = R_{\rm el,\infty} - R_{\rm el,0}$ ). Hence, the transference number becomes  $t_+^{\rm pol} = \frac{IR_{\rm tot,0} - IR_{\rm SEI,0}}{U_\infty - I(R_{\rm SEI,\infty} + \Delta R_{\rm el})} = 0.40$ . This Li-ion transference number being < 0.5 can be expected for the given class of electrolyte material. Its finite value clearly demonstrates that the polymer electrolyte shows Li-ion conductivity.

From Fig. 3.7b we can conclude that the reaction of 0.35 M LiTFSI in PEGMA/BEMA w/w 3:7 with 2–4 wt% photoinitiator electrolyte with Li both on the interface (SEI, second semicircle) and in the bulk (first semicircle) is not completed even after a 3 days aging process. While the SEI is observed to slightly grow with time, it is the bulk of the electrolyte which shows a more severe decrease in ionic conductivity. We attribute this behavior to the instability of the polymer electrolyte with respect to Li. 0.35 M LiTFSI in PEGMA/BEMA w/w 3:7 with 2–4 wt% photoinitiator nonetheless proves a functional Li-ion conducting electrolyte whose mechanical properties make it particularly suitable for our Li-intercalation experiments.

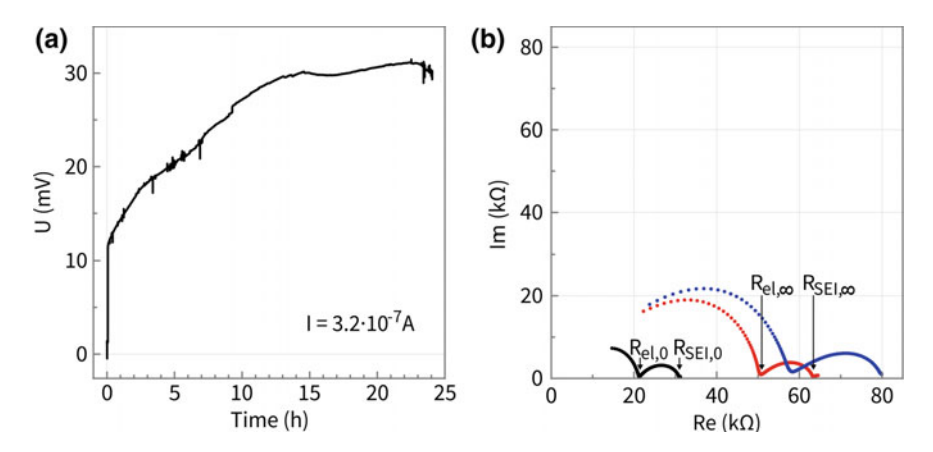


**Fig. 3.7** a Galvanostatic polarization of 0.35 M LiTFSI in PEGMA/BEMA w/w 3:7 with 2-4 wt% photoinitiator. **b** Impedance spectra before polarization (black), after polarization (red), and 3 days after polarization (blue). All measurements are performed in a LilelectrolytelLi cell at ambient temperature

#### 3.2.2 Electrolyte Positioning

The suboptimal properties of our polymer electrolyte just discussed become all acceptable in the light of its positioning capability. The main interest lies in determining the position of the electrolyte's edge (or at least of a section of it), as we aim at being able to have it cover a bilayer graphene device (of characteristic length of  $\sim$ 50 $\mu$ m) only partially. This can be accomplished by engineering the surface wettability of the employed substrate, which in our case is Si covered by a thermally grown layer of SiO<sub>2</sub>. The idea is to achieve a contrast in contact angle between two different regions on the surface, the border between which will act as a guide to the edge of the electrolyte drop. As the used polymer electrolyte shows a contact angle of about  $\theta = 37^{\circ}$  on our Si/SiO<sub>2</sub> substrates,<sup>3</sup> one may obtain the desired result by either increasing or lowering the contact angle on part of the substrate's surface. We pursued both approaches, either depositing a thin layer of gold (by evaporation) or depositing a self-assembled monolayer of silane, respectively, see Fig. 3.8. Patterns on the surface were realized using a standard lift-off technique, with PMMA masks defined prior to deposition by electron beam lithography. Although silanization turned out to yield more reliable results, both approaches were used during the course of this work.

In Fig. 3.8c, we demonstrate that the lower contact angle of the electrolyte on Au (measured to be  $\theta=20^{\circ}$ ) can be exploited to control the position of the electrolyte's edge. As expected, the electrolyte is observed to readily cover the Au layer up to its border with SiO<sub>2</sub>. Note that deliberately designed rectangular gaps in the Au layer

<sup>&</sup>lt;sup>3</sup>Measured after rinsing the substrate in acetone and isopropanol, without any additional cleaning or surface activation steps.

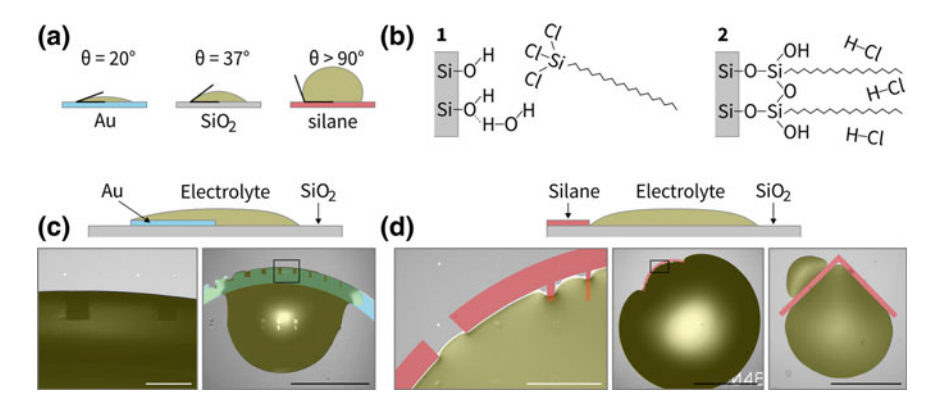


Fig. 3.8 a Schematic contact angle of 0.35 M LiTFSI in PEGMA/BEMA w/w 3:7 with 2–4 wt% photoinitiator on Au (blue), SiO<sub>2</sub> (grey), and silane (red). Values for Au and SiO<sub>2</sub> are measured, while no wetting is observed on silane. b Illustration of the chemisorption of noctadecyltrichlorosilane on SiO<sub>2</sub> under release of HCl, according to Ref. [25]. c,d Optical micrographs illustrating the positioning of the polymer electrolyte (yellow shaded area) by engineering of the surface wettability exploiting the contact angle contrast between SiO<sub>2</sub> and c Au or d silane. For clarity the Au-structure in the lower left panel in c is not shaded. Scale bars are  $100\mu$  m (white) and 1 mm (black). Micrographs with white scale bars are taken at larger magnification in the rectangular regions highlighted in the neighboring micrograph

get nonetheless filled with the electrolyte, as the surface tension of the latter tends to favor a rather smooth edge line. These areas are potentially interesting for our device design, with bilayer graphene positioned partially inside and extruding into the uncovered part. An upper limit for the width of a gap in the Au structure exists to still reliably fill the electrolyte across the gap. It is found to be on the order of  $50\mu m$ , a feasible order of magnitude for device design.

In principle the aforementioned technique also works with other metals. Its biggest drawback, however, lies in the small contrast in contact angle, which we further found to be easily decreased when different surface preparation methods are employed. For example and without going into details,  $O_2$  plasma etching, forming gas annealing or dipping in hydrofluoric acid (HF) all tend to result in a lower and more comparable contact angle on both  $SiO_2$  and the metal film (tested for Au, AuPd (60/40), Pt, Pd, and Ag).

As the usage of  $SiO_2$ -terminated Si substrates is well established and convenient for the present work (and therefore not negotiable), we implement the partial silanization of the  $SiO_2$  surface as an approach to locally increase the contact angle. A self-assembled layer of silane is formed through deposition from the gas phase by over-night heating the substrate and a few drops of n-octadecyltrichlorosilane (OTS) inside an oven at  $T \sim 170^{\circ}$ C [25]. During this procedure, OTS attaches to OH-groups on the substrate by forming covalent bonds under production of HCl gas, illustrated in Fig. 3.8b. As can be seen in Fig. 3.8d, the electrolyte clearly avoids wetting silane-covered regions. Again, gaps in the silane pattern on the order of

 $\sim$ 50 $\mu$ m can be deliberately designed, along which the electrolyte's edge will align rather than penetrate due to the surface tension of the drop. It is feasible to design bilayer devices within such an area as is discussed in the following section.

# 3.3 Bilayer Graphene Device Fabrication and Cell Assembly

The successive steps involved in the fabrication of our bilayer graphene devices are summarized in Fig. 3.9. Device fabrication proceeds as follows.

Figure 3.9a Bilayer graphene flakes are obtained by mechanical exfoliation from bulk graphite (NGS Naturgraphit GmbH) using adhesive tape [26]. At the time of this writing, this presents the most reliable approach to obtain large, AB-stacked single-crystals of high quality. We use a dry transfer technique in order to position and orient the flake on the target SiO<sub>2</sub>-terminated Si substrate [27]. The dry transfer involves the last exfoliation step to be done on a poly(methyl methacrylate) (PMMA) layer, spin-coated on top of a water-soluble sacrificial layer (in our case polyvinyl alcohol, PVA), in turn spin-coated on top of an intermediate Si substrate. We find the hydrophobic PMMA film to facilitate the exfoliation of larger flakes compared to a direct exfoliation onto SiO<sub>2</sub>. Bilayer graphene flakes with typically at least one lateral dimension exceeding 50 \( \mu \) m are selected based on the optical contrast. We verify the bilayer nature by Raman spectroscopy, in particular through the characteristic fourcomponent line-shape of the Raman 2D band, [28] see Sect. 2.8. We then release the PMMA from the intermediate substrate by dissolving the interjacent water-soluble layer in a water bath. A plastic frame glued onto the PMMA facilitates its floating on the water surface during release and its removal from the bath without bilayer graphene getting immersed. Using a home-built alignment setup, the bilayer graphene flake may be positioned onto a target substrate by lowering the supporting PMMA face-down onto the latter until contact. This step is done at above 100°C to avoid trapping water in between bilayer graphene and the substrate. Throughout this work we use  $4 \times 4 \text{ mm}^2$  Si substrates terminated with 300 nm-thick, thermally grown SiO<sub>2</sub>. In case the target substrate underwent processing steps involving resists (e.g., for deposition of metallic markers used for lithography alignment procedures), a fresh SiO<sub>2</sub> surface was prepared by immersion in a buffered HF solution followed by a deionized water rinse [29] prior to the bilayer graphene transfer.

Figure 3.9b We pattern bilayer graphene devices employing either low-pressure  $O_2$ -plasma etching or  $O_2$ :Ar (1:10) reactive ion etching using PMMA masks designed by electron beam (e-beam) lithography. In view of charge carrier transport experiments, we typically etch bilayer graphene into Hall bar shapes (not shown here) [30]. One may use the PMMA from the dry transfer directly for this patterning step. At the end, the remaining resist may be removed using conventional solvents: n-ethylpyrrolidone, acetone, and isopropyl alcohol.

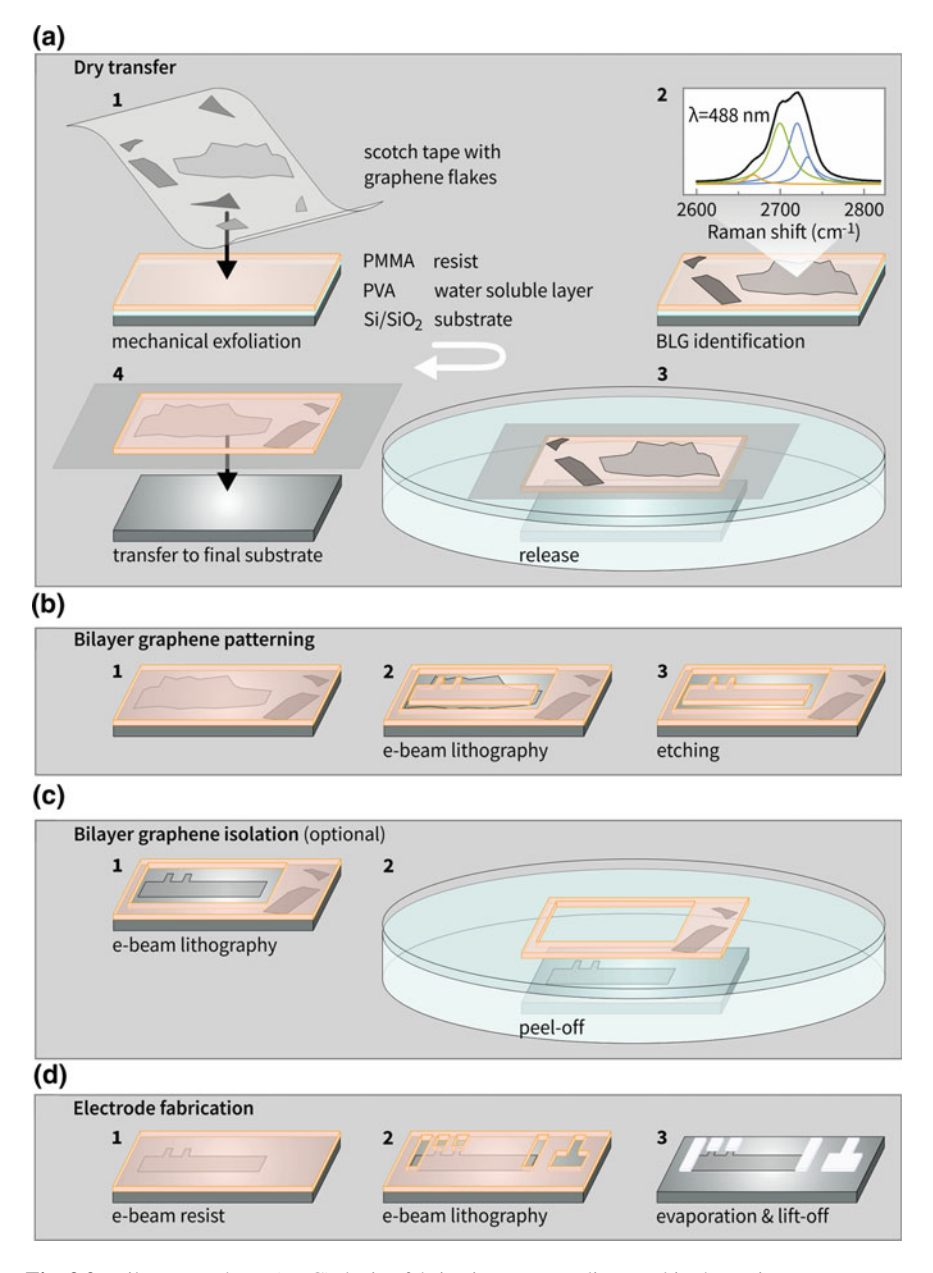


Fig. 3.9 Bilayer graphene (BLG) device fabrication steps as discussed in the main text

Figure 3.9c When necessary, we isolate bilayer graphene on the substrate by removing all other transferred but unwanted graphitic flakes. We do this by opening a hole in the PMMA layer used for etching, such that bilayer graphene is uncovered

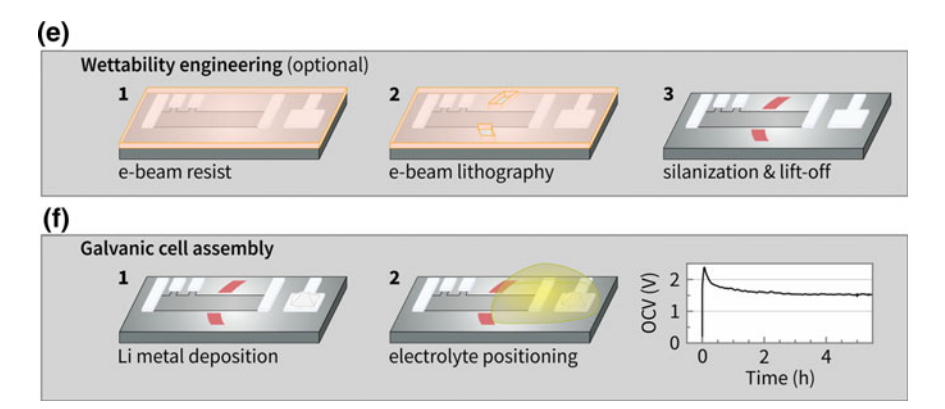


Fig. 3.9 (continued)

from PMMA. When immersing the sample in deionized water, the PMMA attached to the other flakes may be peeled off, [31] leaving only the desired bilayer behind.

Figure 3.9d For the fabrication of electrodes we again use standard electron beam lithography methods. To facilitate the lift-off after metal evaporation, a bilayer PMMA mask is employed to obtain an undercut resist profile. The electrical contacts to the bilayer and the counter-electrode contact for the galvanic cell can be prepared in the same step. While at the beginning of this work devices were made with Ti (5 nm)/Au (55 nm) contacts, early on we switched to all Ti (60 nm). The reason lies in the very different alloying capability of Au and Ti with Li. According to the phase diagrams in Fig. 3.10a, Au is readily lithiated showing a number of different phases at varying Li content [32]. Ti, however, shows no intermetallic formation with Li as well as a negligible Li solubility [33].

This difference can be revealed in lithiation/delithiation experiments performed on lithographically structured Au or Ti electrodes, in a Au (or Ti)|1 M LiTFSI in ethylene carbonate (EC)|Li cell. In Fig. 3.10b, we show the first two cycles with lithiation (delithiation) performed in a sequence of a galvanostatic step down to 50 mV versus Li/Li<sup>+</sup> (up to 2 V vs. Li/Li<sup>+</sup>), followed by a potentiostatic step at 50 mV versus Li/Li<sup>+</sup> (2 V vs. Li/Li<sup>+</sup>) to allow for equilibration of the system. The galvanostatic polarization was done at 20 nA in the case of Au (left), and at 5 nA in the case of Ti (right). While both traces feature a qualitatively similar behavior around 0.5–1 V versus Li/Li<sup>+</sup> indicative of SEI formation processes, [17] see Sect. 3.1.2, extended plateaus in the low-voltage range are observed only in the case of Au. Very similar results have been reported from galvanostatic cycling experiments on metal thin films alloying and not alloying with Li in Ref. [34].

Figure 3.9e If required, we engineer the surface wettability properties according to the discussion in Sect. 3.2.2 in order to facilitate positioning of the electrolyte drop. This again requires electron beam lithography, in order to define the areas where we locally modify the contact angle, for example by silanization. We tend to skip this step if the electrolyte can be placed by hand.

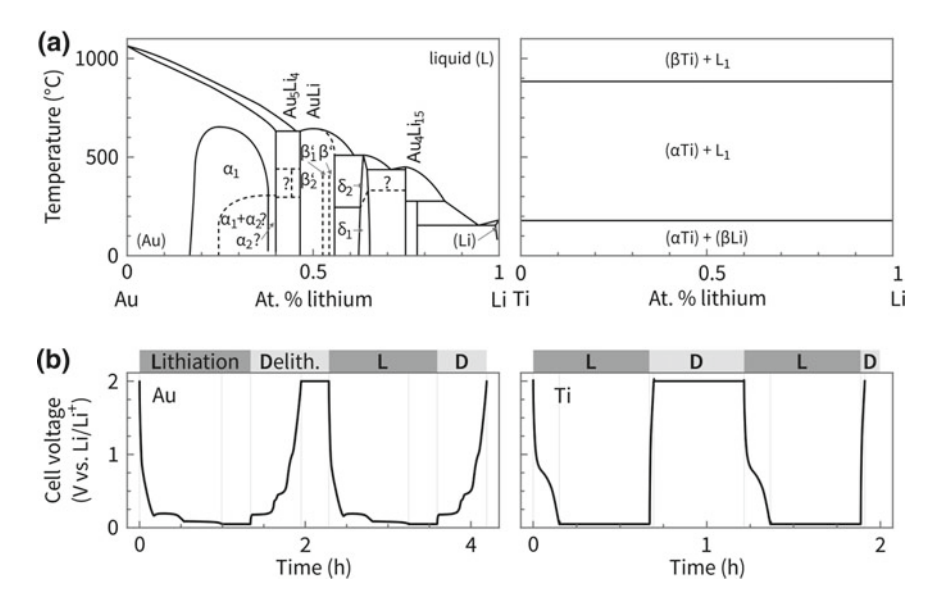


**Fig. 3.10** a Phase diagrams of the Li-Au and the Li-Ti system, respectively. **b** Two consecutive lithiation (L)/delithiation (D) cycles of lithographically designed Au electrodes (left) and Ti electrodes (right), measured in a microscopic Au (Ti)|1 M LiTFSI in ethylene carbonate (EC)|Li cell. Adapted by permission from Springer Nature: panel a from Ref. [32], copyright 1986, and panel b from Ref [33], copyright 1989

Figure 3.9f at this stage we may investigate the properties of bilayer graphene prior to any contact with lithium. To do so, samples should first be annealed (at best over night) in high-vacuum  $p \le 10^{-6}$  mbar at  $T > 100^{\circ}$  C (typically  $T \approx 120^{\circ}$  C). This proves successful in reducing the amount of adsorbates on bilayer graphene, which are typically found to shift the charge neutrality point away from zero backgate voltage (discussion in Sect. 2.5) and inflict additional hysteresis to backgate dependent transport measurements [35].

The fabrication of the electrochemical cell then proceeds in an Ar-filled glovebox. Here, bilayer graphene serves as one electrode (working electrode) of the cell. A Li counter electrode is realized by depositing metallic Li on the designated Ti contact pad. We then position a drop of the polymer electrolyte (0.35 M LiTFSI in PEGMA/BEMA w/w 3:7 with 2–4 wt% photoinitiator) on the device such that both electrodes are connected, leaving most of the bilayer graphene device however uncovered from the drop. While doing so, we monitor the open circuit voltage (OCV) between the working electrode and the counter electrode in situ, which we find to immediately rise to 1.5–2.5 V in all fabricated devices as soon as both electrodes are in contact with the electrolyte. Eventually, the latter is solidified by UV curing. Two scanning electron micrographs of fabricated devices are shown in Fig. 3.11.

3.4 Summary 57

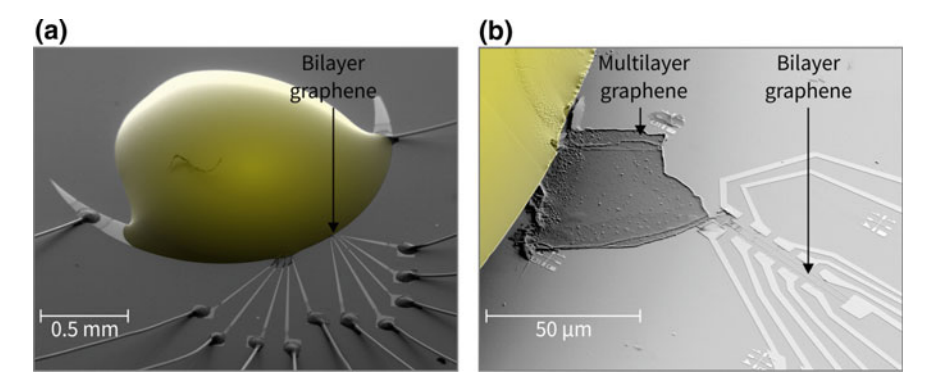


**Fig. 3.11** Scanning electron micrographs of two bilayer graphene devices with UV-cured polymer electrolyte. In **a** the edge of the electrolyte was positioned according to the procedure described in Sect. 3.2.2. In **b** bilayer graphene is naturally attached to a thick multilayer graphene flake which is put in contact with the electrolyte

#### 3.4 Summary

We implement a microscopic galvanic cell setup in which bilayer graphene figures as the working electrode. For the electrochemical lithiation, we may control bilayer graphene's potential with respect to a metallic Li counter electrode across a Li-ion conducting polymer electrolyte. Intercalation of Li-ions is to be expected at low potentials versus Li/Li<sup>+</sup>, the phenomenology of which we have highlighted with special regard to its bulk Li<sub>x</sub>C<sub>6</sub> parent system. While the electrolyte proves crucial in battery applications to guarantee stable SEI formation and thereby potentially long cycling life, we compromise with the choice of our electrolyte. We use 0.35 M LiTFSI in PEGMA/BEMA w/w 3:7 with 2–4 wt% photoinitiator, which we demonstrate to conduct Li-ions but also not to be stable in contact with Li in the long run. However, its highly viscous nature allows for precise positioning on our  $4 \times 4 \text{ mm}^2 \text{ SiO}_2$ -terminated Si substrates. Bilayer graphene, which we are able to identify, position, pattern, isolate, and electrically contact, may thus be covered only partially by the electrolyte drop. Once solidified by UV curing, the microscopic cell is ready for operation.

#### References

- Manthiram, A.: Materials aspects: an overview. In: Nazri, G.-A., Pistoia, G. (eds.) Lithium Batteries: Science and Technology, pp. 3–41. Springer Science+Business Media, New York (2003)
- Winter, M., Besenhard, J.O.: Lithiated carbons. In: Daniel, C., Besenhard, J.O. (eds.) Handbook of Battery Materials, pp. 433–478. Wiley, Weinheim, Germany (2011)

- 3. Yao, F., et al.: Diffusion mechanism of lithium ion through basal plane of layered graphene. J. Am. Chem. Soc. **134**, 8646–8654 (2012)
- 4. Berry, V.: Impermeability of graphene and its applications. Carbon 62, 1–10 (2013)
- Enoki, T., Endo, M., Suzuki, M.: Graphite Intercalation Compounds and Applications. Oxford University Press, Oxford (2003)
- 6. Bernal, J.D.: The structure of graphite. Proc. Roy. Soc. Lond. A **106**, 749–773 (1924)
- Dresselhaus, M.S., Dresselhaus, G.: Intercalation compounds of graphite. Adv. Phys. 30, 139–326 (1981)
- 8. Kirczenow, G.: Staging and kinetics. In: Zabel, H., Solin, S.A. (eds.) Graphite Intercalation Compounds I. Springer Series in Materials Science, vol. 14, pp. 59–100. Springer, Berlin (1990)
- 9. Dahn, J.R.: Phase diagram of Li<sub>x</sub>C<sub>6</sub>. Phys. Rev. B **44**, 9170–9177 (1991)
- Fong, R., von Sacken, U., Dahn, J.R.: Studies of lithium intercalation into carbons using nonaqueous electrochemical cells. J. Electrochem. Soc. 137, 2009–2013 (1990)
- 11. Sugawara, K., Kanetani, K., Sato, T., Takahashi, T.: Fabrication of Li-intercalated bilayer graphene. AIP Adv. 1, 022103 (2011)
- Holzwarth, N.A.W.: Electronic band structure of graphite intercalation compounds. In: Zabel, H., Solin, S.A. (eds.) Graphite Intercalation Compounds II. Springer Series in Materials Science, vol. 18, pp. 7–52. Springer, Berlin (1992)
- Winter, M., Moeller, K.C., Besenhard, J.O.: Carbonaceous and graphitic anodes. In: Nazri, G.-A., Pistoia, G. (eds.) Lithium Batteries: Science and Technology, pp. 144–194. Springer Science+Business Media, New York (2003)
- Guzman, D.M., Alyahyaei, H.M., Jishi, R.A.: Superconductivity in graphene-lithium. 2D Mater. 1, 021005 (2014)
- Shirodkar, S.N., Kaxiras, E.: Li intercalation at graphene/hexagonal boron nitride interfaces. Phys. Rev. B 93, 245438 (2016)
- Kaloni, T.P., Cheng, Y.C., Upadhyay Kahaly, M., Schwingenschlögl, U.: Charge carrier density in Li-intercalated graphene. Chem. Phys. Lett. 534, 29–33 (2012)
- 17. Peled, E., Golodnitsky, D., Penciner, J.: The anode/electrolyte interface. In: Daniel, C., Besenhard, J.O. (eds.) Handbook of Battery Materials, pp. 479–524. Wiley, Germany (2011)
- 18. Yamaki, J., Tobishima, S.: Rechargeable lithium anodes. In: Daniel, C., Besenhard, J.O. (eds.) Handbook of Battery Materials, pp. 377–404. Wiley, Germany (2011)
- 19. Gray, F., Armand, M.: Polymer electrolytes. In: Daniel, C., Besenhard, J.O. (eds.) Handbook of Battery Materials, pp. 627–656. Wiley, Germany (2011)
- Nair, J.R., Gerbaldi, C., Destro, M., Bongiovanni, R., Penazzi, N.: Methacrylic-based solid polymer electrolyte membranes for lithium-based batteries by a rapid UV-curing process. React. Funct. Polym. 71, 409–416 (2011)
- 21. Nair, J.R., et al.: UV-cured methacrylic membranes as novel gel-polymer electrolyte for Li-ion batteries. J. Power Sources 178, 751–757 (2008)
- 22. Gonnelli, R.S., et al.: Temperature dependence of electric transport in few-layer graphene under large charge doping induced by electrochemical gating. Sci. Rep. 5, 9554 (2015)
- 23. Evans, J., Vincent, C.A., Bruce, P.G.: Electrochemical measurement of transference numbers in polymer electrolytes. Polymer 28, 2324–2328 (1987)
- 24. Popovic, J., Hasegawa, G., Moudrakovski, I., Maier, J.: Infiltrated porous oxide monoliths as high lithium transference number electrolytes. J. Mater. Chem. A 4, 7135–7140 (2016)
- 25. Lafkioti, M.: Untersuchung der 2D Transporteigenschaften von Graphen auf hydrophobem Substrat. Doctoral dissertation. Universität Stuttgart, Germany (2011)
- Novoselov, K.S., et al.: Electric field effect in atomically thin carbon films. Science 306, 666–669 (2004)
- Dean, C.R., et al.: Boron nitride substrates for high-quality graphene electronics. Nat. Nanotech.
   722–726 (2010)
- 28. Ferrari, A.C., et al.: Raman spectrum of graphene and graphene layers. Phys. Rev. Lett. 97, 187401 (2006)
- 29. Nagashio, K., Yamashita, T., Nishimura, T., Kita, K., Toriumi, A.: Electrical transport properties of graphene on SiO<sub>2</sub> with specific surface structures. J. Appl. Phys. **110**, 024513 (2011)

References 59

 ASTM F76-08(2016): Standard test methods for measuring resistivity and Hall coefficient and determining Hall mobility in single-crystal semiconductors. ASTM International, West Conshohocken, USA (2016)

- 31. Bonaccorso, F., et al.: Production and processing of graphene and 2d crystals. Mater. Today 15, 564–589 (2012)
- 32. Pelton, A.D.: The Au-Li (gold-lithium) system. Bull. Alloy Phase Diagr. 7, 228–231 (1986)
- 33. Bale, C.W.: The Li-Ti (lithium-titanium) system. Bull. Alloy Phase Diagr. 10, 135–138 (1989)
- 34. Yazami, R.: Lithium reaction with metal nanofilms. In: Yazami, R. (ed.) Nanomaterials for Lithium-Ion Batteries: Fundamentals and Applications, pp. 199–226. Pan Stanford Publishing, CRC Press, Taylor & Francis Group, Boca Raton, USA (2014)
- Lohmann, T.: Elektronischer Transport in Graphen. Doctoral dissertation, RWTH Aachen, Germany (2010)

## **Chapter 4 Lithiation Studies**



In this chapter we demonstrate the controlled electrochemical lithiation and delithiation of lithographically structured bilayer graphene devices, covered only partially from a Li-ion conducting polymer electrolyte, as schematically shown in Fig. 4.1. The electrochemical process is driven by controlling the potential of bilayer graphene with respect to a counter electrode,  $U_G$ . We expect lithiation (delithiation) at suitable conditions to cause intercalation (deintercalation) of Li-ions into (from) the bilayer, followed by diffusion throughout the latter in order to minimize concentration gradients. Li-ions should thus migrate into the region of the device uncovered from the electrolyte. Due to charge transfer from Li to bilayer graphene, the electronic properties of the latter undergo significant changes during this process.

We reveal some of these by different in situ measurements, all performed with the respective sample at room-temperature and in a high vacuum atmosphere. First, we discuss the zero-field electronic transport in Sect. 4.1, which we combine with Raman spectroscopy in Sect. 4.2. We then turn to magnetotransport measurements in Sect. 4.3. As an addition to these in situ studies, an investigation on the low-temperature magnetotransport behavior of a highly lithiated bilayer graphene device is appended as Sect. 4.4.

#### 4.1 In situ Electronic Transport at Zero Magnetic Field

We measure the electronic transport of charge carriers in a bilayer graphene device, fabricated in a way schematically shown in Fig. 4.2a. We deploy a standard lock-in technique, with a low-frequency (13.33 Hz) excitation current I = 100 nA applied to the bilayer, measuring the longitudinal voltage drop  $U_{xx}$  along the device well outside the electrolyte-covered area in four-point probe geometry. In Fig. 4.2b, we show the sheet resistivity  $\rho_{xx} = W/L \cdot U_{xx}/I$  thus extracted during one lithiation/delithiation cycle. Both the width  $W = 3 \,\mu\text{m}$  of the bilayer as well as the

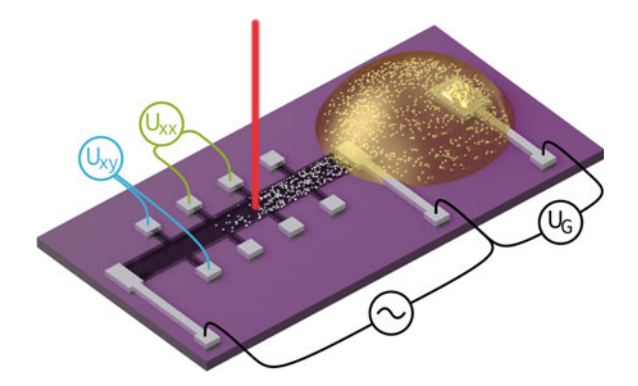


Fig. 4.1 Schematic device design with techniques used to probe electronic properties of bilayer graphene in situ during its electrochemical lithiation/delithiation: measurement of the quasi-dc electronic transport (longitudinal and transverse voltage drops  $U_{xx}$  (green) and  $U_{xy}$  (blue)), as well as Raman scattering (incident Laser beam indicated in red). Bilayer graphene is shown in black, electrical contacts in grey, the SiO<sub>2</sub>-terminated Si-substrate in violet, the electrolyte in yellow and Li-ions as white spheres

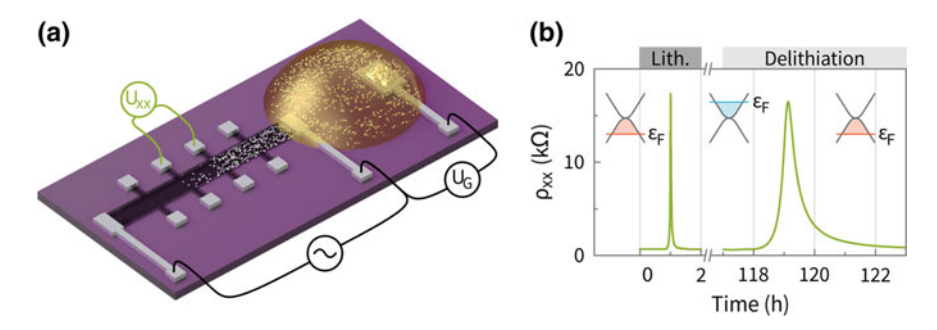


Fig. 4.2 a Schematic device design as in Fig. 4.1. b Longitudinal sheet resistivity  $\rho_{xx}$  of an initially p-doped bilayer graphene device measured in situ during one electrochemical lithiation/delithiation cycle. Insets illustrate the position of the Fermi level  $\epsilon_F$  at three different times

distance  $L=10\,\mu\mathrm{m}$  between neighboring probes used to measured  $U_{xx}$  are determined during patterning of the device. Lithiation (delithiation) was driven at  $U_G=0.02\,\mathrm{V}$  versus Li/Li<sup>+</sup> ( $U_G=2\,\mathrm{V}\,\mathrm{vs}$ . Li/Li<sup>+</sup>) with the sample in a high-vacuum atmosphere ( $p\leq 10^{-6}\,\mathrm{mbar}$ ). Low-temperature experiments, the subject of Chap. 5, were conducted between lithiation and delithiation, accounting for the discontinuity in the time axis.

According to Fig. 4.2b, the sheet resistivity  $\rho_{xx}$  of bilayer graphene experiences drastic changes during lithiation and delithiation, although  $\rho_{xx}$  is measured well outside the electrolyte-covered area of the bilayer. These changes are caused by a charge transfer on the order of e, the elementary charge of an electron, from each intercalating Li-ion to the electronic states of bilayer graphene (see Sect. 3.1.1). In terms of the simplifying rigid band model, this charge transfer shifts the Fermi level  $\epsilon_F$ 

while leaving the dispersion of the host's electronic states unchanged. Consequently, when Li-ions enter bilayer graphene during lithiation,  $\epsilon_F$  shifts further up into the conduction band as the systems gets more and more electron doped. In the reverse case,  $\epsilon_F$  drops during delithiation as Li-ions leave bilayer graphene thereby revoking the charge transfer. This is illustrated in the insets to Fig. 4.2b with the grey lines representing the approximately isotropic dispersion of the lower-lying  $\pi$ -electronic bands around  $K^{(\prime)}$ . For this initially highly p-doped sample (due to a high impurity density  $n_{\rm imp} \approx 1.3 \cdot 10^{13} \, {\rm cm}^{-2}$ ), we start with  $\epsilon_F$  well in the valence band. During lithiation,  $\dot{\epsilon_F}$  slowly shifts towards the conduction band, causing a maximum sheet resistivity  $\rho_{xx}^{\rm CNP} \approx 17.3 \, {\rm k}\Omega$  when crossing the charge neutrality point (CNP).  $\rho_{xx}$  then drops as  $\epsilon_F$  rises further with continued influx of Li-ions providing more electrons to the bilayer electronic states. The subsequent delithiation step, here performed after a few days with the sample at temperatures as low as  $T \approx 1.5$  K, begins with  $\epsilon_F$  still high in the conduction band. As Li-ions leave bilayer graphene during delithiation,  $\epsilon_F$  shifts towards the valence band and we see a concomitant increase of  $\rho_{xx}$  up to about the same maximum value of  $\rho_{xx}^{CNP}$  at the charge neutrality point. Due to the high level of intrinsic p-doping,  $\epsilon_F$  continues to go deeper into the valence band as delithiation proceeds, paralleled with a corresponding decrease of  $\rho_{xx}$ . At the end of this lithiation/delithiation cycle,  $\rho_{xx}$  attains just about the value it had at its beginning, suggesting a high degree of reversibility of the process.

The behavior of  $\rho_{xx}$  measured well outside the electrolyte-covered area supports the assumption that during lithiation Li-ions intercalate into bilayer graphene and diffuse throughout the latter in order to minimize concentration gradients. Due to charge transfer, the electronic states in bilayer graphene get increasingly populated as the Li-concentration rises, thereby shifting  $\epsilon_F$  and causing a related change in  $\rho_{xx}$  akin to its backgate-dependence [1] discussed in Sect. 2.5. However, unlike the straightforward controllability of  $\rho_{xx}$  by a voltage applied to the backgate, here the precise time-evolution of  $\rho_{xx}$  during lithiation (respectively delithiation) likely depends on the Li-diffusion dynamics within the electrolyte, the solid electrolyte interphase (SEI) formed at the bilayer graphene/electrolyte interface as well as the bilayer itself. Microscopic details such as wrinkles, folds, and atomic scale defects in the latter may act as barriers to diffusion. Furthermore, with side-reactions imposing a non-zero degree of irreversibility, each lithiation cycle begins under slightly altered conditions the impact of which on the lithiation kinetics may turn out more drastic in the given case of a single-crystalline electrode than in the conventional case of composite electrodes.<sup>1</sup>

Figure 4.3a shows  $\rho_{xx,i}$  during four successive lithiation/delithiation cycles of a bilayer graphene device (shown in panel b) measured at three neighboring positions i with i = 1 (i = 3) closest (furthest) to the electrolyte. Fig. 4.2b is in fact an excerpt of the shown data for  $\rho_{xx,3}$ . While the three traces of  $\rho_{xx,i}(t)$  nearly overlap, finite differences between them could indicate a spatial nonuniformity of the sample (e.g.,

<sup>&</sup>lt;sup>1</sup>In a macroscopic galvanic cell with composite electrodes, local changes with a critical impact on the local Li diffusion kinetics inflict only a minor change on the overall cycling behavior of the cell.

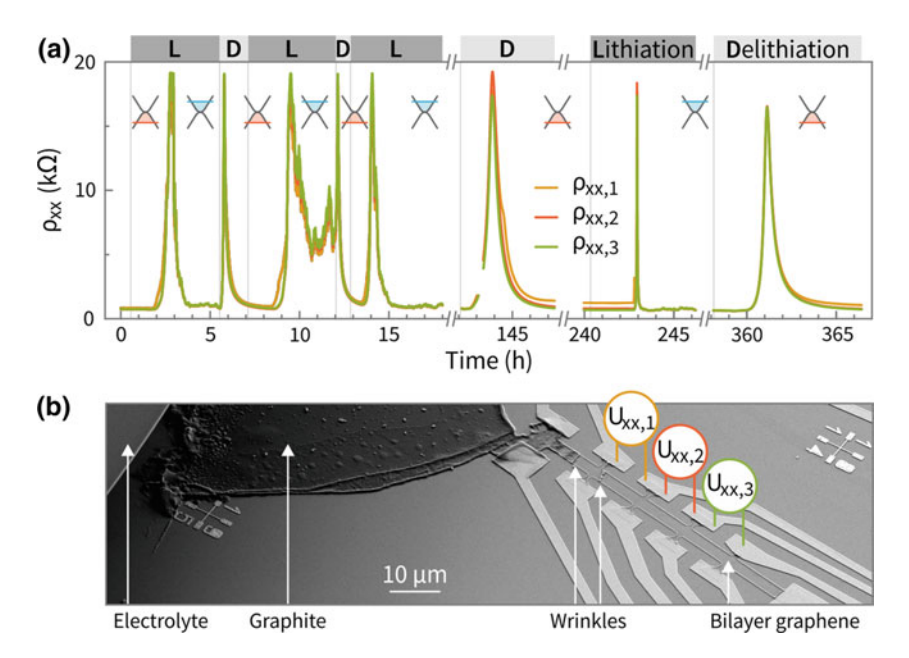


Fig. 4.3 a Sheet resistivity  $\rho_{xx,i}$  measured in situ during four successive lithiation/delithiation cycles of an initially p-doped bilayer graphene device using three neighboring contact pairs i, with i=1 (i=3) closest (furthest) to the electrolyte. Fig. 4.2b is an excerpt of the shown data for  $\rho_{xx,3}$ . As in Fig. 4.2b, insets illustrate the position of the Fermi level  $\epsilon_F$  at different times. b Scanning electron micrograph of the bilayer graphene device after cycling. Ti contact pairs for measurements of longitudinal voltage drops  $U_{xx,i}$  used to extract  $\rho_{xx,i}$  are indicated in the same color as respective data in (a)

due to an inhomogeneous distribution of impurities) or of the Li diffusion process (the subject of Chap. 7). They could further stem from irreversible processes during lithiation. For example,  $\rho_{xx,1}(t \ge 144 \text{ h})$  never drops back to  $\rho_{xx,1}(0)$  during delithiation, which could be due to a wrinkle across the bilayer within the probed area (indicated in the scanning electron micrograph in Fig. 4.3b) at which immobilized Li reaction products are found to agglomerate with time. Such decorations are subject to more in-depth discussion in Chap. 6. More striking however is the overall difference between  $\rho_{xx,i}(t)$  for successive lithiation/delithiation cycles. Despite polarization durations being unequally long,  $\rho_{xx,i}(t)$  during delithiation steps show a higher degree of resemblance than during lithiation steps. The rate limiting factor is thus mainly determined by the diffusion kinetics in the electrolyte and/or the SEI, which are susceptible to modifications due to cycling (as SEI formation continues and its microstructure changes) or due to ageing. Thus, the second lithiation in Fig. 4.3a appears hampered with  $\rho_{xx,i}(t)$  fluctuating at values above 5 k $\Omega$  which is not related to problems in the bilayer, but rather to limitations on the Li-influx. Note that in addition to what was said before, the bilayer here is connected to the electrolyte via a natural connection to a bulk graphite single crystal, see Fig. 4.3b. Possible intercalant ordering in this bulk part might further impede the migration of Li into the bilayer. If Li-ions are provided quickly enough, as during the fourth lithiation in Fig. 4.3a,  $\rho_{xx,i}(t)$  changes equally fast at all three contact pairs, indicating a high intrinsic Li diffusion coefficient in bilayer graphene. Its quantitative determination is discussed in Chap. 7.

The continuous change of  $\rho_{xx}$  in bilayer graphene during lithiation cycles has not been experimentally demonstrated before. However, it is known that the intercalation of bulk graphite lends the resulting compound a metallic character, in contrast with the semi-metallic one of graphite itself [2]. A reduction of the anisotropy in the electronic conductivity  $\sigma_a/\sigma_c$  from 3000 in HOPG to 14 in LiC<sub>6</sub> has been reported, with an approximately 10-fold increase in the in-plane conductivity from  $\sigma_a \approx 2.5 \cdot 10^4 \, \Omega^{-1}$ cm<sup>-1</sup> in HOPG to  $\sigma_a \approx 2.5 \cdot 10^5 \,\Omega^{-1} \,\mathrm{cm}^{-1}$  in LiC<sub>6</sub>, nearing the room-temperature conductivity of copper  $\sigma_{Cu} \approx 6 \cdot 10^5 \,\Omega^{-1} \,\mathrm{cm}^{-1}$  [3]. Here,  $\sigma_c$  is the out-of-plane conductivity in graphite (parallel to the c-axis). Also in bulk graphite, the increase in the in-plane conductivity is generally understood as being due to charge transfer from the intercalate layer to the graphene planes [3]. An increase in  $\sigma_a$  upon Li intercalation has been demonstrated also in few-layer graphene samples with a thickness down to five layers. In this work, Bao et al. [4] report maximum room-temperature values of  $\sigma_a^{\text{max}} \approx 11 \text{ mS}$  per layer in LiC<sub>6</sub>, claimed to be one third of the intrinsic limit set by electron-acoustic phonon scattering. In the case of our device discussed in this section, the minimum room-temperature sheet resistivity obtained after lithiation  $\rho_{xx} \approx 700 \,\Omega$  yields  $\sigma_a \approx 0.7$  mS per layer indicating most likely a yet incomplete intercalation. It should be noted however, that the difference between the conductivity in a pristine bilayer graphene flake with respect to a fully Li intercalated one is likely much higher than the factor of  $\sim 10$  reported for bulk graphite [3], as Bao et al. [4] report values up to about 50 for few-layer samples and we find a factor of about 30 when comparing the value at charge neutrality  $\sigma_a^{\rm CNP} \approx 0.025$  mS per layer to our minimum after lithiation  $\sigma_a \approx 0.7$  mS per layer. If indeed at full Li-content  $\sigma_a^{\text{max}} \approx$ 11 mS per layer, the increase in conductivity with respect to the pristine state would exceed a factor of 400. To our knowledge, such a high value would be unprecedented for Li-intercalated graphitic carbon.

#### 4.2 In situ Raman Spectroscopy

The spectrum of light scattered inelastically from graphitic carbon reveals a number of efficient scattering processes that involve different lattice vibrational modes in the crystal, [5] see Sect. 2.8. Among these, a first order Raman scattering process involving the zone-center optical  $E_{2g}$ -phonon mode gives rise to the pronounced Raman G band at the energy  $\epsilon(G) \approx 1575 \text{ cm}^{-1}$  in bulk graphite [6]. This Raman G band is highly susceptible to the intercalation of guest ions, [3] which has been reported for the relevant case of Li-intercalated graphite, [7, 8] in particular from in situ measurements of the Raman scattering response during the gradual electrochemical intercalation of Li [9, 10] The response was found to strongly depend

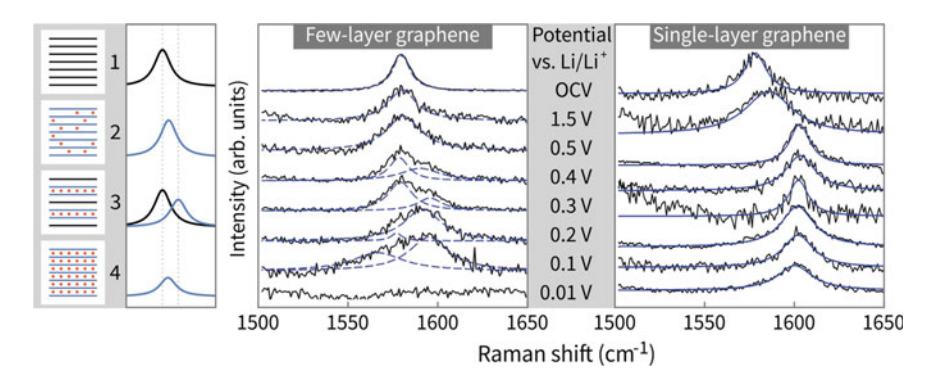


**Fig. 4.4** In situ Raman spectra of a few-layer graphene electrode (left panel main graph) and a single-layer graphene electrode (right panel main graph) at selected potentials during electrochemical lithiation (OCV stands for open circuit voltage). Blue lines in main graph are reported Lorentzian fits. A schematic of the commonly observed Raman G band evolution during Li intercalation into graphitic carbon is given on the left. (1) Pristine state, (2) dilute stage 1, (3) high stage-index intercalation compound, (4) LiC<sub>6</sub>. Insets illustrate the respective distribution of Li (red dots) in graphitic carbon, with bounding graphene layers (blue) and interior graphene layers (black) giving rise to the respectively colored G band component. Adapted with permission from Ref. [11]. Copyright 2010 American Chemical Society

on the dimensionality of the sample, which we briefly discuss on the basis of data summarized in Fig. 4.4 as reported by Pollak et al. [11].

Pollak et al. [11] performed in situ Raman spectroscopy during the electrochemical lithiation of few-layer graphene (left panel main graph) and single-layer graphene (right panel main graph). At open circuit potential (OCV), i.e., prior to lithiation, a single-Lorentzian Raman G band is measured in both cases. During the lithiation of few-layer graphene, this Raman signal is observed first to split and then to disappear with decreasing potential versus Li/Li<sup>+</sup>, i.e., with increasing Li content. Not experimentally resolved is a blueshift of the G band (shift to higher wavenumber) prior to its splitting, commonly observed in graphitic carbons with a low concentration of intercalated Li [4, 9, 10, 12–14] The main features of the G band evolution may be captured as schematically shown left to the main graph in Fig. 4.4 (using the same numbering):

- 1. Pristine state with a single-Lorentzian G band.
- 2. Dilute stage 1 with a blueshifting G band upon increasing Li-content. Charge transfer from the intercalant to the graphene layers causes a stiffening of the  $E_{2g}$ -phonon mode as it increases the force constant of the in-plane C-C bonds, similar to the behavior observed in electrostatically doped single-layer graphene [15–17].
- 3. Staging with a high stage index causes a split G band with a low (high) frequency component from the so-called interior (bounding) graphene layers, respectively. Bounding layers are located directly next to an intercalant-filled gallery, efficiently screening the intercalant as they receive all or most of the transferred charge [3]. They give rise to a blueshifted G band component for the same reason

- as in (2). Interior layers, which are neighboring only unoccupied galleries, receive no charge and hence give rise to the low-wavenumber G band component. Both G band components are observed to redshift (shift to lower wavenumbers) with increasing reciprocal stage index (1/n), which has been attributed to an in-plane tensile strain due to lattice expansion [3, 8, 18].
- 4. Approaching the maximum Li-content, LiC<sub>6</sub>, only bounding layers remain and thus one obtains a single spectral line near 1600 cm<sup>-1</sup> [7, 8]. Its observation is however suppressed in most experiments, as the optical skin depth is strongly reduced due to the high electrical conductivity of these lowest-stage compounds [4, 9–14].

Unlike the case of few-layer graphene, the Raman G band of single-layer graphene does not split during lithiation as staging is impossible, see the rightmost panel in Fig. 4.4. The G band is rather observed to shift from initially 1586 cm<sup>-1</sup> up to 1602 cm<sup>-1</sup> during cathodic polarization, [11] attributed to the stiffening of the  $E_{2\sigma}$ -phonon mode due to electron doping [15–17]. A similar absence of a G band splitting was reported in Ref. [18] for Li-intercalation in 3-layer graphene. Though what seems obvious for the case of single-layer graphene is not for 3-layer graphene. If the Li intercalant was to occupy only one of the two available van der Waals-gaps, the three graphene layers would receive unequal amount of charge with one sheet likely retaining the character of an interior layer in bulk graphite. In that respect, bilayer graphene is again a less complex case offering no platform for stage ordering. The possibility of inducing a splitting of the Raman G band in bilayer graphene has however been demonstrated via an electric field-induced asymmetric charge distribution on its two layers [19, 20]. Such a splitting is experimentally not resolved when the charge carrier density is varied only in a small interval  $\Delta n \approx \pm 10^{13} \text{ cm}^{-2}$ around the charge neutrality point, [21] or if an equal charge distribution is enforced, e.g, by deliberately shortcutting both layers [22]. At the time of this writing, no in situ Raman study during the Li intercalation in bilayer graphene has been reported.

We measure the Raman scattering response of bilayer graphene samples in situ during their controlled electrochemical lithiation/delithiation. To this end we perform micro-Raman spectroscopy in backscattering configuration, with an unpolarized helium-neon laser beam ( $\lambda = 632.8$  nm) focused onto the bilayer with a spot size near the diffraction limit (diameter < 1  $\mu$ m) and a power well below 1 mW. A low-frequency ac-current applied to the device allows for the simultaneous measurement of the longitudinal voltage drop  $U_{xx}$  using standard lock-in techniques, identical to the procedure discussed in the previous Sect. 4.1. As schematically illustrated in Fig. 4.5a, the Raman scattering response is measured in a region of bilayer graphene well outside the electrolyte-covered area. Typical acquisition times are 1 min/spectrum. Since the experiment is performed with the sample in a high-vacuum atmosphere (with typically  $p < 10^{-5}$  mbar), both the incident and reflected light pass through a quartz glass window of a home-made vacuum chamber.

In Fig. 4.5b we show the Raman scattering response of two bilayer graphene devices A and B measured each during one lithiation/delithiation cycle. A1 and A2 are measured on the same device A, only on different positions during two consecutive

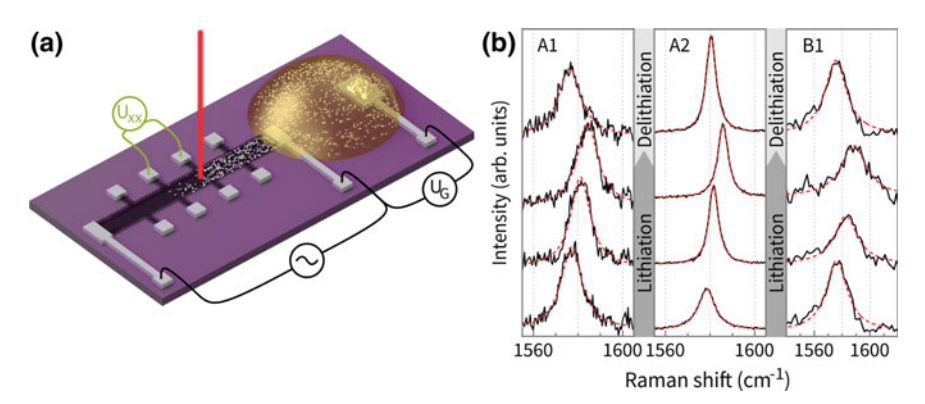
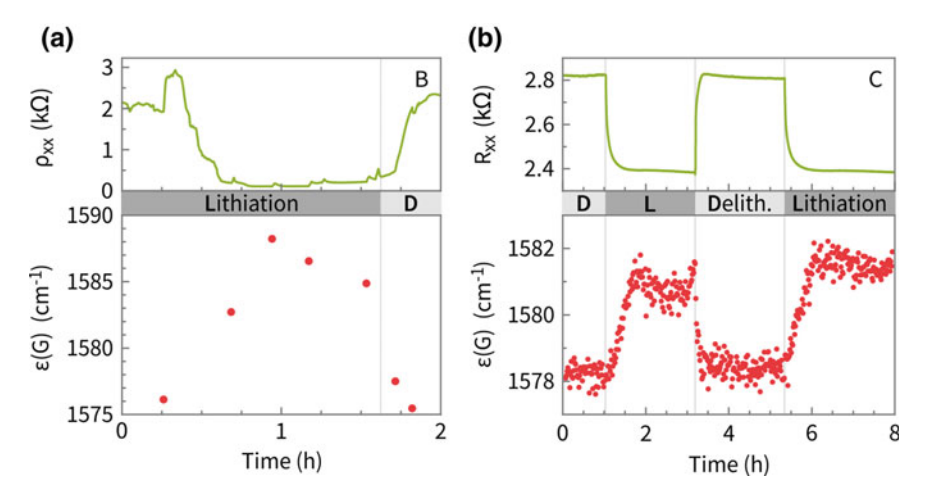


Fig. 4.5 a Schematic device design as in Fig. 4.1. b Raman G band evolution of bilayer graphene devices measured during a lithiation/delithiation cycle (black lines). A1 and A2 are measured on the same device A, only on different positions during two consecutive cycles. B1 is measured on a different device. Intensity scales are not the same for the three panels. From bottom to top, the first three spectra in each panel are for increasing Li content (extended lithiation), while the topmost spectrum is after delithiation. Dashed red lines are single-Lorentzian fits to the signal. The excitation laser wavelength is  $\lambda = 632.8$  nm

cycles. The signal to noise ratio for A2 is best as it was acquired from a region of the bilayer suspended over a hole in the  $SiO_2$ . At the beginning of lithiation, we observe the Raman G band centered at  $1577 \, \mathrm{cm}^{-1}$ ,  $1578 \, \mathrm{cm}^{-1}$ , and  $1576 \, \mathrm{cm}^{-1}$  for A1, A2, and B1, respectively. During lithiation, the G band is found to blueshift in all three cases, up to  $1584 \, \mathrm{cm}^{-1}$ ,  $1586 \, \mathrm{cm}^{-1}$ , and  $1588 \, \mathrm{cm}^{-1}$  for A1, A2, and B1, respectively. After delithiation (topmost spectrum in each panel in Fig. 4.5b), the G band has returned close to its original position. In all cases, the measured signal has a single-Lorentzian line shape as we demonstrate by fitting the data accordingly, see the red dashed lines in the figure. The center of each Lorentzian gives the energy of the Raman G band  $\epsilon(G)$ . Note that the absence of a splitting suggests an even distribution of transferred charge among both graphene layers. Therefore, we determine the Raman G band behavior during Li intercalation in bialyer graphene to be qualitatively similar to the one of single layer graphene shown in Fig. 4.4.

In Fig. 4.6, we show  $\epsilon(G)$  extracted from in situ measurements of the Raman scattering response of two graphene bilayers B and C during lithiation/delithiation. Device B (Fig. 4.6a) was a single-crystalline bilayer, lithographically etched into a Hall bar, and thus the sheet resistivity could be extracted in a straightforward manner from a simultaneous in situ measurement of the electronic transport. Here, a shutter was used to prevent the laser light from illuminating the sample after the acquisition of each spectrum (integration time 60 s). During each acquisition we observe a laser-induced change in the measured sheet resistivity, likely due to the charging of trap states in the SiO<sub>2</sub> [23]. The overall behavior is however governed by a strong decrease in resistivity during lithiation, and a respective increase during delithiation. For this sample, we estimate an initial electron density  $n_e(t=0) \approx 4 \cdot 10^{12}$  cm<sup>-2</sup> from a



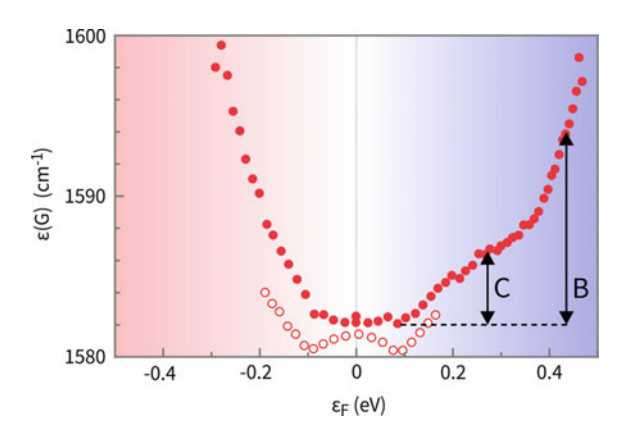
**Fig. 4.6** Sheet resistivity  $\rho_{xx}$  or longitudinal resistance  $R_{xx}$  (upper panels) and energy of the Raman G band  $\epsilon(G)$  (lower panels) measured in situ during lithiation (L)/delithiation (D) of two bilayer graphene devices, (**a**) device B and (**b**) device C

backgate sweep performed prior to lithiation (according to the procedure described in Sect. 2.5). Since intercalating Li only increases the electron density in bilayer graphene further, a decrease (increase) in  $\rho_{xx}$  during lithiation (delithiation) is in agreement with our findings presented in the previous Sect. 4.1. The shift in energy of the Raman G band is paralleled with a considerable change in the sheet resistivity, plausible for the scenario of a diffusing intercalant.

The reversibility of the process is demonstrated again in an excerpt of the measurement on device C, see Fig. 4.6b. Here, the bilayer was continuously exposed to the laser illumination whilst a resistance  $R_{xx}$  was extracted from measuring the voltage drop across an attached graphene few-layer. Although the absolute value of  $R_{xx}$  is not meaningful, we again observe the parallel evolution of both resistance and Raman G band energy  $\epsilon(G)$  in bilayer graphene, as lithium diffuses into and out of the device.

For a tentatively quantitative conclusion, we attempt to compare the magnitude of the observed shifts  $\Delta\epsilon(G)$  to experimentally determined energies of the Raman G band  $\epsilon(G)$  as a function of Fermi energy  $\epsilon_F$ , reported from electrostatic gating experiments on bilayer graphene, [21, 22] see Fig. 4.7. Here, we select experimental work which reports no splitting of the Raman G band upon doping as in our experiment. This suggests an equal distribution of charge among both carbon layers. According to theoretical calculations from Ando [24], the behavior of  $\epsilon(G)$  as a function of  $\epsilon_F$  should feature two cusps at  $\pm\hbar\omega_{\rm ph}/2$  due to a logarithmic singularity in the perturbative renormalization of the phonon energy. Here,  $\omega_{\rm ph}$  is the frequency of the E<sub>2g</sub>-phonon involved in the scattering process of the Raman G band. According to Fig. 4.7, only the data from Ref. [21] (open circles) features these cusps at  $\approx \pm 0.1$  eV as the charge inhomogeneity in the studied sample was reportedly low enough,

Fig. 4.7 Experimentally determined energy  $\epsilon(G)$  of the Raman G band in bilayer graphene from Refs. [21] (open circles) and [22] (filled circles). In both experiments the Fermi energy  $\epsilon_F$  was varied by electrostatic doping. The maximum shift  $\Delta\epsilon(G)$  due to Li intercalation observed for samples B and C in Fig. 4.6 is given by the double-headed arrows, which are offset for comparison



i.e., well below  $2\cdot 10^{12}~{\rm cm}^{-2}$ . In the case of Ref. [22] (filled circles), the charge inhomogeneity was higher and consequently  $\epsilon(G)$  is approximately constant around the charge neutrality point. For  $\epsilon_F>0.1~{\rm eV}$ , both experiments report a blueshift of the Raman G band with comparable slope.

Thus, we roughly compare the maximum shift  $\Delta\epsilon(G)\approx 4\,\mathrm{cm}^{-1}$  from our sample C (see Fig. 4.6b) to the electron-doped side of the data of Das et al. [22], as indicated by the respective double headed arrow in Fig. 4.7. The given shift in  $\epsilon(G)$  translates to an approximate change in Fermi level of  $\Delta\epsilon_F\approx 0.2\,\mathrm{eV}$ . According to Sect. 2.3 this value corresponds to a change in charge carrier density on the order of  $\Delta n\approx 1\cdot 10^{13}\,\mathrm{cm}^{-2}$ . For sample B the lithiation-induced shift of the Raman G band is  $\Delta\epsilon(G)=12\,\mathrm{cm}^{-1}$  (see Fig. 4.6a). According to Fig. 4.7, the Fermi level in sample B was thus likely raised beyond 0.4 eV, corresponding to a charge carrier density in excess of  $2\cdot 10^{13}\,\mathrm{cm}^{-2}$ . We shall see in the following, how to extract the Li concentration from these numbers.

#### 4.3 In situ Magnetotransport

The application of a magnetic field B perpendicular to a bilayer graphene device allows for the in situ measurement of the Hall voltage  $U_{xy}$  during its lithiation/delithiation. As introduced in Sect. 2.6, for a two-dimensional material with a single charge carrier type  $U_{xy}$  can be written as [25]

$$U_{xy} = \frac{IB}{nq},\tag{4.1}$$

where I is the magnitude of the applied current, B = |B| is the magnetic field strength, n is the charge carrier density per unit area, and q is the amount of charge per carrier. From Eq. 4.1 one can extract the so-called Hall coefficient

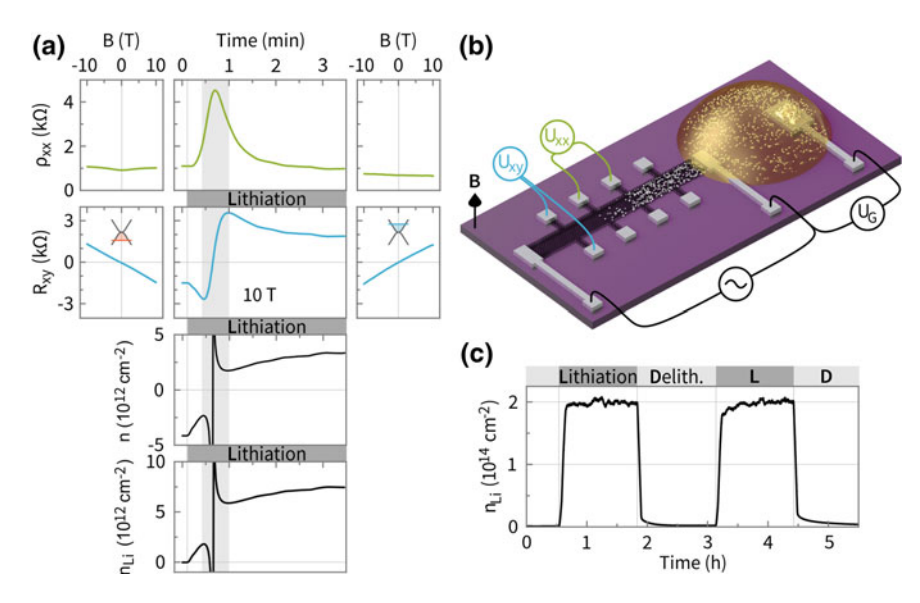


**Fig. 4.8** a Magnetotransport (graphs in the upper two rows) of charge carriers in an initially p-doped bilayer graphene device schematically shown in (b), measured before (left column), during (central column), and after (right column) lithiation. From the in situ Hall measurement (performed at B = 10 T) we extract the density n (third row) of electrons (positive values)/holes (negative values) as well as the intercalated Li density  $n_{\text{Li}}$  (last row). In the grey shaded area, the extraction of  $n_{\text{Li}}$  is not possible as explained in the text.  $\mathbf{c}$   $n_{\text{Li}}$  determined from an in situ Hall measurement (performed at B = 10 T) during lithiation/delithiation of a different, initially n-doped bilayer graphene device

$$R_H = \frac{U_{xy}}{IB} = \frac{R_{xy}}{B} = \frac{1}{nq},$$
 (4.2)

which is a material constant.  $R_H$  yields access to both the sign and the amount of charge transferred from the intercalant to the host [3]. From Hall effect measurements it has been confirmed that during the intercalation of Li indeed electrons are transferred to the electronic states of graphitic carbon [4]. The volumetric density of transferred charge has been found to be independent of sample thickness, at least down to 4-layer graphene [4]. However, no Hall measurements on Li-intercalated bilayer graphene have been reported at the time of this writing.

We measure the magnetotransport during lithiation/delithiation of bilayer graphene devices etched into Hall bar shapes (schematically shown in Fig. 4.8b) either in alternating current (ac) mode or in direct current (dc) mode. In combination with standard lock-in techniques the former method offers a high measurement precision. Therefore, commonly it is our method of choice. However, for time-resolved experiments with up to several hundred measurements of  $U_{xy}$  per minute, we employ the dc method. As according to Eq. 4.1  $U_{xy} \propto 1/n$ , the high electron density n in bilayer graphene that we expect from Li-intercalation would render  $U_{xy}$  very small. We therefore perform the experiment in a cryogen-free superconducting magnet

system, with the sample subject to a perpendicular magnetic field B up to 12 T at room temperature. The current I is chosen such that the potential drop across bilayer graphene is small with respect to the potential  $U_G$  versus Li/Li<sup>+</sup>. I.e., for a typical longitudinal resistance in the k $\Omega$ -range we choose  $I \leq 1 \,\mu\text{A}$ , so that the magnitude of the potential drop is small with respect to  $U_G = 50 \,\text{mV}$  versus Li/Li<sup>+</sup> applied during lithiation.

In the top two rows of Fig. 4.8a, we show the magnetotransport of charge carriers in an initially p-doped bilayer graphene device measured before (left column), during (central column), and after (right column) lithiation. This experiment was performed in ac mode. From the linear dependence of  $R_{xy}(B)$  observed during the first magnetic field sweep, we extract the density of holes due to p-doping from impurities to amount to  $n_{\rm imp} = 4.57 \cdot 10^{12} \ {\rm cm}^{-2}$ . The slope of  $R_{xy}(B)$  has opposite sign after lithiation as the charge carrier type has changed to electrons with a density of  $n_e = 4.42 \cdot 10^{12} \ {\rm cm}^{-2}$ . During lithiation at  $B = 10 \ {\rm T}$ ,  $R_{xy}$  shows a smooth zero crossing as the Fermi level shifts through the charge neutrality point (CNP) due to charge transfer from the continuous influx of lithium. Within the grey shaded area in the graph, the magnetotransport is governed by electron-hole puddles. Here, both n and  $n_{\rm Li}$  can not be extracted reliably as an accurate description requires a two charge carrier type model. Consistently,  $\rho_{xx}$  passes through a maximum at charge neutrality, in line with our observations during in situ experiments at B = 0 in Sect. 4.1.<sup>2</sup>

In the third row of Fig. 4.8a we plot the charge carrier density n as extracted from  $R_{xy}$ , negative (positive) values of which stand for holes (electrons), respectively. Except for the electron-hole puddle regime (extending over  $\approx \pm 2 \cdot 10^{12}$  cm<sup>-2</sup> around charge neutrality) in which Eq. 4.2 does not hold, we observe a continuous accumulation of negative charges in bilayer graphene. Assuming a complete charge transfer of 1e per intercalated Li<sup>+</sup>, the measured increase in density of electrons in bilayer graphene equals the intercalated Li density  $n_{Li}$ . Thus using the charge carrier density  $n_{Li}$  as shown in the third row of Fig. 4.8a,  $n_{Li}$  can be extracted as

$$n_{\rm Li}(t) = n(t) - n_{\rm imp}.$$
 (4.3)

For the given sample, we plot this temporal evolution of the Li concentration  $n_{\text{Li}}$  in the bottom row of Fig. 4.8a.

In Fig. 4.8c, we show  $n_{\rm Li}(t)$  extracted according to the preceding discussion from a dc magnetotransport measurement (performed at  $B=10\,\rm T$ ) on an initially n-doped bilayer graphene device during repeated intercalation (deintercalation) of lithium at  $U_G=0.05\,\rm V$  versus Li/Li<sup>+</sup> ( $U_G=1.5\,\rm V$  vs. Li/Li<sup>+</sup>). In this sample, the electron density reaches a maximum value of approximately  $2\cdot 10^{14}\,\rm cm^{-2}$ . In fact, this can

<sup>&</sup>lt;sup>2</sup>Note that  $\rho_{xx}$  shows no significant dependence on *B* before and after lithiation as can be expected from a system conforming to a single-band Drude model [25]. In the region of electron-hole puddles however, the magnitude of  $\rho_{xx}$  may be affected by the presence of a finite magnetic field. Nevertheless, in Sect. 2.6 we demonstrated  $\rho_{xx}$  to keep its qualitative appearance upon a variation of *n*, featuring a single maximum at charge neutrality. It is along these lines that we may attempt a qualitative comparison to the behavior of  $\rho_{xx}$  at zero magnetic field in Sect. 4.1.

be considered as a lower limit for the Li density  $n_{\rm Li}$  in case the charge transfer ratio is less than the assumed value of one (see Sect. 3.1.1 for discussion). Upon initiating delithiation, the carrier density is observed to return close to its original value, demonstrating again the high degree of reversibility of the Li-intercalation process. Such an in situ magnetotransport measurement thus provides a powerful tool to not only reveal intercalated Li having diffused away from the interface with the electrolyte, but also to monitor its local concentration with time.

#### 4.4 Low-Temperature Magnetotransport

The magnetotransport of charge carriers in a bilayer graphene device with a high density of intercalated Li is shown in Fig. 4.9. The measurement was performed after lithiation at room-temperature and a subsequent cool-down to T = 1.5 K inside a cryogen-free superconducting magnet system. A sweep of the magnetic field applied perpendicular to the bilayer reveals an approximately parabolic dependence on the field strength B of the sheet resistivity  $\rho_{xx}$  (Fig. 4.9a) as well as a virtually linear Hall resistance  $R_{xy}$  (Fig. 4.9b). From a linear fit to  $R_{xy}(B)$  according to Eq. 4.2 we obtain the charge carrier density  $n = 2.3 \cdot 10^{14} \, \mathrm{cm}^{-2}$ . The initial electron density from impurities in this device amounts to  $n_{\rm imp} = 2 \cdot 10^{12} \, {\rm cm}^{-2}$ , extracted from a lowtemperature Hall measurement prior to lithiation. Consequently, using Eq. 4.3, we obtain a Li concentration of  $n_{\rm Li} = 2.28 \cdot 10^{14} \, {\rm cm}^{-2}$ . This is more than a third of the theoretical maximum  $n_{\rm Li}^{\rm max} \approx 6.36 \cdot 10^{14} \, {\rm cm}^{-2}$ , and corresponds to a stoichiometry of approximately C<sub>18</sub>LiC<sub>18</sub>. It is the highest density of intercalated Li achieved in this work. Note that the actual value of  $n_{Li}$  is higher if the charge transferred between an intercalated Li atom and the electronic states of bilayer graphene is only a fraction of e. We can state, however, that the charge transfer amounts to at least e/3.

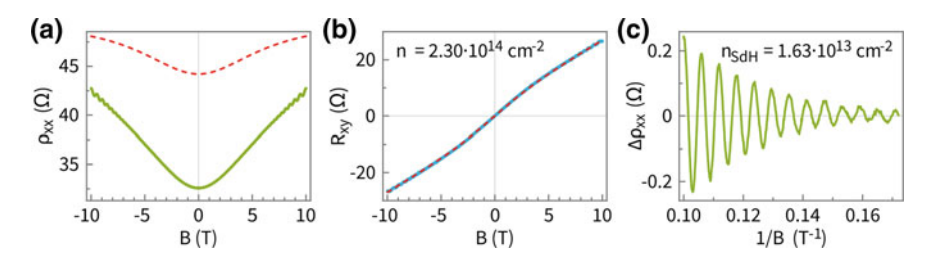


Fig. 4.9 a Sheet resistivity  $\rho_{xx}$  (green solid line) and **b** Hall resistance  $R_{xy}$  (blue solid line) of a Li-intercalated bilayer graphene device measured at T = 1.5 K. The charge carrier density n from a linear fit to the Hall data (Eq. 4.2) is given. Red dashed lines are calculated from the two-carrier model as described in the text. **c** Changes of the sheet resistivity  $\Delta \rho_{xx}$  due to Shubnikov-de Haas (SdH) oscillations, extracted from (**a**) by subtraction of the parabolic background. The associated charge carrier density  $n_{\text{SdH}}$  is shown in the figure

At such a high Li content, we expect the second  $\pi$ -band of bilayer graphene (in the following denoted as higher energy subband, HES) to be partially occupied, see Sect. 2.3 and especially Fig. 2.3. Both the parabolic B-dependence of  $\rho_{xx}$  as well as the Shubnikov-de Haas (SdH) oscillations, clearly resolved in the high-field region of Fig. 4.9a, also suggest the participation of more than one type of charge carrier in the transport, as we shall see. We first analyze the SdH oscillations, which we find to be composed of a single frequency component  $f_{\text{SdH}}$  periodic in  $B^{-1}$ , see Fig. 4.9c. Here, a parabolic background in  $\rho_{xx}(B)$  was subtracted from the data shown in panel a, to obtain the remaining  $\Delta \rho_{xx}$  shown in panel c. Assuming each Landau level to be fourfold degenerate, we extract the density of the charge carrier type associated with this frequency according to Eq. 2.18 as

$$n_{\text{SdH}} = \frac{4 \cdot e}{h} \cdot f_{\text{SdH}} = 1.63 \cdot 10^{13} \text{cm}^{-2}.$$
 (4.4)

This density is much smaller than the overall charge carrier density extracted from the Hall measurement. We therefore presume that  $n_{\rm SdH}$  represents charge carriers in the higher energy subband, as their density  $n_{\rm HES}$  is expected to be smaller than the one in the lower energy subband (LES). I.e.,  $n_{\rm HES} = n_{\rm SdH}$ . In line with the procedure of Efetov et al. [26], we extract the density of charge carriers in the lower energy subband as  $n_{\rm LES} = n - n_{\rm HES}$ , where n is the total density extracted from the fit to the Hall measurement discussed above. We thus find  $n_{\rm LES} = 2.137 \cdot 10^{14} \, {\rm cm}^{-2}$ .

Due to this clear evidence for the presence of more than one type of charge carrier, we employ a multi-band description for the magnetotransport. A simple approach is to add the contributions  $\hat{\sigma}_i$  from the individual bands i to obtain the total conductivity [25]

$$\hat{\sigma} = \sum_{i} \hat{\sigma}_{i}. \tag{4.5}$$

For two types of negatively charged carriers with mobility  $\mu_i$  and density  $n_i$  (where i = 1 for the LES and i = 2 for the HES),

$$\sigma_{xx,i} = \frac{n_i e \mu_i}{1 + (\mu_i B)^2}$$
 and  $\sigma_{xy,i} = -\frac{n_i e \mu_i^2 B}{1 + (\mu_i B)^2}$ , (4.6)

according to Eq. 2.16. One obtains from tensor inversion

$$\rho_{xx}(B) = \frac{n_1 \mu_1 + n_2 \mu_2 + \mu_1 \mu_2 (n_1 \mu_2 + n_2 \mu_1) B^2}{e(n_1 \mu_1 + n_2 \mu_2)^2 + e\mu_1^2 \mu_2^2 (n_1 + n_2)^2 B^2},$$
(4.7)

$$\rho_{xy}(B) = \frac{(n_1\mu_1^2 + n_2\mu_2^2)B + \mu_1^2\mu_2^2(n_1 + n_2)B^3}{e(n_1\mu_1 + n_2\mu_2)^2 + e\mu_1^2\mu_2^2(n_1 + n_2)^2B^2}.$$
 (4.8)

With the help of Eq. 4.8 we obtain a satisfactory fit to  $R_{xy}(B)$  in Fig. 4.9b (red dashed line) for  $n_2 = n_{\text{SdH}}$  as well as  $n_1 = 2.38 \cdot 10^{14} \text{ cm}^{-2}$ ,  $\mu_1 = 470 \text{ cm}^2/\text{Vs}$ ,

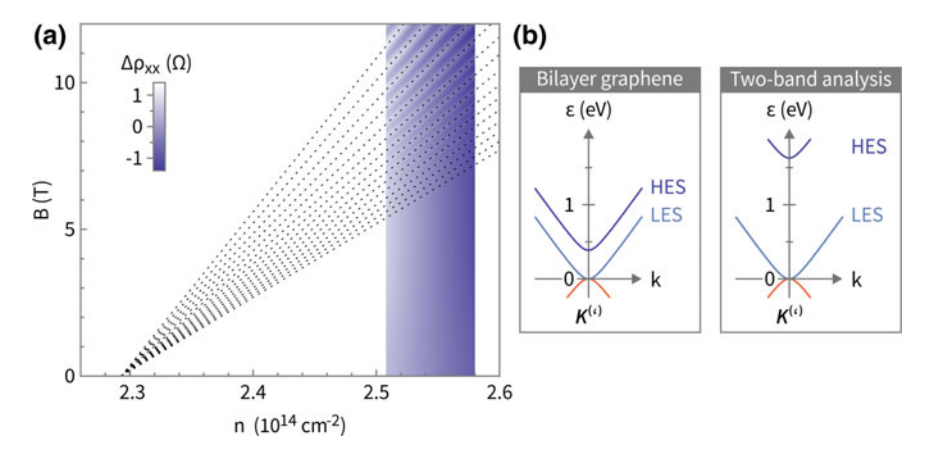


**Fig. 4.10** a Shubnikov-de Haas (SdH) oscillations in a Li-intercalated bilayer graphene device at T=1.5 K. False color plot of changes in sheet resistivity  $\Delta \rho_{xx}$ , measured at a fixed Li-content. Dashed lines are extrapolations of the position in charge carrier density n of observed SdH maxima to B=0 T. **b** Dispersion of the lower (LES) and higher (HES) energy subband in bilayer graphene around  $K^{(\prime)}$  in its pristine state (left) and in the highly lithiated state as suggested from assigning the SdH oscillation-derived density to the HES (right).

and  $\mu_2 = 1800 \text{ cm}^2/\text{Vs.}^3$  Note that the total charge carrier density  $n' = n_1 + n_2 = 2.543 \cdot 10^{14} \text{ cm}^{-2}$  obtained via the multiband approach is about 10% higher than our initial finding of n obtained from the linear fit to  $R_{xy}(B)$  using Eq. 4.2. Given the oversimplification of the latter method, the values of n and n' are still appreciably close. Note however that although Eq. 4.7 qualitatively reflects the observed B-dependence of  $\rho_{xx}$ , we do not obtain a convincing fit using the aforementioned parameters, see red dashed line in Fig. 4.9a. Uncertainties in the determination of the aspect ratio of the active sample area alone, needed to extract  $\rho_{xx}$  from our measurement, can not satisfyingly account for the observed deviation.

Most striking, however, is the big discrepancy between the obtained charge carrier densities in the lower and higher energy subband, irrespective of the method chosen to determine  $n_{\rm LES}$ . If the rigid band model was to hold, then during intercalation the electronic states of the host would remain unchanged and only the Fermi level  $\epsilon_F$  would shift due to charge transfer. Applying that scenario to bilayer graphene (using the methodology of Sect. 2.3), a total density  $n'=2.543\cdot 10^{14}~{\rm cm}^{-2}$  would imply  $\epsilon_F\approx 1.35~{\rm eV}$  at which we expect  $n_{\rm LES}=1.64\cdot 10^{14}~{\rm cm}^{-2}$  and  $n_{\rm HES}=9.03\cdot 10^{13}~{\rm cm}^{-2}$ . In comparison, our value of  $n_{\rm HES}=1.63\cdot 10^{13}~{\rm cm}^{-2}$  extracted from the observed SdH oscillations is far too small. In Fig. 4.10a, varying the voltage

 $<sup>^3</sup>$ A more than three times greater value of  $\mu_2$  compared to  $\mu_1$  at a given value of n has been reported before from electrolyte-gating experiments on bilayer graphene [26]. An explanation for this finding is the always lower effective mass in the higher energy subband at each value of n, see Fig. 2.3. A further enhancement of  $\mu_2$  may result from the more efficient screening of charged impurities at high n, resulting in an effectively reduced scattering of charge carriers in the higher energy subband on these scattering sites [26].

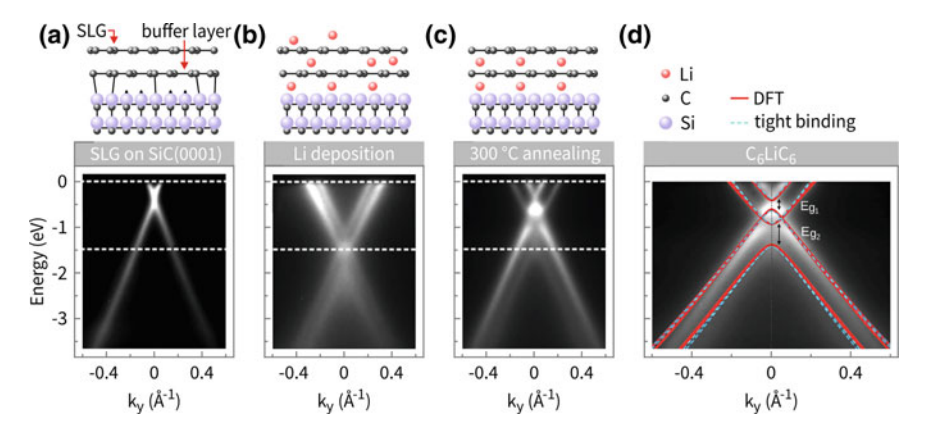


Fig. 4.11 Band dispersion of Li-intercalated graphene on 4H-SiC(0001). False color plots of the experimental ARPES spectral intensity recorded along a line perpendicular to the M-K direction, centered at the K-point. The Fermi energy  $\epsilon_F$  is at 0 eV. a Single layer graphene (SLG) before Li deposition, b after Li deposition, and c after heating to 300 °C. d Band structure of free-standing C<sub>6</sub>LiC<sub>6</sub> calculated with DFT (red solid lines) and using a tight-binding model (blue dashed lines), compared to the experimental ARPES spectral intensity as in (c).  $E_{\rm g1}$  and  $E_{\rm g2}$  energy gaps of different magnitude. Shown above are schematic side views of the topmost atomic layers of the studied sample. Adapted with permission from Ref. [27]. Copyright 2016 by the American Physical Society

applied to the backgate of our sample, we map the sheet resistivity  $\rho_{xx}$  between 0 and 12 T in a small density interval around  $n'=2.543\cdot 10^{14}$  cm<sup>-2</sup>. We determine n using the areal capacitance of 11.5 nF · cm<sup>-2</sup> (given by the thickness of the SiO<sub>2</sub> gate dielectric) according to Eq. 2.13. Plotted is the change in sheet resistivity  $\Delta \rho_{xx}$  obtained after subtracting the mean resistivity value at each value of B. As indicated by the dashed lines in the figure, the position in density of the SdH maxima extrapolate to approximately  $2.3 \cdot 10^{14}$  cm<sup>-2</sup> at B=0 T. This density relates to an onset of the higher energy subband at  $\epsilon_{\text{HES},0} \approx 1.63$  eV.

These findings point to a failure of the rigid band model, as the experimental evidence seems to suggest a dispersion of electronic states in this highly lithiated bilayer graphene sample as shown in the right panel of Fig. 4.10b. For the sake of comparison, the case of pristine bilayer graphene is shown in the left panel of the same figure. The difference is striking, and the scenario on the right hardly realistic. Efetov et al. [26] report an increase in the onset energy of the higher energy subband  $\epsilon_{\rm HES,0}$  at high eletrolyte gate voltages applied to bilayer graphene. Their experimentally accessible electron density was however limited to below  $n \approx 4.6 \cdot 10^{13} \ {\rm cm}^{-2}$ . Furthermore, the reported increase in  $\epsilon_{\rm HES,0}$  could be attributed to an increase in the interlayer potential difference, a natural consequence of the asymmetric charge injection when using an electrolyte top-gate. In the present case of Li intercalation we can expect the charge to be more evenly distributed between both layers, as supported from our Raman spectroscopy studies (see Sect. 4.2).

An alternative explanation for the observed magnetotransport behavior could lie in a significant modification of the band structure induced from intercalation.

A technique suitable to reveal such modifications is angle-resolved photoemission electron spectroscopy (ARPES). It has been applied to study Li-intercalation in graphene grown on 4H-SiC(0001) [27–32]. Experimental results from Ref. [27] are shown in Fig. 4.11. We also include schematic side views of the topmost atomic layers of the studied sample. Caffrey et al. [27] first sublimated Si from a 4H-SiC(0001) wafer, such that two graphene layers remain on its surface. As the lower one, the socalled buffer layer, is partially bound to the SiC substrate, only the upper one shows electronic states near the Fermi energy  $\epsilon_F = 0$  in Fig. 4.11a. Characteristically, a single, linearly dispersing band is observed with the Dirac point at  $\approx -0.45$  eV due to intrinsic n-doping from the substrate. With Li deposited at room temperature, ARPES reveals two bands with charge neutrality at  $\approx -1.4 \,\mathrm{eV}$  (Fig. 4.11b). This observation is attributed to bilayer graphene decoupled from the substrate due to Li intercalation in between the buffer layer and the SiC surface. The bilayer is highly electron doped due to charge transfer from Li additionally sitting on its top and in between its two carbon layers. After heating to 300°C, the bands in the ARPES signal have sharpened and show a distinct dispersion (Fig. 4.11c). The authors claim that while Li has disappeared from the surface, its intercalation to the interface has completed and it has developed an ordered structure in between the graphene layers. Meanwhile, the latter have changed register and are now AA-stacked, i.e., all their carbon atoms sit on top of each other. According to Fig. 4.11d, the measured dispersion resembles the one of C<sub>6</sub>LiC<sub>6</sub>, calculated both from density functional theory (DFT) as well as from a tight binding model. Qualitatively, the system appears as a highly electron-doped AA-stacked graphene bilayer, featuring two Dirac cones shifted in energy. However, due to the characteristic Li  $(\sqrt{3} \times \sqrt{3})R30^{\circ}$  superlattice, the Dirac cones are found to be unequally gapped as highlighted in Fig. 4.11d. The authors had to shift their calculated band dispersions in order to account for a displacement of the charge neutrality point to  $\approx -0.6$  eV after heating. They suggest that n-doping of the bilayer decreases as Li preferentially moves to the SiC interface with the majority of charge transferred to the substrate. This is in contradiction to the expected charge neutrality point of  $C_6LiC_6$  at  $\approx -1.4$  eV, according to both their calculation [27] and the one of Guzman et al. [33]. It might however suggest, that significant band modifications set in at already much lower Li content than in C<sub>6</sub>LiC<sub>6</sub>.

Therefore, the ARPES data in Fig. 4.11 does not yield a convincing explanation for the drastic difference in density between the two types of electrons that participate in the transport in our highly lithiated bilayer graphene device. The example demonstrates, however, that at such high Li content we might actually be facing a material with a strongly altered band dispersion. It is conceivable that the SdH oscillations observed in Fig. 4.9 stem from a new electron pocket, induced by Li intercalation via a strong modification of the band structure. More investigations are clearly needed to fully understand the observed magnetotransport. However, the existing results suggest a failure of the rigid band model, at least for this case of very high Li content.

#### 4.5 Summary

We investigated the reversible electrochemical lithiation/delithiation of bilayer graphene devices only partially covered from a Li-ion conducting polymer electrolyte. Several methods have revealed related and equally reversible changes induced to the electronic properties of bilayer graphene in situ, well outside the electrolyte-covered region of the devices. All observations are in agreement with the assumption that during lithiation Li-ions from the electrolyte intercalate into bilayer graphene and diffuse across the device, including its uncovered region. The charge transfer on the order of 1*e* per intercalating Li-ion to the electronic states of bilayer graphene manifests as

- a change in the sheet resistivity  $\rho_{xx}$  of bilayer graphene (Sect. 4.1). This is best revealed for an initially p-doped device, where  $\rho_{xx}$  characteristically passes through a maximum as the Fermi level  $\epsilon_F$  reversibly shifts through the charge neutrality point during lithiation/delithiation.
- a blueshift in energy  $\epsilon(G)$  of the Raman G band (Sect. 4.2) due to a stiffening of the associated  $E_{2g}$ -phonon mode.
- a change in the Hall resistance  $R_{xy}$  (Sect. 4.3). Since  $R_{xy}$  is directly related to the charge carrier density n (Eq. 4.2), it allows for a quantification of the Li density  $n_{\text{Li}}$  intercalated in bilayer graphene (Eq. 4.3). This is key to our analysis of the Li diffusion kinetics in Chap. 7.

The low-temperature magnetotransport of a device with the highest Li content achieved in this work was presented in Sect. 4.4. At  $n_{\rm Li}$  at least a third of the theoretical maximum, corresponding to a stoichiometry of  $C_{18}{\rm Li}C_{18}$ , signatures of multiband transport as well as indications for a failure of the rigid band model were observed.

#### References

- 1. Novoselov, K.S., et al.: Unconventional quantum Hall effect and Berry's phase of  $2\pi$  in bilayer graphene. Nat. Phys. **2**, 177–180 (2006)
- Enoki, T., Endo, M., Suzuki, M.: Graphite Intercalation Compounds and Applications. Oxford University Press, Oxford (2003)
- Dresselhaus, M.S., Dresselhaus, G.: Intercalation compounds of graphite. Adv. Phys. 30, 139– 326 (1981)
- 4. Bao, W., et al.: Approaching the limits of transparency and conductivity in graphitic materials through lithium intercalation. Nat. Commun. 5, 4224 (2014)
- Ferrari, A.C., et al.: Raman spectrum of graphene and graphene layers. Phys. Rev. Lett. 97, 187401 (2006)
- 6. Tuinstra, F., Koenig, J.L.: Raman spectrum of graphite. J. Chem. Phys. 53, 1126–1130 (1970)
- Zanini, M., Ching, L.-Y., Fischer, J.E.: Raman scattering in LiC<sub>6</sub>. Further evidence for a rigid-band-model interpretation. Phys. Rev. B 18, 2020–2022 (1978)
- 8. Eklund, P.C., Dresselhaus, G., Dresselhaus, M.S., Fischer, J.E.: Raman scattering in graphite-lithium intercalation compounds. Phys. Rev. B 21, 4705–4709 (1980)
- 9. Inaba, M., et al.: In situ Raman study on electrochemical Li intercalation into graphite. J. Electrochem. Soc. **142**, 20–26 (1995)

References 79

10. Huang, W., Frech, R.: In situ Raman studies of graphite surface structures during lithium electrochemical intercalation. J. Electrochem. Soc. **145**, 765–770 (1998)

- 11. Pollak, E., et al.: The interaction of Li<sup>+</sup> with single-layer and few-layer graphene. Nano Lett. **10**, 3386–3388 (2010)
- 12. Shi, Q., Dokko, K., Scherson, D.A.: In situ Raman microscopy of a single graphite microflake electrode in a Li<sup>+</sup>-containing electrolyte. J. Phys. Chem. B **108**, 4789–4793 (2004)
- Migge, S., Sandmann, G., Rahner, D., Dietz, H., Plieth, W.: Studying lithium intercalation into graphite particles via in situ Raman spectroscopy and confocal microscopy. J. Solid State Electrochem. 9, 132–137 (2005)
- Sole, C., Drewett, N.E., Hardwick, L.J.: In situ Raman study of lithium-ion intercalation into microcrystalline graphite. Faraday Discuss. 172, 223–237 (2014)
- Yan, J., Zhang, Y., Kim, P., Pinczuk, A.: Electric field effect tuning of electron-phonon coupling in graphene. Phys. Rev. Lett. 98, 166802 (2007)
- Pisana, S., et al.: Breakdown of the adiabatic Born-Oppenheimer approximation in graphene. Nat. Mater. 6, 198–201 (2007)
- 17. Das, A., et al.: Monitoring dopants by Raman scattering in an electrochemically top-gated graphene transistor. Nat. Nanotech. 3, 210–215 (2008)
- Zou, J., Sole, C., Drewett, N.E., Velický, M., Hardwick, L.J.: In situ study of Li intercalation into highly crystalline graphitic flakes of varying thicknesses. J. Phys. Chem. Lett. 7, 4291–4296 (2016)
- 19. Malard, L.M., Elias, D.C., Alves, E.S., Pimenta, M.A.: Observation of distinct electron-phonon couplings in gated bilayer graphene. Phys. Rev. Lett. **101**, 257401 (2008)
- Mafra, D.L., et al.: Characterizing intrinsic charges in top gated bilayer graphene device by Raman spectroscopy. Carbon 50, 3435–3439 (2012)
- 21. Yan, J., Henriksen, E.A., Kim, P., Pinczuk, A.: Observation of anomalous phonon softening in bilayer graphene. Phys. Rev. Lett. **101**, 136804 (2008)
- Das, A., et al.: Phonon renormalization in doped bilayer graphene. Phys. Rev. B 79, 155417 (2009)
- Kim, Y.D., et al.: Focused-laser-enabled p-n junctions in graphene field-effect transistors. ACS Nano 7, 5850–5857 (2013)
- 24. Ando, T.: Anomaly of optical phonons in bilayer graphene. J. Phys. Soc. Jpn. 76, 104711 (2007)
- 25. Ashcroft, N.W., Mermin, N.D.: Solid State Physics. Brooks/Cole (1976)
- Efetov, D.K., Maher, P., Glinskis, S., Kim, P.: Multiband transport in bilayer graphene at high carrier densities. Phys. Rev. B 84, 161412 (2011)
- 27. Caffrey, N.M., et al.: Structural and electronic properties of Li-intercalated graphene on SiC(0001). Phys. Rev. B 93, 195421 (2016)
- 28. Virojanadara, C., Watcharinyanon, S., Zakharov, A.A., Johansson, L.I.: Epitaxial graphene on 6*H*-SiC and Li intercalation. Phys. Rev. B **82**, 205402 (2010)
- Virojanadara, C., Zakharov, A.A., Watcharinyanon, S., Yakimova, R., Johansson, L.I.: A low-energy electron microscopy and x-ray photo-emission electron microscopy study of Li intercalated into graphene on SiC(0001). New J. Phys. 12, 125015 (2010)
- Sugawara, K., Kanetani, K., Sato, T., Takahashi, T.: Fabrication of Li-intercalated bilayer graphene. AIP Adv. 1, 022103 (2011)
- 31. Watcharinyanon, S., Johansson, L.I., Zakharov, A.A., Virojanadara, C.: Studies of Li intercalation of hydrogenated graphene on SiC(0001). Surf. Sci. 606, 401–406 (2012)
- 32. Bisti, F., et al.: Electronic and geometric structure of graphene/SiC(0001) decoupled by lithium intercalation. Phys. Rev. B **91**, 245411 (2015)
- 33. Guzman, D.M., Alyahyaei, H.M., Jishi, R.A.: Superconductivity in graphene-lithium. 2D Mater. 1, 021005 (2014)

# **Chapter 5 Conductivity Corrections from Quantum Interferences**



In this chapter we exploit quantum interference (QI) corrections to the Drude conductivity in bilayer graphene devices as a sensitive probe to the presence of intercalated Li-ions. In Sect. 5.1, we first provide in-depth information on QIs in single layer graphene and bilayer graphene, including the theoretical framework and the mathematical description. We then present experimental data in Sect. 5.2, obtained from low-field magnetotransport measurements of two bilayer graphene devices at different states of lithiation.

### 5.1 Quantum Interferences in Graphene Single- and Bilayers

As already introduced in Sect. 2.7.3, the diffusive motion of charge carriers in a disordered 2D crystal is affected by interferences of the probability amplitudes associated with different paths of propagation. Fig. 5.1a illustrates this diffusive propagation as a series of straight segments, on which the motion is ballistic, interrupted by elastic scattering events (grey circles), during which the particle might change its direction. As long as phase coherence—characterized by the phase coherence length  $l_{\phi}$  or the phase coherence time  $\tau_{\phi}$ —is maintained, the probability amplitudes for travelling between any two points (such as A and B in the figure) interfere and may induce corrections to the overall conductivity. It has been shown, however, that the multitude of possible trajectories between two arbitrary but distinct points lead to an averaging-out of the effect [1]. The only ones effective in inducing observable QI corrections are closed, counter-propagating paths, returning to the point of departure of a charge carrier (red and blue lines, (ii) and (iii), in Fig. 5.1a). If the interference between such paths is constructive, i.e., the probability to return to the origin is enhanced, one speaks of weak localization (WL). On the other hand, if the interference is destructive, i.e., the probability to return to the origin is reduced, one speaks of weak anti-localization (WAL). A result is an increase (decrease) in the resistivity

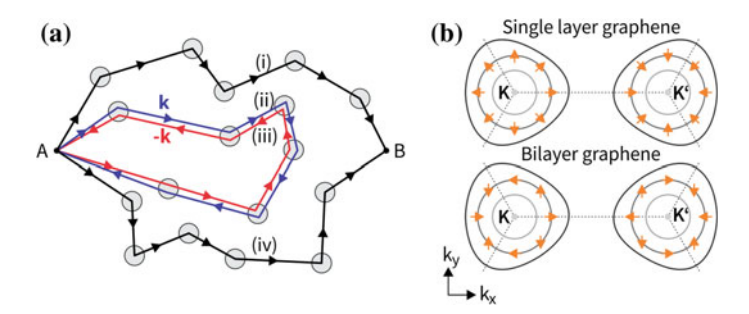


**Fig. 5.1** a Arbitrary classical paths of diffusive motion of charge carriers in 2D from point A to B (i, iv) or returning to A (ii, iii). Grey circles represent elastic scattering events. **b** Schematic of the Fermi line from low (light grey) to high (dark grey) charge carrier density for single layer graphene (top) and bilayer graphene (bottom), respectively. The **k**-dependent orientation of the pseudo spin (orange arrows), drawn for a single Fermi line, indicates the different degree of chirality of charge carriers in both systems

of the sample in the case of WL (WAL), usually on the order of only a few percent of the Drude value  $\rho$ . This QI correction to  $\rho$  can be revealed via the application of a magnetic field oriented perpendicular to the 2D sample plane (see Sect. 2.7.3), which breaks time-reversal symmetry and thus suppresses the interference between the associated probability amplitudes.

The character (and possible result) of these QIs depends on both the material's structure (crystal and electronic) as well as the type of disorder present. In conventional 2DESs, characterized by a single valley of charge carriers and no spin-momentum locking, typically WL is observed. In these systems, spin-orbit interaction (SOI) was classically considered key to inducing WAL, as it enables spin-flips during charge carrier scattering events [2]. In grahene single and bilayers, the situation is more complex due to the chirality of the charge carriers associated with a different Berry phase  $\Phi_B$  in both systems. According to Ando et al. [3],  $\Phi_B$ determines whether back scattering is suppressed or enhanced, i.e, whether WL or WAL occurs. In the case of single layer graphene with  $\Phi_B = \pi$ , one may thus expect WAL, while in bilayer graphene with  $\Phi_B = 2\pi$  WL should prevail. As illustrated in Fig. 5.1b however, charge carriers in both systems live in two inequivalent valleys near  $K^{(i)}$ , elastic scattering between which tends to restore WL also in single layer graphene. Further effects such as trigonal warping of the Fermi line and chiralitybreaking intravalley scattering processes also need to be considered in a complete description, which we will briefly introduce in the following first for single layer graphene and then for bilayer graphene.

<sup>&</sup>lt;sup>1</sup>Note that in the case of equivalent valleys, QI corrections to the conductivity in multivalley systems are usually formulated as the sum of the contributions from each valley weighted with a prefactor [2, 4, 5].

#### 5.1.1 Quantum Interferences in Single Layer Graphene

In single layer graphene, the QI corrections to the conductivity can be written as [6]

$$\Delta\sigma(B) = \frac{e^2}{\pi h} \left[ F\left(\frac{B}{B_{\phi}}\right) - F\left(\frac{B}{B_{\phi} + 2B_i}\right) - 2F\left(\frac{B}{B_{\phi} + B_i + B_*}\right) \right]$$
 (5.1)

with

$$F(z) = \ln(z) + \Psi\left(\frac{1}{2} + \frac{1}{z}\right) \quad \text{and} \quad B_{\phi,i,*} = \frac{\hbar}{4e} \cdot \frac{1}{l_{\phi,i,*}^2} = \frac{\hbar}{4e} \cdot \frac{1}{D\tau_{\phi,i,*}}.$$

Here,  $\Psi(x)$  is the digamma function and  $l_i$ ,  $l_*$  are two length scales, the first of which characterizes elastic scattering between the two valleys at  $K^{(\prime)}$ , and the second of which is associated with breaking of the effective time-reversal symmetry in a single valley due to trigonal warping of the Fermi surface and chirality breaking intravalley scattering events. The latter are mediated by long-range potentials, primarily caused by random strain fluctuations in graphene that effectively couple to the charge carriers via associated pseudomagnetic fields [7, 8]. Long-range potentials from charged impurities may be an additional cause of chirality breaking intravalley scattering [8]. The corresponding time scales  $\tau_i$ ,  $\tau_*$  follow from the charge carrier diffusion coefficient  $D=v_F^2 au_{\rm tr}/2$  as  $l_{\phi,i,*}=\sqrt{D au_{\phi,i,*}}$ , where  $au_{\rm tr}$  is the elastic mean free time. As can be seen from Eq. 5.1,  $\Delta \sigma(B)$  can be of either positive or negative sign, depending on the magnitude of the different scattering rates. In the limit of negligible rates  $\tau_i^{-1}$ ,  $\tau_*^{-1} \to 0$  (i.e.,  $B_i$ ,  $B_* \to 0$ ), only the last term of Eq. 5.1 remains as the first two cancel and we find WAL as  $\Delta \sigma(B) < 0$ . This intrinsic WAL is qualitatively maintained at a finite value of  $\tau_*^{-1}$ , as long as there is no intervalley scattering [9, 10], although quantitatively  $\tau_*^{-1}$  tends to suppress interference effects. Intervalley scattering at the rate  $\tau_i^{-1}$ , induced by potentials with extremely short interaction range (such as caused from a lattice vacancy), tends to restore WL [6, 9].

While QI corrections to the conductivity have first been reported to be strongly suppressed [12], it is WL which most readily manifests in single layer graphene [8, 11–16]. This is because, while commonly  $\tau_*^{-1}$  is found to be by far the largest rate on the order of  $\tau_{\rm tr}^{-1}$  [8, 15], the intervalley scattering rate  $\tau_i^{-1}$  is still significant. This finding was expected from the coupling between graphene and a substrate, causing atomically sharp scatterers [6]. WAL could however also be demonstrated in turbostratically disordered epitaxial graphene [17], followed by the demonstration of the transition between WL and WAL in exfoliated single layers on SiO<sub>2</sub> [11], see Fig. 5.2. The latter was achieved by lowering the carrier density n (thereby increasing  $\tau_i$ ) and by raising the temperature T (thereby decreasing  $\tau_\phi$ ). While WAL has been repeatedly observed [18, 19], the majority of experimental works on single layer graphene report WL. Typically, the rates  $\tau_i^{-1}$ ,  $\tau_*^{-1}$  are found to be independent of temperature T [8, 11].

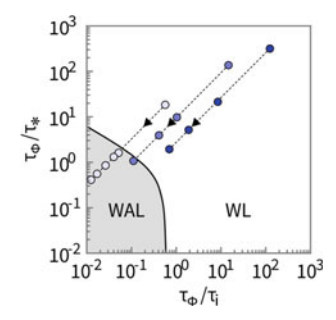


Fig. 5.2 Quantum interferences (QIs) in single layer graphene: manifestation of WL or WAL depending on characteristic time scales. Black arrows point towards increasing temperature. Data points are given for three different electron densities n, with more saturated blue representing a higher value of n. Adapted with permission from Ref. [11]. Copyright 2009 by the American Physical Society

#### 5.1.2 Quantum Interferences in Bilayer Graphene

The phenomenology of QIs in bilayer graphene inherits many aspects from the case of single layer graphene. The main difference is the intrinsic Berry phase  $\Phi_B = 2\pi$  of charge carriers [20, 21], which accounts for the constructive interference of counter-propagating charge carrier paths. WL is thus always observed [22], and its contribution  $\Delta \sigma$  to the magnetoconductivity in bilayer graphene can be described as [23]

$$\Delta\sigma(B) = \frac{e^2}{\pi h} \left[ F\left(\frac{B}{B_{\phi}}\right) - F\left(\frac{B}{B_{\phi} + 2B_i}\right) + 2F\left(\frac{B}{B_{\phi} + B_i + B_*}\right) \right]. \tag{5.2}$$

In contrast to the case of single layer graphene (Eq. 5.1) the last term has a positive sign.<sup>2</sup> The result of Eq. 5.2 is always positive, and in the case of  $\tau_i^{-1}$ ,  $\tau_*^{-1} \to 0$  the remaining third term corresponds to the conventional scenario of WL in a 2D systems with two independent valleys. A finite value of  $\tau_*^{-1}$  again tends to suppress the QI correction altogether. Intervalley scattering at the rate  $\tau_i^{-1}$ , however, induces a difference between the first two terms, thereby restoring and stabilizing the WL effect.

Several experimental works reported WL in bilayer graphene, with Eq. 5.2 confirmed to well describe this phenomenon [22, 25, 26]. As in single layer graphene,  $\tau_*$  is typically found to be the shortest time scale, at least one order of magnitude smaller than  $\tau_{\phi}$ ,  $\tau_i$  and approaching the elastic mean free time  $\tau_{\text{tr}}$ . Pseudomagnetic

<sup>&</sup>lt;sup>2</sup>Another difference lies in the precise expression of  $\tau_*$ , qualitatively characterizing the same effective time-reversal symmetry breaking within a single valley as in single layer graphene, differing however in details related to the different crystal structure and scattering pathways. The interested reader is referred to Ref. [24].

fields induced by random strain fluctuations have likewise been identified as the most probable source of intravalley scattering processes contributing to  $\tau_*$  and limiting the mobility in bilayer graphene devices [26].

#### 5.2 Weak Localization in Li-intercalated Bilayer Graphene

To reveal QI corrections to the magnetoconductivity in bilayer graphene, we perform magnetotransport measurements of bilayer graphene devices such as the one shown in Fig. 5.3a. As discussed in the preceding chapter, the gate voltage  $U_G$ between bilayer graphene (working electrode, WE) and the Li counter electrode (CE) is controlled at all times using a high-input impedance precision source/measure unit. Lithium intercalation (deintercalation) is driven at  $U_G = 0.05 \,\mathrm{V}$  versus Li/Li<sup>+</sup>  $(U_G = 1.5 \text{ V versus Li/Li}^+)$ , respectively, with the sample kept at room temperature in a high vacuum atmosphere,  $p \le 1 \cdot 10^{-6}$  mbar. In the case of the sample shown in Fig. 5.3a, Li intercalates first into a thick graphene multilayer (bright area at the left in the optical micrograph) and then diffuses into the bilayer graphene region of the flake, well separated from the interface with the polymer electrolyte. We study the magnetotransport of charge carriers in the bilayer graphene device, using two Ti contacts to impose an ac-excitation current with a rms-amplitude  $I \le 1 \,\mu\text{A}$  at a frequency of  $\sim 13.33$  Hz. We simultaneously measure both the longitudinal and transverse voltage drops across the device using standard lock-in techniques in fourprobe configuration in order to extract the longitudinal conductivity  $\sigma(B)$  in the three regions of the device indicated in Fig. 5.3a. The WL contribution to the conductivity  $\Delta \sigma(B)$  is readily distinguished at low temperatures via its suppression by a small magnetic field oriented perpendicular to the bilayer graphene planes. We conduct all experiments in a cryogen-free superconducting magnet system providing magnetic fields B up to 12 T and temperatures between 1.4 K and 300 K.

In the left panel of Fig. 5.3b, we show three traces of the normalized change in magnetoconductivity,  $[\sigma(B) - \sigma_0]/\sigma_0$ , measured in region 2 of the bilayer graphene device shown in Fig. 5.3a. Data is shown for three different temperatures and with an intercalated Li density  $n_{\text{Li}} \approx 3.5 \cdot 10^{13} \, \text{cm}^{-2}$  (determined from Hall measurements according to the procedure discussed in Sect. 4.3). A  $\sim 3 \, \%$  positive magnetoconductivity contribution from WL is observable at 1.5 K. It gets gradually suppressed as the temperature increases. This suppression is due to dephasing, the temperature-dependence of which yields insights into mechanisms efficient in causing it as we will discuss in Sect. 5.2.1. Superposed to the WL contribution  $\Delta \sigma(B)$  and equally getting suppressed with increasing temperature are universal conductance fluctuations (UCFs). They are strongest at lowest temperatures as can be seen in the figure. As the magnitude of UCFs measured in our samples is usually smaller than the WL contribution, we refrain from averaging techniques targeting their removal during

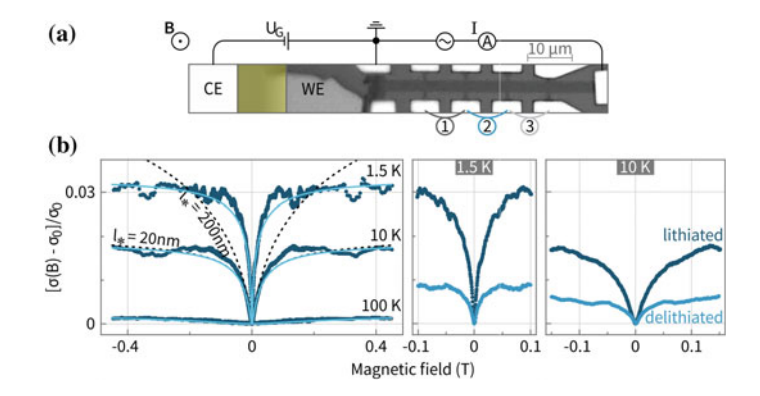


Fig. 5.3 Weak localization (WL) in the bilayer graphene device #1 for different states of lithiation. a Schematic bilayer graphene (working electrode, WE)|polymer electrolyte|Li (counter electrode, CE) cell used for Li intercalation including an optical micrograph of the device with several Ti contacts for magnetotransport measurements. Contact pairs used to extract the longitudinal magnetoconductivity of three different sections  $i = \{1, 2, 3\}$  of the device are indicated. b Exemplary magnetoconductivity traces for bilayer graphene in the lithiated (dark cyan dots,  $n_{\text{Li}} = 3.5 \cdot 10^{13} \, \text{cm}^{-2}$ ) and the delithiated state (bright cyan dots) at different temperatures, measured in section 2. Solid lines are fits to the data using the first two terms of Eq. 5.2, only. Black, dashed lines are plots of Eq. 5.2 with parameters as for the simplified fit at 10 K and two values for  $l_*$  as indicated

the data acquisition process,<sup>3</sup> except noted otherwise. Most importantly, we see a clear enhancement of the WL effect upon lithiation. This is demonstrated in the two panels on the right of Fig. 5.3b, where we show low-field magnetoconductivity traces measured in section 2 of the lithiated device at 1.5 K and 10 K as well as data obtained after delithiation. We will show below that the significant enhancement of the WL effect in the presence of intercalated Li is due to an increased elastic scattering rate  $\tau_i^{-1}$  of charge carriers between the two valleys at  $\textbf{\textit{K}}$  and  $\textbf{\textit{K}}'$ .

Successful fits to the WL data from our bilayer graphene devices are typically obtained using only the first two terms in Eq. 5.2, as  $l_*$  is by far the shortest length scale, in line with previous measurements on bilayer graphene [22, 26]. The good agreement between the two term model and our measurement is demonstrated in the left panel of Fig. 5.3b (solid lines and dots, respectively). For the data measured at 10 K, we additionally plot two traces for the full model for two selected values of  $l_*$  (20 nm and 200 nm). The third term of Eq. 5.2 can indeed be neglected and  $l_*$  is on the order of the transport mean free path,  $l_{\rm tr} = v_F \tau_{\rm tr} \approx 26$  nm, essentially set by the scale of the electron-hole puddles.

In Fig. 5.4 we plot the temperature dependence of the characteristic length scales (the phase coherence length  $l_{\phi}$  and the length associated with intervalley scattering  $l_i$ ) obtained in this manner in addition to the mean free path  $l_{\rm tr}$ . The latter is obtained from  $l_{\rm tr} = v_F \tau_{\rm tr}$ , with the transport time  $\tau_{\rm tr} = \sigma_0 m^*/(ne^2)$  extracted from the zero field

 $<sup>^{3}</sup>$ In order to suppress UCFs, one may vary the backgate voltage and thus the carrier density within a small interval at a given value of B, thereby averaging-out the UCFs [22].

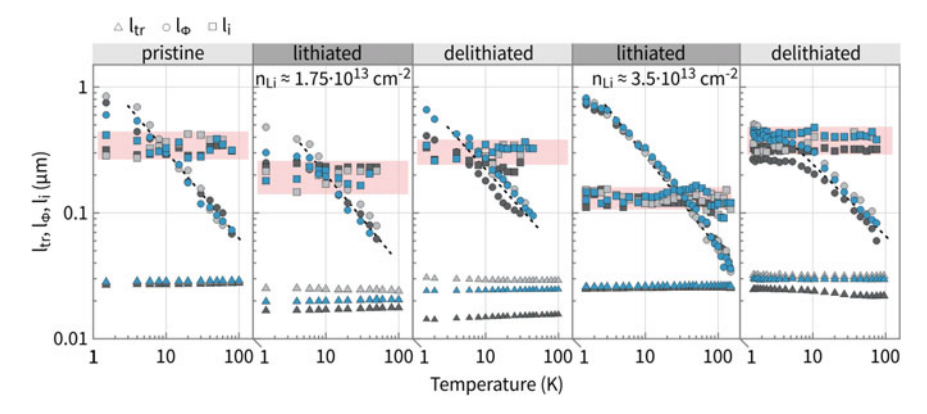


Fig. 5.4 Temperature dependence of the elastic mean free path  $l_{tr}$  (triangles), the phase coherence length  $l_{\phi}$  (circles), and the intervalley scattering length  $l_{i}$  (squares) in sample #1 at different states of lithiation. The three different colors of the data correspond to the three sections of the device, as shown in Fig. 5.3a. Dashed lines are guides to the eye for the temperature dependence of  $l_{\phi}$ , while red shaded areas indicate the approximate spread of  $l_{i}$ 

conductivity  $\sigma_0 \approx \sigma(B=0,T) - \Delta\sigma(B,T)$  without quantum corrections. Both the Fermi velocity  $v_F$  and the effective mass  $m^*$  depend on the charge carrier density n (which we extract from a Hall measurement) and are calculated according to Eqs. 2.6 and 2.5, respectively, using the simple tight-binding model of bilayer graphene's electronic structure, Eq. 2.3. In Fig. 5.4, we plot data obtained from all three sections of the device shown in Fig. 5.3a, using the respective color. In all cases we confirm that  $k_F l_{\rm tr} \gg 1$  (with the Fermi wavevector  $k_F$ ), i.e., charge carrier transport is in the diffusive metallic, weakly disordered regime and Eq. 5.2 applies.

While both  $l_i$  and  $l_{\rm tr}$  show no clear temperature dependence,  $l_\phi$  drops with increasing temperature as dephasing mechanisms gain efficiency, thereby suppressing interference effects. Qualitatively, dephasing appears insensitive to the concentration of intercalated Li. A clear sensitivity to Li intercalation is revealed by a change in the characteristic intervalley scattering length  $l_i$ . As can be seen in Fig. 5.4,  $l_i$  is significantly reduced in the presence of intercalated Li, i.e., the intervalley scattering rate  $\tau_i^{-1}$  is enhanced. Measurements performed on a different sample agree with this general observation, see Fig. 5.5. Here, the first Li intercalation resulted in an unequal  $n_{\rm Li}$  measured in section 1 and 2 of the device shown in Fig. 5.5a. Therefore, we plot the data in Fig. 5.5b in two separate rows. In Fig. 5.6 we have extracted the intervalley scattering time  $\tau_i$  as well as the dephasing time  $\tau_\phi$ , using  $\tau_{\phi,i} = l_{\phi,i}^2 D$ , with the charge carrier diffusion coefficient  $D = v_F^2 \tau_{\rm tr}/2$ . We use the maximum spread in values obtained for  $l_i$  from fitting at temperatures between 1.5 K and 10 K to determine the error bars displayed in the plots. For comparison, we again include the transport times  $\tau_{\rm tr}$ .

While  $\tau_{tr}$  varies from sample to sample (depending on quality and residual doping) and shows no conclusive dependence on the state of lithiation,  $\tau_i$  is reproducibly reduced upon Li intercalation and increased upon Li-deintercalation, revealing the

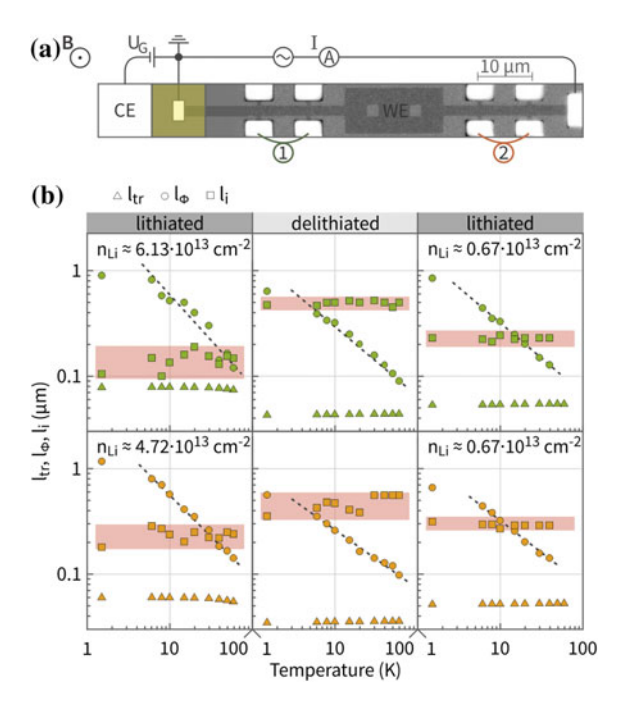
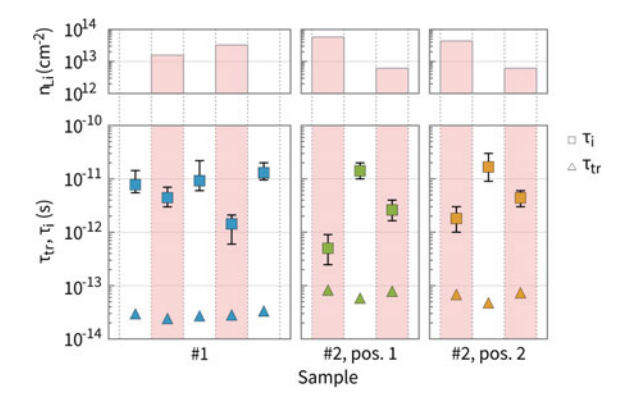


Fig. 5.5 Weak localization (WL) in the bilayer graphene device #2 for different states of lithiation. a Schematic bilayer graphene (working electrode, WE)|polymer electrolyte|Li (counter electrode, CE) cell used for Li intercalation including an optical micrograph of the device with several Ti contacts for magnetotransport measurements. Contact pairs used to extract the longitudinal magnetoconductivity of two different sections  $i=\{1,2\}$  of the device are indicated. b Temperature dependence of the elastic mean free path  $l_{tr}$  (triangles), the phase coherence length  $l_{\phi}$  (circles), and the intervalley scattering length  $l_i$  (squares) in sample #2 at different states of lithiation. The two different colors of the data correspond to the two sections of the device, as shown in (a). Dashed lines are guides to the eye for the temperature dependence of  $l_{\phi}$ , while red shaded areas indicate the approximate spread of  $l_i$ 

Fig. 5.6 Intervalley scattering time (squares) and transport time (triangles) for sample #1 and two different contact pairs of sample #2. Columns are successive states of lithiation with the density  $n_{\rm Li}$  of intercalated Li shown in the column chart (top). White columns are pristine or delithiated states



degree of reversibility of the intercalation process. Their size being shorter than the lattice spacing, Li-ions enable the large momentum transfer required for elastic intervalley scattering. Upon insertion, they assists in scattering charge carriers between the two valleys in bilayer graphene, not unlike what has been reported for indium adatoms on single layer graphene [27].

#### 5.2.1 Dephasing

As temperature increases, charge carriers in graphene maintain their phase coherence over decreasing lengths because inelastic scattering becomes more important. The temperature dependence of the dephasing rate  $\tau_{\phi}^{-1}$  bears information about the dephasing mechanisms involved. It is described as the sum of individual contributions, the most relevant of which can be expressed as [11, 25, 26, 28]<sup>4</sup>

$$\tau_{\phi}^{-1} = \tau_{N}^{-1} + \tau_{ee}^{-1} \tag{5.3}$$

$$=k_B T \frac{\ln(g/2)}{\hbar g} + \beta^2 \cdot \frac{\pi (k_B T)^2}{4\hbar \epsilon_F} \ln\left(\frac{2\epsilon_F}{k_B T}\right),\tag{5.4}$$

with the dimensionless conductivity  $g = \sigma/(e^2/h)$ , the Boltzmann constant  $k_B$ , and a coefficient  $\beta$  on the order of unity. Here,  $\tau_N^{-1}$  describes Nyquist scattering, i.e., small momentum transfer, electron-electron scattering in the diffusive regime.  $\tau_{ee}^{-1}$  describes electron-electron scattering in the ballistic regime due to the direct Coulomb interaction (large momentum transfer collision).  $\tau_{ee}^{-1}$  was demonstrated to be important at temperatures  $T \gtrsim 20 \, \mathrm{K}$  [16].

In Fig. 5.7a, we show a typical plot of the temperature dependence of  $\tau_\phi^{-1}$  used for the analysis according to Eq. 5.4. Here, grey dots are experimental data points from section 1 of sample #1 (Fig. 5.3a) in the lithiated state with  $n_{\rm Li}=3.5\cdot10^{13}~{\rm cm}^{-2}$ . The solid line is the fit to the data using Eq. 5.4 and  $\beta=1.79$ . The individual contributions from  $\tau_N^{-1}$  and  $\tau_{ee}^{-1}$  are plotted as the long-dashed and short-dashed line, respectively. While indeed  $\tau_N^{-1}$  dominates in the low-temperature range,  $\tau_{ee}^{-1}$  is the more important contribution at high temperatures. A combined linear and quadratic T-dependence as the one shown in Fig. 5.7a is consistently observed in all our bilayer graphene devices, irrespective of the state of lithiation. This finding agrees with reported experiments on single layer graphene [11, 16].

While we observe no clear quantitative dependence of dephasing on  $n_{\rm Li}$ , we do see a dependence on the charge carrier concentration n. In Figs. 5.7b and c we therefore plot results from fitting Eq. 5.4 to the experimental data obtained from devices #1 and #2 as a function of n, negative (positive) values of which stand for holes (electrons). In Fig. 5.7b it can be seen that Nyquist scattering is strongest near charge neutrality

<sup>&</sup>lt;sup>4</sup>Here, we omit a constant contribution due to spin-flip scattering, first claimed experimentally by Lara-Avila et al. [29]

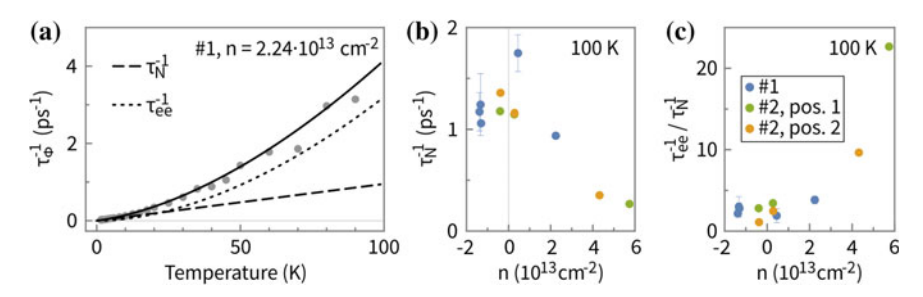


Fig. 5.7 Dephasing in bilayer graphene devices. a Temperature dependence of the rate  $\tau_{\phi}^{-1}$  of inelastic, phase coherence breaking scattering events. Experimental data (grey dots) for section 1 of sample #1 (Fig. 5.3a) in the lithiated state with  $n_{\text{Li}} = 3.5 \cdot 10^{13} \, \text{cm}^{-2}$ . The solid line is the fit to the data using Eq. 5.4 for  $\beta = 1.79$ , with contributions  $\tau_{N}^{-1}$  (long-dashed line) and  $\tau_{ee}^{-1}$  (short-dashed line). The net n-doping given in the figure is lower than  $n_{\text{Li}}$  due to initial p-doping of the device. b Magnitude of the contribution of Nyquist scattering  $\tau_{N}^{-1}$  to  $\tau_{\phi}^{-1}$  at 100 K. c Ratio of scattering rates  $\tau_{ee}^{-1}/\tau_{N}^{-1}$  at 100 K. The colors in b, c correspond to the bilayer graphene devices illustrated in Figs. 5.3a and 5.5a. For sample #1 we plot mean values of the three sections and error bars (standard deviation)

and decreases in rate at higher values of n. For the sake of comparison we show data at an arbitrarily chosen temperature of  $T=100\,\mathrm{K}$ . In single layer graphene, such an increased Nyquist scattering near charge neutrality was attributed to spatially fluctuating electromagnetic fields associated with the electron-hole puddles [16]. The same scenario might apply to our bilayer graphene samples which indeed feature electron-hole puddles (see Sect. 2.5). A comparison of the two terms in Eq. 5.4 reveals furthermore that the direct Coulomb interaction gets more important as n increases. This is illustrated in Fig. 5.7c, where we plot the ratio  $\tau_{ee}^{-1}/\tau_N^{-1}$  again at  $100\,\mathrm{K}$ . A similarly increased importance of  $\tau_{ee}^{-1}$  at high carrier density has been reported from experiments on single layer graphene [11, 16].

#### 5.3 Summary

Quantum interference (QI) corrections to the conductivity of bilayer graphene manifest as weak localization (WL), readily evidenced by its suppression via the application of a small out-of-plane magnetic field. As the charge carriers in bilayer graphene are chiral and additionally live in two valleys, the WL effect is determined by several time scales characterizing the phase-coherent charge carrier transport: the phase coherence time  $\tau_{\phi}$ , the effective intravalley chiral symmetry breaking time  $\tau_{*}$ , and the elastic intervalley scattering time  $\tau_{i}$ . In agreement with experiments on single layer graphene [11, 16], we find  $\tau_{\phi}$  to be limited by direct Coulomb interaction-induced electron-electron scattering events at higher values of the charge carrier density n and/or at higher temperatures T.  $\tau_{*}$  proves to be the shortest time scale on the order of the transport time  $\tau_{tr}$ , identifying long-range disorder potentials most likely

5.3 Summary 91

associated with random strain fluctuations as the dominant source of charge carrier scattering in our devices [8, 26]. Most importantly, however, we demonstrate WL as a powerful probe to the presence of Li-ions intercalated in bilayer graphene, as their atomic-scale perturbation to the system selectively enhances the intervalley scattering rate  $\tau_i^{-1}$ . After delithiation,  $\tau_i^{-1}$  has dropped back towards its original value. Our systematic study of WL using several contact pairs on two bilayer graphene devices thus strikingly confirms Li-ion diffusion from the electrolyte at the device periphery into and out of the uncovered bilayer graphene.

#### References

- Beenakker, C.W.J., van Houten, H.: Quantum transport in semiconductor nanostructures. In: Ehrenreich, H., Turnbull, D. (eds.) Semiconductor Heterostructures and Nanostructures. Solid State Physics, vol. 44, pp. 1–228. Academic Press, Inc., San Diego, USA (1991)
- 2. Al'tshuler, B.L., Aronov, A.G., Larkin, A.I., Khmel'nitskii, D.E.: Anomalous magnetoresistance in semiconductors. J. Exp. Theor. Phys. **54**, 411–419 (1981)
- 3. Ando, T., Nakanishi, T., Saito, R.: Berry's phase and absence of back scattering in carbon nanotubes. J. Phys. Soc. Jpn. 67, 2857–2862 (1998)
- Fukuyama, H.: Non-metallic behaviors of two-dimensional metals and effect of intervalley impurity scattering. Prog. Theor. Phys. Suppl. 69, 220–231 (1980)
- Kawabata, A.: Theory of negative magnetoresistance I. Application to heavily doped semiconductors. J. Phys. Soc. Jpn. 49, 628–637 (1980)
- McCann, E., et al.: Weak-localization magnetoresistance and valley symmetry in graphene. Phys. Rev. Lett. 97, 146805 (2006)
- Morpurgo, A.F., Guinea, F.: Intervalley scattering, long-range disorder, and effective timereversal symmetry breaking in graphene. Phys. Rev. Lett. 97, 196804 (2006)
- 8. Couto, N.J.G., et al.: Random strain fluctuations as dominant disorder source for high-quality on-substrate graphene devices. Phys. Rev. X 4, 041019 (2014)
- Ando, T., Nakanishi, T.: Impurity scattering in carbon nanotubes—absence of back scattering. J. Phys. Soc. Jpn. 67, 1704–1713 (1998)
- Suzuura, H., Ando, T.: Crossover from symplectic to orthogonal class in a two-dimensional honeycomb lattice. Phys. Rev. Lett. 89, 266603 (2002)
- 11. Tikhonenko, F.V., Kozikov, A.A., Savchenko, A.K., Gorbachev, R.V.: Transition between electron localization and antilocalization in graphene. Phys. Rev. Lett. **103**, 226801 (2009)
- Morozov, S.V., et al.: Strong suppression of weak localization in graphene. Phys. Rev. Lett. 97, 016801 (2006)
- Berger, C., et al.: Electronic confinement and coherence in patterned epitaxial graphene. Science 312, 1191–1196 (2006)
- 14. Heersche, H.B., Jarillo-Herrero, P., Oostinga, J.B., Vandersypen, L.M.K., Morpurgo, A.F.: Bipolar supercurrent in graphene. Nature **446**, 56–59 (2007)
- Tikhonenko, F.V., Horsell, D.W., Gorbachev, R.V., Savchenko, A.K.: Weak localization in graphene flakes. Phys. Rev. Lett. 100, 056802 (2008)
- Ki, D.-K., Jeong, D., Choi, J.-H., Lee, H.-J., Park, K.-S.: Inelastic scattering in a monolayer graphene sheet: a weak-localization study. Phys. Rev. B 78, 125409 (2008)
- 17. Wu, X., Li, X., Song, Z., Berger, C., de Heer, W.A.: Weak antilocalization in epitaxial graphene: Evidence for chiral electrons. Phys. Rev. Lett. **98**, 136801 (2007)
- 18. Jouault, B., et al.: Interplay between interferences and electron-electron interactions in epitaxial graphene. Phys. Rev. B 83, 195417 (2011)

- Gopinadhan, K., Shin, Y.J., Yudhistira, I., Niu, J., Yang, H.: Giant magnetoresistance in singlelayer graphene flakes with a gate-voltage-tunable weak antilocalization. Phys. Rev. B 88, 195429 (2013)
- 20. Novoselov, K.S., et al.: Unconventional quantum Hall effect and Berry's phase of  $2\pi$  in bilayer graphene. Nat. Phys. **2**, 177–180 (2006)
- McCann, E., Fal'ko, V.I.: Landau-level degeneracy and quantum Hall effect in a graphite bilayer. Phys. Rev. Lett. 96, 086805 (2006)
- 22. Gorbachev, R.V., Tikhonenko, F.V., Mayorov, A.S., Horsell, D.W., Savchenko, A.K.: Weak localization in bilayer graphene. Phys. Rev. Lett. 98, 176805 (2007)
- 23. Kechedzhi, K., Fal'ko, V.I., McCann, E., Altshuler, B.L.: Influence of trigonal warping on interference effects in bilayer graphene. Phys. Rev. Lett. **98**, 176806 (2007)
- 24. McCann, E., Fal'ko, V.I.: Weak localization and spin-orbit coupling in monolayer and bilayer graphene. In: Aoki, H., Dresselhaus, M. (eds.) Physics of Graphene. NanoScience and Technology, pp. 327–345. Springer International Publishing, Cham, Switzerland (2014)
- 25. Yu, C., et al.: Observation of quantum Hall effect and weak localization in p-type bilayer epitaxial graphene on SiC(0001). Solid State Commun. 175–176, 119–122 (2013)
- Engels, S., et al.: Limitations to carrier mobility and phase-coherent transport in bilayer graphene. Phys. Rev. Lett. 113, 126801 (2014)
- Chandni, U., Henriksen, E.A., Eisenstein, J.P.: Transport in indium-decorated graphene. Phys. Rev. B 91, 245402 (2015)
- Altshuler, B.L., Aronov, A.G.: Electron-electron interaction in disordered conductors. In: Efros, A.L., Pollak, M. (eds.) Electron-electron Interactions in Disordered Systems. Modern Problems in Condensed Matter Sciences, vol. 10, pp. 1–153. North-Holland Physics Publishing, Elsevier Science Publishers B.V., The Netherlands (1985)
- Lara-Avila, S., et al.: Disordered fermi liquid in epitaxial graphene from quantum transport measurements. Phys. Rev. Lett. 107, 166602 (2011)

# **Chapter 6 Intercalate Diffusion Pathways**

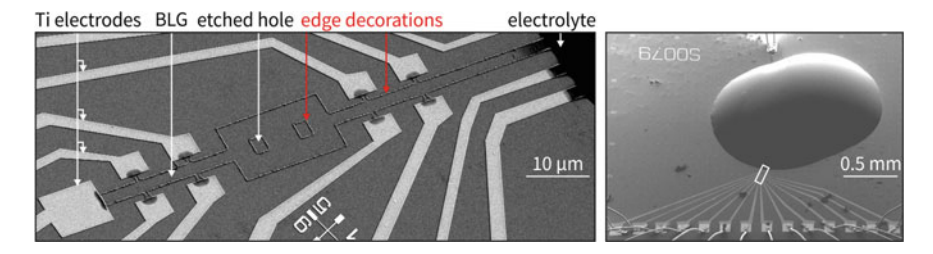


In this chapter we present extensive *ex situ* characterization of bilayer graphene devices after lithiation. Successful Li intercalation is revealed to cause material accumulation at bilayer graphene edges, see Fig. 6.1. With the Li activity in Lirich graphitic carbon being comparable to the one of metallic Li [1] we attribute this observed edge decoration to products of reactions caused by the intercalant. Reaction partners may be provided either from the residual gas atmosphere (although experiments are carefully performed at  $p \le 1 \cdot 10^{-6}$  mbar) or from mobile hydrocarbons on the sample surface stemming either from processing steps during device preparation or from the polymer electrolyte which possesses compounds with significant vapour pressure. We reveal these decoration to indeed contain Li, a finding which we exploit using particular device designs in order to unambiguously proof that the intercalation and diffusion of lithium occurs only in-between graphene sheets.

We first present and discuss experimental findings related to the bilayer graphene edge decorations in Sect. 6.1. In Sect. 6.2, we then discuss the special case of bilayer graphene devices that incorporate a natural junction with single layer graphene, chosen in order to help identify efficient Li diffusion pathways.

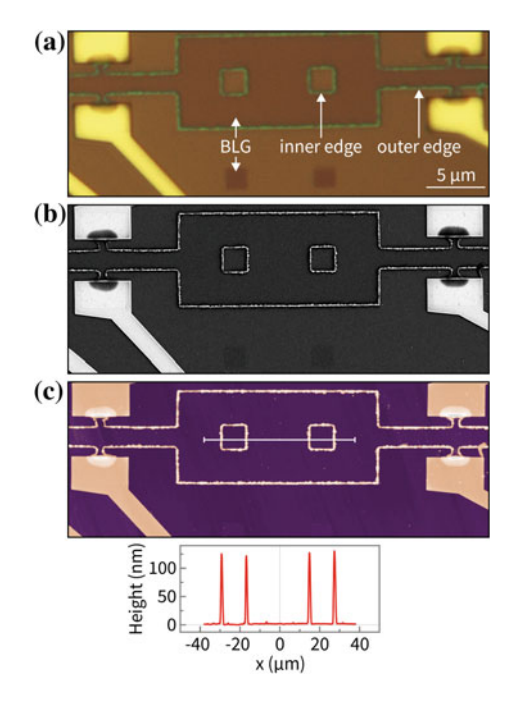
#### **6.1** Edge Decorations

We systematically find the edges of our bilayer graphene devices to be decorated with accumulated material after successful Li intercalation. These decorations can be observed, e.g., by optical microscopy, scanning electron microscopy (SEM) or atomic force microscopy (AFM), see Figs. 6.1 and 6.2. Here, the edge of two deliberately etched  $\sim 6~\mu m^2$  holes within the bilayer are clearly decorated as much as the outer device edges. From the initial graphene bilayer, two square patches have been etched such as to remain on the same sample surface but well separated from the device, see Fig. 6.2a. Their contrast in the optical micrograph helps both to recognize the bilayer graphene device in the figure as well as to compare their edges with the ones of the device. Using AFM, we extract both width and height of the accumulated material to



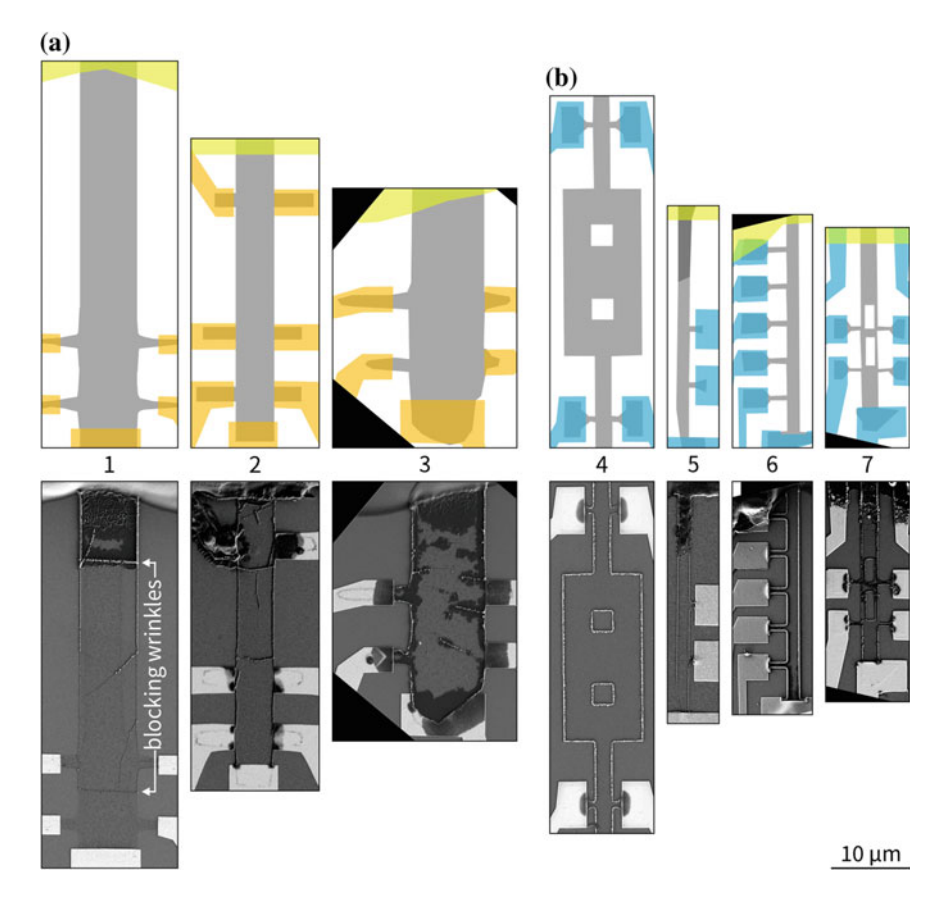
**Fig. 6.1** Scanning electron micrographs of a bilayer graphene (BLG) device after successful Li intercalation. Left image was acquired from the rectangular region indicated in the right micrograph

Fig. 6.2 Manifestation of bilayer graphene (BLG) edge decorations as observed by a optical microscopy, b SEM, and c AFM. The height profile in c is taken along the white line shown in the micrograph



be on the order of  $\sim 100\,\mathrm{nm}$  in the case of the shown device, see Fig. 6.2c. We include a height profile extracted along the white line in the micrograph, demonstrating the comparable height of the decoration at all four edges.

In the lower panel of Fig. 6.3, we show scanning electron micrographs of different bilayer graphene devices after successful Li intercalation (normalized to the same lateral scale), contacted with either Au electrodes (a) or Ti electrodes (b). The schematic of each device is shown in the upper panel of the figure, with the electrolyte placed towards the top of the page. For the sake of comparison, the device presented in Figs. 6.1 and 6.2 is shown again at position 4. In all cases we find edge decorations in qualitative agreement with the preceding observations. In addition, noticeable wrinkles in bilayer graphene also get decorated, see especially devices 1–3. These wrinkles stem from the transfer process during device fabrication.



**Fig. 6.3** Scanning electron micrographs of bilayer graphene devices after successful Li intercalation (lower row) with **a** Au electrodes and **b** Ti electrodes. Schematic sample layout (upper row), with bilayer graphene (light grey), multilayer graphene (dark grey), SiO<sub>2</sub> (white), Au (orange), Ti (blue), and the polymer electrolyte (yellow)

Although graphene's mechanical integrity should be preserved at wrinkles [2] the mechanical strain induced distortions of the sp²-bonds reportedly increase the local reactivity [3, 4]. In light of a possibly altered probability of Li permeation [5] it might become comprehensible that these wrinkles get decorated qualitatively similar to the device edges. During the course of this work, we were able to improve device fabrication such as to avoid a large number of wrinkles, see samples 4–7 as well as 8 & 9 in Fig. 6.4. In ideal cases (such as device 4, Figs. 6.1 and 6.2), no wrinkles are present.

Note that if wrinkles run completely across a bilayer graphene device perpendicular to the principle intercalant diffusion direction, edge decorations beyond (i.e., further away from the polymer electrolyte) tend to appear less pronounced. This is most evident in the case of devices 1 and 8. In the latter case, Li intercalation up to an intercalant density of  $n_{\rm Li} \approx (4 \pm 1) \cdot 10^{13} \, {\rm cm}^{-2}$  was achieved in the region

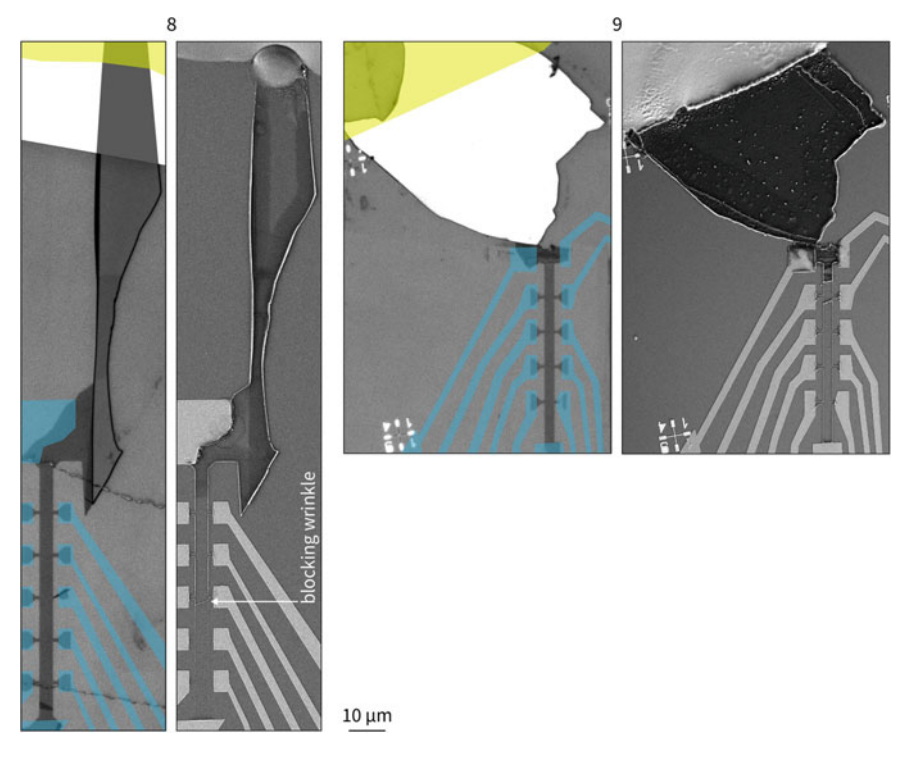


**Fig. 6.4** Scanning electron micrographs of bilayer graphene devices 8 and 9 after successful Li intercalation. To the left of each SEM image we show a schematic sample layout overlaid on an optical micrograph of the device, taken prior to electrode deposition, with Ti electrodes (blue) and polymer electrolyte (yellow)

beyond the wrinkle during the first lithiation cycle only. During subsequent lithiation/delithiation cycles, the charge carrier density in this region remained close to the value of the pristine device (i.e., before the first lithiation), within the electron-hole puddle regime. At the same time, Li-ions could be reversibly intercalated into the bilayer region before the wrinkle, although with the absolute magnitude of  $n_{Li}$  on the order of a few 10<sup>13</sup> cm<sup>-2</sup>, only. In other words, the wrinkle (or its decorated version) tends to hinder intercalant diffusion. From the SEM images, we can further conclude that the size of the edge decoration is related to both the magnitude of  $n_{\rm Li}$ , but also to the time during which bilayer graphene hosts intercalated Li. Although in the case of device 8 we only have a moderate  $n_{\rm Li} < 6 \cdot 10^{13} \, {\rm cm}^{-2}$  at all times, we still get a pronounced edge decoration due to the long duration (hours) of lithiation. Here, the low overall magnitude of Li content is most probably related to the special device layout, in which a graphene bilayer naturally extending from a thick multilayer flake was designed such that intercalating Li ions need to diffuse throughout the multilayer first, before entering the bilayer region. Similar to the case of device 9 (also shown in Fig. 6.4), we cannot determine the exact crystallographic connection between the bilayer and the thicker part of the flake, the exact interface between which might be

a bottle neck for Li diffusion. Secondly, due to staging which occurs in bulk graphite at higher Li content (see Sect. 3.1.1), the exact intercalant order configuration in the crystal might be such that intercalation in the bilayer is effectively hindered (unless in the case of stage 1).

Hence, although no systematic study was conducted, there is evidence for a connection between the amount of intercalated Li and the presence and size of edge decorations. As intercalated Li may not leave bilayer graphene other than at edges or at suitable defect sites, immobile reaction products may agglomerate at such sites. This scenario is highly likely, as the activity of Li in Li-rich graphitic carbon is known to be comparable to the one of metallic Li [1]. And although all our experiments are carefully performed in a high-vacuum environment ( $p < 1 \cdot 10^{-6}$  mbar), possible sources of reaction partners may readily be found in the residual atmosphere as well as in hydrocarbons on the sample surface stemming either from processing steps during device preparation or from the polymer electrolyte. A possible alternative for the observed phenomenon could be Li plating, which could be ruled out due to our mild lithiation conditions with the bilayer graphene at  $U_G \ge 0.05 \,\mathrm{V}$  versus Li/Li<sup>+</sup> and the ionic current being compliance-limited to a maximum of 10 nA. Usually, this current even remains in the pA-range or below during the experiment. In comparison, prolonged lithiation at  $U_G < 0.01 \,\mathrm{V}$  versus Li/Li<sup>+</sup> was shown to cause irreversible Li plating at the edges of ultrathin graphite sheets [6].

We employ time-of-flight secondary ion mass spectrometry (ToF-SIMS) in order to learn more about the chemical composition of the edge decorations. Here, a pulsed primary beam of  $Ga^+$  with an energy of 25 keV hits the sample at 45° incidence angle, and the secondary ions ejected from the surface are analyzed with respect to their mass and charge. We study both one device with Au electrodes (sample 2 in Fig. 6.3) as well as one device with Ti electrodes (sample 4 in Fig. 6.3), see Figs. 6.5 and 6.6, respectively. In panel a of both figures, we again show the scanning electron micrograph of the region of interest probed by ToF-SIMS. In panel b, we show ToF-SIMS data obtained from lateral scans of the primary ion beam. With a lateral resolution on the order of 100 nm, a direct comparison of the spatial distribution of C, Li and

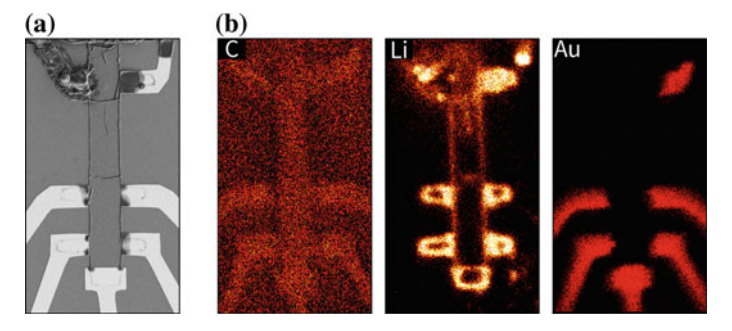


**Fig. 6.5** SEM image (**a**) and ToF-SIMS (**b**) of bilayer graphene device 2 shown in Fig. 6.3. Color in **b** is counts in arbitrary units, with dark (bright) representing a low (high) number of counts

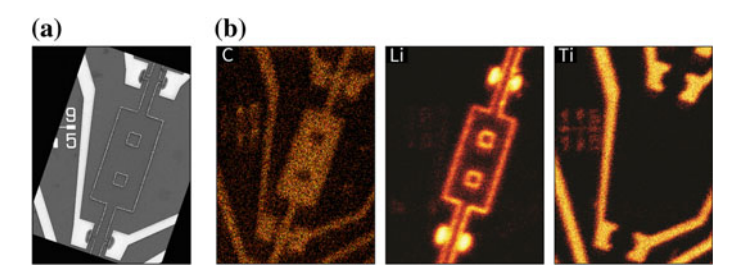


**Fig. 6.6** SEM image (a) and ToF-SIMS (b) of bilayer graphene device 4 shown in Fig. 6.3. Color in **b** is counts in arbitrary units, with dark (bright) representing a low (high) number of counts

Au (or Ti) with the SEM image in panel a is possible. We first of all clearly observe the presence of Au (or Ti) at the position of the electrodes. As expected, we also find C at the position of bilayer graphene. Also the  $\approx 6 \,\mu\text{m}^2$  holes etched into device 4 can be seen. 1 Most importantly however, ToF-SIMS reveals a high Li content of the edge decoration in both bilayer graphene devices as there is a clear correspondence between the spatial distribution of Li in the data and the edges of the bilayer. We furthermore see a qualitative difference between the Li distribution at the electrodes made of either Au or Ti: while in the first case bilayer graphene edges in the Aucovered area become visible, they remain invisible in the latter case. This observation is directly related to the different capability of alloying with Li, discussed in Sect. 3.3. In contrast to Ti, Au readily alloys with Li, thus acting like a Li-sink. Li intercalated in bilayer graphene covered by Au may thus lithiate the latter starting from defect sites or edges leading to the corresponding spatial distribution of Li in Fig. 6.5b. In the case of device 4, ToF-SIMS depth-profiling by intermittent  $O_2^+$ -sputtering (not shown) reveals Li-rich material having accumulated only near or on top of the Ti electrode, with no evidence for alloying as expected. While according to Fig. 6.5 Lirich material has partially also accumulated on top of Au electrodes, the Au and Li signals clearly show spatial overlap, unlike in the case of the Ti electrodes (Fig. 6.6).

The experimental evidence brought forward so far strongly suggests that Li intercalation and diffusion happens at the graphene/graphene interface only, i.e., in-between the two carbon sheets of bilayer graphene. The Li-rich material accumulation at inner bilayer graphene edges (around the holes etched into device 4, see Fig. 6.6) excludes Li transport along the sample perimeter only. Li-ions must have somehow travelled towards the center of the device to cause edge decorations of similar extent as at the sample perimeter (see Fig. 6.7 for a 3D representation of the AFM images of the device). If that Li transport took place at the graphene/vacuum interface, i.e., on top of bilayer graphene, a more homogeneous lithiation of the Au electrodes would be expected. Instead, lithiation of Au is found to preferentially start close to the bilayer graphene edges, see Fig. 6.5. In the following we strive to exclude Li-ion transport at the remaining graphene/SiO<sub>2</sub> interface.

<sup>&</sup>lt;sup>1</sup>To see increased counts of C on the electrodes, is related to the so-called relative sensitivity factor. It essentially means that the elemental sensitivity of ToF-SIMS depends on the local elemental environment. In this respect, ToF-SIMS must be regarded as a rather qualitative technique.

**Fig. 6.7** 3D representation of combined atomic force micrographs of device 4, shown in Figs. 6.1, 6.3, and 6.6



#### 6.2 Bilayer Graphene/Single Layer Graphene Junctions

In order to exclude a potential Li-ion diffusion pathway at the graphene/SiO<sub>2</sub> interface, we deliberately tailor device structures incorporating natural bilayer graphene/single layer graphene junctions. Such graphene flakes are routinely obtained as a natural result of mechanical exfoliation. An example is shown in Fig. 6.8. The scanning electron micrograph of the device taken after successful lithiation reveals the expected edge decorations phenomenologically similar to the samples discussed before. However, it can clearly be seen that the edge decoration stops at the natural interface with single layer graphene. This observation is striking, all the more so as during lithiation a small electronic current could flow through the whole device (including the single layer region), i.e., the electronic and hence crystallographic integrity of the device was given. It strongly suggests intercalation of Li between the two carbon planes of bilayer graphene only, whereas intercalation between bilayer graphene and the SiO<sub>2</sub>-substrate as well as Li migration on top of graphene planes can be excluded.

Additional support for these assertions has been collected from *in situ* timeresolved Hall measurements on a device where bilayer graphene is interrupted with a single layer region, but continues afterwards, see Fig. 6.9. While the Hall signal (and thus  $n_{\rm Li}$ ) changes due to Li diffusion up to single layer graphene, no change is observed in the bilayer part beyond the single layer portion. Due to the very mild lithiation conditions ( $n_{\rm Li} < 1.5 \cdot 10^{13} \, {\rm cm}^{-2}$  at all times), edge decorations are barely visible in the scanning electron micrograph taken after the experiment (right panel in Fig. 6.9a). Black lines indicate where edge decorations can be identified in the original image, notably all of which are before the single layer junction.

Our findings thus unequivocally demonstrate that intercalated Li resides and diffuses in between the two graphene sheets (G) of bilayer graphene only. Additional diffusion pathways at the G/SiO<sub>2</sub> and G/vacuum interfaces may indeed be ruled out, most strikingly due to evidence from experiments performed on bilayer graphene devices incorporating natural interfaces with single layer graphene. Our finding agrees with *ab initio* calculations according to which Li may intercalate in between graphene sheets only, but may not reside on its surface (down to the single layer limit) in the absence of defects [7]. Although facile Li diffusion on the graphene surface

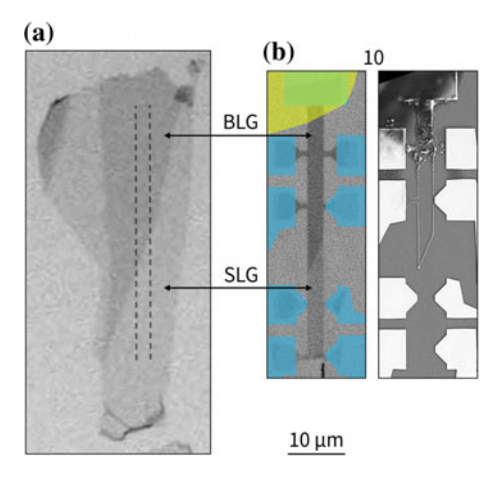


**Fig. 6.8** a Optical micrograph of a graphene flake with single layer graphene (SLG) and bilayer graphene (BLG) regions. **b** Scanning electron micrograph (right panel) of bilayer graphene device 10 after successful Li intercalation, fabricated from the flake shown in (**a**). Schematic sample layout overlaid on an optical micrograph of the device (left), taken prior to electrode deposition, with Ti electrodes (blue) and polymer electrolyte (yellow)

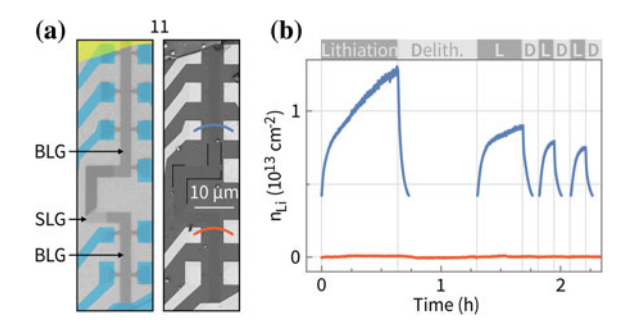


**Fig. 6.9** a Scanning electron micrograph (right panel) of bilayer graphene (BLG) device 11 after successful Li intercalation. Schematic sample layout overlaid on an optical micrograph of the device (left), taken prior to electrode deposition, with Ti electrodes (blue) and polymer electrolyte (yellow). The device features a single layer graphene (SLG) junction, i.e., one of the two carbon sheets of BLG is locally interrupted. **b** Time-dependent Li concentration  $n_{\rm Li}$  derived from in situ measurements of the Hall voltage during lithiation/delithiation of the bilayer graphene device shown in **a** both before and beyond the SLG junction (corresponding probes indicated in **a** in the same color)

(i.e., at the G/vacuum interface) was experimentally demonstrated, intercalation inbetween carbon sheets is energetically much more favorable [8]. Note that according to calculations, different interfaces such as G/hexagonal boron nitride (hBN) may indeed provide a Li diffusion pathway [9]. Thus one may not rule out *a priori* Li diffusion at interfaces other than G/G. In the case of our devices, however, that scenario applies.

6.3 Summary 101

## 6.3 Summary

While in strict terms, intercalation of Li-ions means that the latter reside and diffuse in between the two graphene sheets (G) of bilayer graphene only, one may not rule out a priori their diffusing on the top or bottom surface, too, i.e., at the G/SiO<sub>2</sub> or the G/vacuum interface. In this chapter we demonstrate however, that in our devices efficient Li intercalation can only be revealed between carbon sheets. To this end we combine ex situ techniques with specific device designs, exploiting the implications of our usual observation that edges and defects of successfully lithiated devices appear decorated with Li-rich material. This edge decoration is specific to the geometry addressed in this work with a spatial separation between the electrolyte and an uncovered region of the 2D material under study. Although the exact nature of this decoration remains to be understood, immobilized products of reactions between highly active Li and residues in the gas phase or hydrocarbons mobile on the sample surface provide a likely explanation. Similar processes must be expected in general for the intercalation of reactive species into layered materials with open edges or defects. These sites may act like a sink for the intercalant, which is undesirable when targeting high intercalant densities. It may be alleviated by optimizing the aspect ratio of the device to minimize the length of its perimeter and likely also by covering or sealing the edges in a suitable manner. For the same purpose, one needs to use inert electrode materials, as we demonstrate by comparing Ti with Au, only the former of which does not show alloying with Li.

#### References

- Winter, M., Besenhard, J.O.: Lithiated carbons. In: Daniel, C., Besenhard, J.O. (eds.) Handbook of Battery Materials, pp. 433–478. Wiley-VCH, Weinheim, Germany (2011)
- Calado, V.E., Schneider, G.F., Theulings, A.M.M.G., Dekker, C., Vandersypen, L.M.K.: Formation and control of wrinkles in graphene by the wedging transfer method. Appl. Phys. Lett. 101, 103116 (2012)
- 3. Zhang, Y., et al.: Enhanced reactivity of graphene wrinkles and their function as nanosized gas inlets for reactions under graphene. Phys. Chem. Phys. 15, 19042–19048 (2013)
- 4. Bissett, M.A., Konabe, S., Okada, S., Tsuji, M., Ago, H.: Enhanced chemical reactivity of graphene induced by mechanical strain. ACS Nano 7, 10335–10343 (2013)
- Yao, F., et al.: Diffusion mechanism of lithium ion through basal plane of layered graphene. J. Am. Chem. Soc. 134, 8646–8654 (2012)
- 6. Bao, W., et al.: Approaching the limits of transparency and conductivity in graphitic materials through lithium intercalation. Nat. Commun. **5**, 4224 (2014)
- Lee, E., Persson, K.A.: Li absorption and intercalation in single layer graphene and few layer graphene by first principles. Nano Lett. 12, 4624–4628 (2012)
- Mandeltort, L., Yates, J.T.: Rapid atomic Li surface diffusion and intercalation on graphite: A surface science study. J. Phys. Chem. C 116, 24962–24967 (2012)
- Shirodkar, S.N., Kaxiras, E.: Li intercalation at graphene/hexagonal boron nitride interfaces. Phys. Rev. B 93, 245438 (2016)

# Chapter 7 Intercalate Diffusion Kinetics



As could be shown in the preceding chapters, Li intercalated into our bilayer graphene devices diffuses in between graphene sheets, only. The intercalate diffusion continues into the part of the bilayer that is uncovered by the electrolyte. In this chapter we study the kinetics of this diffusion process using time-resolved in situ magnetotransport measurements.

In Sect. 7.1, we first give a brief introduction to chemical diffusion and how it manifests in Li-intercalated bulk graphite. We then present how we can locally monitor the time-dependent changes of the Li concentration  $n_{\rm Li}$  along a bilayer graphene device in Sect. 7.2. Describing Li diffusion using Fick's second law, we provide a numerical solution that conforms to the boundary conditions given by our experiment in Sect. 7.3. Applying it to our data in Sect. 7.4, we extract for the first time the chemical diffusion coefficient for Li in bilayer graphene.

# 7.1 Li Diffusion in Graphite

The activated random (Brownian) motion of particles in a system is at the microscopic origin of diffusion, a process often defined by its macroscopic tendency to even out spatial variations in the particle concentration c with time. While diffusion prevails even in homogeneous systems, as long as the temperature is high enough, the aforementioned tendency is readily captured within the phenomenological framework of Fick's laws of diffusion,

$$J = -D\frac{\partial c}{\partial x},\tag{7.1}$$

$$\frac{\partial c}{\partial t} = D \frac{\partial^2 c}{\partial x^2}. (7.2)$$

The first law, Eq. 7.1, relates a gradient in the particle concentration to a particle flux J, often referred to as steady-state diffusion. The second law, Eq. 7.2, formulates a time-varying diffusion equation, i.e., it describes non-steady-state diffusion. The diffusion coefficient D (here assumed independent of x and c), is a measure of the mobility of a given type of particle in a given environment at a given temperature and pressure. It is quantitatively related to the underlying diffusion mechanisms allowed in the system.

The following discussion will be limited to the relevant case of Li-intercalated graphite. In this material, diffusion of both Li-ions and free conduction electrons (or holes) occurs. The graphite host is considered a framework in which these two particle species move. Graphite being a predominantly electronic conductor (electrons or holes are significantly more mobile than intercalated Li-ions), the effect of electric fields on Li transport may be neglected [2]. During intercalation/deintercalation, Li-ions diffuse between the carbon planes by ambipolar motion coupled to electrons [3]. This process involves a net macroscopic transport of mass and is called chemical diffusion. In general terms, the diffusion flux is proportional to the gradient in chemical potential, which only in special cases equals the concentration gradient [4]. The gradient in chemical potential acts as an internal driving force, enhancing the chemical diffusion coefficient  $D^{\delta}$  with respect to the self-diffusion coefficient  $D^{\delta}$  (the diffusivity in the absence of concentration gradients) by the so-called thermodynamic enhancement factor. The symbol  $D^{\delta}$  is used to indicate a concentration dependence of the chemical diffusion coefficient.

In Fig. 7.1, we give an overview over room-temperature values for  $D^{\delta}$  of Li in graphite, reported from electrochemical experiments in Refs. [5–14]. Data reported as a function of known or estimated values of Li content x in Li $_x$ C $_6$  appear in the left graph, while data reported as a function of electrode potential versus Li/Li<sup>+</sup> appear in the right graph. Experimental values for which neither x nor the electrode potential is explicitly reported are given in the central graph. The values spread over seven orders of magnitude for several reasons:

- The practical graphite electrodes employed in most mentioned references are composites containing the insertion compound (graphite, typically as a powder) and additives such as binders. In such a composite, Li diffusion is a complex process with  $D^{\delta}$  being an effective parameter.
- The extraction of  $D^{\delta}$  from electrochemical measurements relies on models that are often based on assumptions about inaccessible parameters, such as the molar volume of lithiated material or the active surface area. The correct extraction of  $D^{\delta}$  is therefore subject of debate [9, 12, 13].
- $D^{\delta}$  depends on the Li content x in Li<sub>x</sub>C<sub>6</sub> with  $0 \le x \le 1$ . In the dilute limit ( $x \to 0$ ), the interlayer spacing is expected to dominantly influence the Li diffusivity, with a wider van der Waals gap facilitating more rapid Li diffusion [15]. For increasing values of x, one may expect a decrease in  $D^{\delta}$  due to the increasing importance of

<sup>&</sup>lt;sup>1</sup>The carbon atoms may in principle also diffuse. The level of associated activation energies is, however, large compared to temperatures relevant to this work [1].

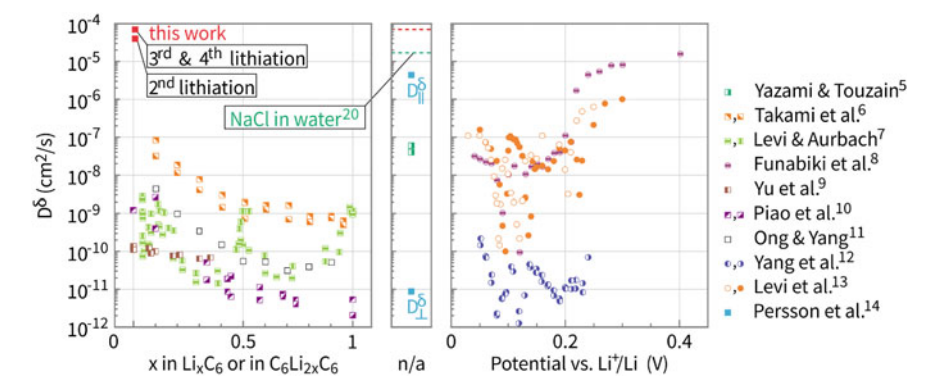


Fig. 7.1 Room-temperature chemical diffusion coefficient  $D^{\delta}$  of Li in graphite from different electrochemical experiments, reported as a function of composition x in Li<sub>x</sub>C<sub>6</sub> (left panel) or as a function of electrode potential versus Li/Li<sup>+</sup> (right panel). In case neither is explicitly stated in the reference, data is shown in the middle panel together with  $D^{\delta}$  for NaCl in water from Ref. [20] (green dashed line). See the respective references for details.  $D^{\delta}_{\parallel}$  and  $D^{\delta}_{\parallel}$  represent Li diffusion mainly perpendicular and parallel to the carbon sheets in bulk graphite, respectively. Values for  $D^{\delta}$  of Li in bilayer graphene extracted from our experiment are shown as red squares

repulsive Li-Li interaction [15]. At high values of x, intercalant ordering and phase transitions influence the diffusion coefficient. Despite contradicting reports, [15] experiments point towards minima (maxima) in  $D^{\delta}$  for coexisting phases (pure phases) [7, 8, 12].

• Li diffusion in graphitic carbon is highly anisotropic. The individual graphene sheets being in fact impermeable to Li, [16] diffusion in graphitic carbon proceeds preferentially coplanar with the graphene sheets, [17] i.e., parallel to the basal planes. In *c*-axis direction, Li may only diffuse via certain defect sites or grain boundaries [18, 19].

The anisotropic character of Li diffusion was maybe most strikingly demonstrated in Ref. [14]. Using a two-compartment cell with HOPG membranes in basalplane and edge-plane configuration, Persson et al. [14] determined the coefficients for Li diffusion mainly perpendicular  $(D_{\perp}^{\delta} \approx (8.7 \pm 0.4) \cdot 10^{-12} \, \mathrm{cm^2/s})$  and parallel  $(D_{\parallel}^{\delta} \approx (4.4 \pm 0.1) \cdot 10^{-6} \, \mathrm{cm^2/s})$  to the graphene basal planes. The vast majority of other reported data points fall in between the bounds set by  $D_{\perp}^{\delta}$  and  $D_{\parallel}^{\delta}$ , see Fig. 7.1. The spread in reported values of  $D_{\parallel}^{\delta}$  might thus also be partially attributed to the referenced experiments effectively probing different ratios of  $D_{\parallel}^{\delta}/D_{\perp}^{\delta}$ . This can be the case insofar as related sample parameters differ between these experiments, such as the ratio of edge versus basal planes or the characteristic amount of defects in the basal planes. In other words, different setups or methods might show a different sensitivity in addressing each of the two diffusion pathways. Indeed, techniques such as quasi-elastic neutron scattering (QENS), which are sensitive mainly to the in-plane diffusivity, report high values of the Li self-diffusion coefficient D at considerable composition of  $x \geq 0.375$  [21, 22], albeit measured at several 100 K above room

temperature where D is further enhanced. Jungblut and Hoinkins [23] also report extremely high values of  $D^{\delta} > 10^{-4} \, \mathrm{cm^2/s}$  at very low x from time-resolved release experiments performed in an ultrahigh vacuum environment, however likewise at extremely high temperature  $T > 1000 \, \mathrm{K}$ .

In the following we turn to bilayer graphene, in which intercalate diffusion is restricted to an in-plane component, only. With some of the bulk phenomenology, such as staging, being absent in this system, it may still reflect some bulk properties insofar as the in-plane diffusivitiy has not been found to be highly influenced by the next-nearest intercalate layers in the bulk [15].

### 7.2 Measurement Setup for Intercalate Diffusion Studies

In order to access the kinetics of intercalate diffusion in bilayer graphene, we use the device configuration shown in Fig. 7.2. The elongated, narrow device geometry with multiple potential probes along the perimeter of uncovered bilayer graphene and with Li-ions emanating from one side only lends itself superbly to the study of Li-ion diffusion and its dynamics. The Li density  $n_{\rm Li}$  can be monitored continuously as a function of time and at discrete positions by simultaneously measuring the Hall voltage  $U_{xy}$  which develops across the bilayer at different distances from the graphene/electrolyte interface. To this end, we impose a constant<sup>2</sup> dc-current through the bilayer and apply a constant perpendicular magnetic field  $B = 10 \,\mathrm{T}$ . The Hall voltage  $U_{xy}(x)$  building up at different positions  $x = x_i$  with  $i = \{0, 1, 2, 3\}$  is directly related to the local charge carrier density  $n(x) = BI/eU_{xy}(x)$ . In line with the reasoning in Sect. 4.3, assuming a complete charge transfer of 1e per intercalated Li-ion (with e the elementary charge of an electron), the measured density of electrons  $n_e$  equals the intercalated Li density  $n_{Li}$ , minus an initial charge density from intrinsic doping sources  $n_{\text{imp}}$ . The latter can be extracted from a Hall measurement prior to Li intercalation and was found to be  $n_{\rm imp} \approx 2 \cdot 10^{12} \, {\rm cm}^{-2}$  for the device shown in Fig. 7.2.<sup>3</sup> It follows that  $n_{Li}(x, t) = n_e(x, t) - n_{imp}(x, t = 0)$ .

In Fig. 7.3a, we plot  $U_{xy}(x,t)$  measured at  $x=x_i$  with  $i=0,\ldots,3$  using time-synchronized 7 1/2-digit PXI digital multimeters. Because the raw data contains  $\approx 250$  points per minute for each trace, the plots in Fig. 7.3 are obtained after the application of a moving average with a width of  $\approx 13$ s. Using a high-input impedance precision source/measure unit, we potentiostatically polarize the device by setting the gate voltage  $U_G$  between bilayer graphene and the Li counter electrode to  $U_G=0.05$  V versus Li/Li<sup>+</sup> ( $U_G=1.5$  V vs. Li/Li<sup>+</sup>) in order to drive lithiation

 $<sup>^2</sup>$ We actually measure the dc-current. During the experiment, the absolute value of the dc-current is found to vary by <1.3%.

<sup>&</sup>lt;sup>3</sup>Both the position in backgate voltage of the maximum resistance (charge neutrality point) as well as SdH oscillations measured prior to the deposition of the electrolyte were found to agree with this impurity density.

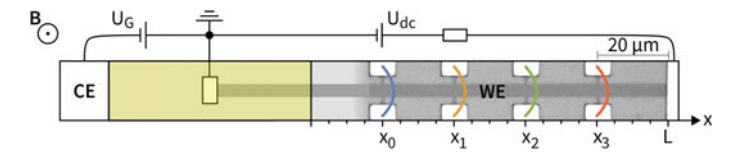


Fig. 7.2 Schematic bilayer graphene (working electrode, WE)|polymer electrolyte|Li (counter electrode, CE) cell used for the measurement of the chemical diffusion coefficient  $D^{\delta}$  of Li in bilayer graphene. An optical micrograph of the device is included. The Hall voltage  $U_{xy}$  is measured at different positions using the Ti contact pairs at  $x_i$  with  $i = \{0, 1, 2, 3\}$ 

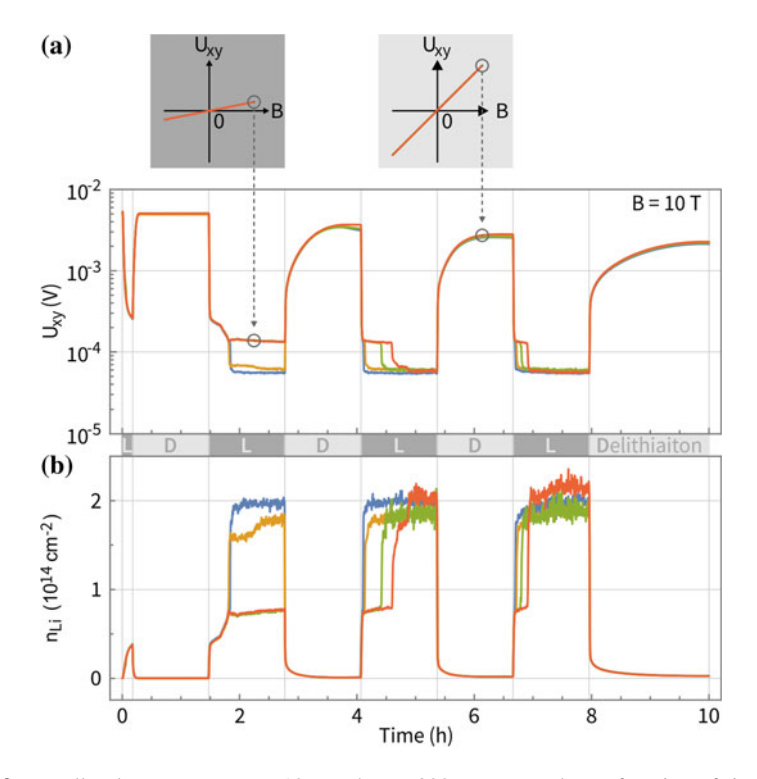


Fig. 7.3 a Hall voltage  $U_{xy}$  at  $B=10\,\mathrm{T}$  and  $T=300\,\mathrm{K}$  measured as a function of time at the four different positions  $x_0,\ldots,x_3$  of the bilayer graphene device shown in Fig. 7.2 during several lithiation/delithiation cycles (colors correspond to the Hall probe colors used in Fig. 7.2). A dc excitation current  $I\approx 1.6\,\mu\mathrm{A}$  was used. Insets schematically show the *B*-dependent Hall trace in lithiated and delithiated condition. **b** Li concentration  $n_{\mathrm{Li}}$  extracted from (a) as discussed in the main text

(delithiation). Thus, four consecutive lithiation/delithiation cycles are performed, all at a controlled temperature of  $T = 300 \,\mathrm{K}$  and in a high-vacuum atmosphere  $p < 1 \cdot 10^{-6}$  mbar. It can be seen that Li intercalation is followed by fast diffusion of Li along the device, as  $U_{xy}$  reproducible drops by up to about two orders of magnitude at all four positions  $x_0, \ldots, x_3$  in the uncovered bilayer graphene region. This reflects the strong increase in electron density  $n_e$  brought about by the intercalating Li-ions. Upon delithiation,  $U_{xy}$  increases again towards its initial values, reflecting the deintercalation of Li-ions. A slight decrease with time of the maximum value to which  $U_{xy}$  is restored upon delithiation is observed, which we attribute to intercalated Li being irreversibly trapped inside the uncovered region of bilayer graphene, possibly due to reactions at defect sites or the like. However after 10 h, the associated irreversible charge carrier density is  $< 3 \cdot 10^{12} \, \text{cm}^{-2}$  confirming an overall high degree of reversibility. The densities  $n_{Li}(x, t)$  of intercalated Li at positions  $x_0, \ldots, x_3$  are plotted in Fig. 7.3b as extracted from  $U_{xy}$  by the procedure described above. It can be seen that during the first lithiation, a comparatively slower increase in  $n_{\rm Li}(x,t)$  is observed than during higher cycle numbers, likely due to the formation of the SEI (see Sect. 3.1.2). Furthermore, highest Li densities on the order of  $n_{\rm Li} \approx 2 \cdot 10^{14} \, {\rm cm}^{-2}$  are reached first at electrodes closer to the electrolyte/bilayer graphene interface. Sudden increases in  $n_{\rm Li}$  observed at later points in time at electrodes further away probably indicate the sudden weakening of some local restraining conditions on intercalation. Such might be induced by folds/wrinkles in the sample or residues from device fabrication potentially locally blocking intercalation pathways up to a certain moment. Due to these experimental findings, as well as due to the more significant noise level at lower values of  $U_{xy}$  (respectively higher values of  $n_{Li}$ ), we will consider the Li diffusion kinetics in the lower density regime, i.e., up to  $\approx 1 \cdot 10^{13}$  cm<sup>-2</sup>.

#### 7.3 Numerical Solution to Fick's Second Law

The Li intercalate diffusion kinetics in bilayer graphene can be described by Fick's second law, Eq. 7.2. We apply it following a numerical approach in an explicit scheme. In the relevant case of directed Li diffusion in one dimension, Eq. 7.2 may be restated as

$$\frac{\partial n_{\rm Li}(x,t)}{\partial t} = D^{\delta} \frac{\partial^2 n_{\rm Li}(x,t)}{\partial x^2},\tag{7.3}$$

where  $D^{\delta}$  is the chemical diffusion coefficient for Li in bilayer graphene, which we can regard as independent of density within a small density range in an in-plane disordered phase (i.e., at low density of intercalated Li). We consider the boundary conditions

$$n_{\mathrm{Li}}(0,t) = n_{\mathrm{Li}}^{\mathrm{meas}}(0,t) \qquad \frac{\partial n_{\mathrm{Li}}(x,t)}{\partial x} \bigg|_{x=L} = 0. \tag{7.4}$$

The first boundary condition sets the Li density at  $x = x_0 = 0$  equal to the measured one at all times t. The second boundary condition imposes zero flux at the ionically blocking electrode at x = L at all times t. We replace the derivatives in time and space by their approximative finite-difference formulations

$$\frac{\partial n_{\text{Li}}}{\partial t}\Big|_{x_i,t_j} = \frac{n_i^{j+1} - n_i^j}{\Delta t}, \qquad \frac{\partial^2 n_{\text{Li}}}{\partial x^2}\Big|_{x_i,t_j} = \frac{n_{i+1}^j - 2n_i^j + n_{i-1}^j}{(\Delta x)^2}.$$
(7.5)

Here we make the transition from continuous variables x and t to discrete ones  $x_i$  and  $t_j$ , and we write  $n_i^j = n_{Li}(x_i, t_j)$ ,  $\Delta t = t_{j+1} - t_j$  and  $\Delta x = x_{i+1} - x_i$ . Combining Eqs. 7.3 and 7.5, we can write

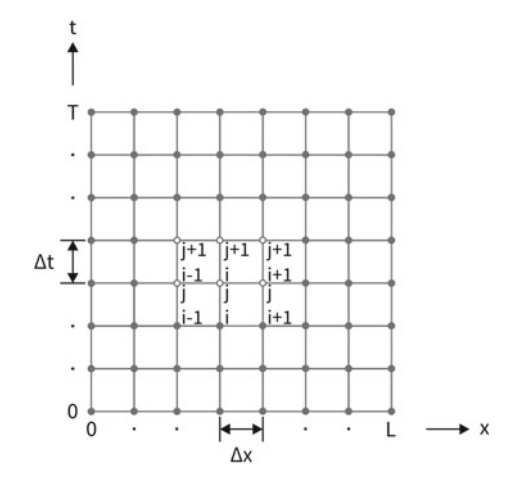
$$n_i^{j+1} = n_i^j + D^\delta \Delta t \frac{n_{i+1}^j - 2n_i^j + n_{i-1}^j}{(\Delta x)^2},$$
(7.6)

which gives a solution stable in time if

$$\frac{D^{\delta} \Delta t}{(\Delta x)^2} \le \frac{1}{2}.\tag{7.7}$$

As shown in Fig. 7.4, we devide the region of interest of the sample of length L into  $N_x = L/\Delta x + 1$  discrete steps in x direction. In our case (device shown in Fig. 7.2)  $L = 80 \,\mu\text{m}$  and  $\Delta x = 1 \,\mu\text{m}$  yielding  $N_x = 81$  steps. We discretize the time domain within the time frame of interest into  $N_t$  steps depending on the choice of  $D^{\delta}$  respecting the stability condition Eq. (7.7). We start with an initial density profile  $n_i^0 = 0$  for all  $i = 0 \dots (N_x - 1)$ . Taking into account the boundary conditions (Eqs. 7.4), we first set  $n_0^1 = n_{\text{Li}}^{\text{meas}}(0, t_1)$ , then calculate  $n_i^1$  according to Eq. 7.6 for

Fig. 7.4 Schematic grid used for our numerical calculation of Fick's second law



 $i=1\dots(N_x-2)$  and finally set  $n^1_{i=N_x-1}=n^1_{i=N_x-2}$ . We then proceed with  $t_j$  for  $j=2\dots(N_t-1)$ . Depending on the choice of  $D^\delta$ ,  $\Delta t$  needs to be chosen such that the stability criterion (Eq. 7.7) is fulfilled. Hence,  $n^j_0$  is extracted from the measured  $n_{\rm Li}(0,t)$  by interpolation, if needed. The solution provides us with both the Li density profile across the sample at a given time  $t_j$ , as well as the time-dependent evolution of the Li density at a specific position  $x_i$ .

#### 7.4 Li Diffusion Kinetics in Bilayer Graphene

We start considering first the Li diffusion kinetics during the second lithiation cycle of the device shown in Fig. 7.2. Both the device schematic as well as the relevant data are plotted again in Fig. 7.5, this time without the application of a moving average.

The Li densities  $n_{\rm Li}(x,t)$  at positions  $x_0=0$ ,  $x_1=20\,\mu{\rm m}$ ,  $x_2=40\,\mu{\rm m}$ , and  $x_3=60\,\mu{\rm m}$  are plotted up to  $\approx 10^{13}\,{\rm cm}^{-2}$  in the left panel of Fig. 7.5. They exhibit a steep increase with time. The Li density is always higher at positions closer to

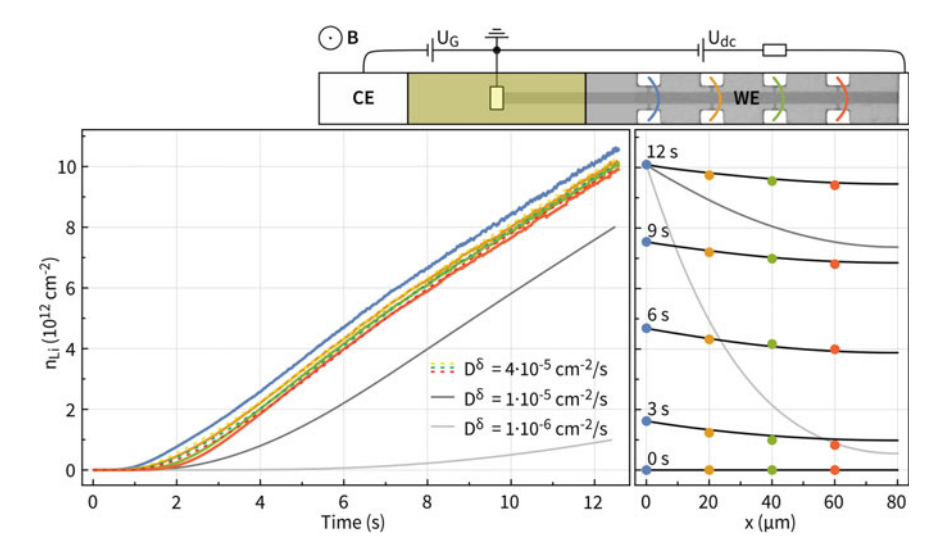


Fig. 7.5 Direct measurement of Li diffusion. The schematic of the  $C_6 \text{Li}_x C_6$  (WE)|polymer electrolyte (yellow shaded area)|Li (CE) cell includes an optical micrograph of the uncovered bilayer graphene area. The probes used for the Hall measurements are marked in the same color as the corresponding data set. Left panel: Li concentration  $n_{\text{Li}}$  extracted from Hall measurements at  $B=10\,\text{T}$  and  $T=300\,\text{K}$  as a function of time at four positions along the bilayer graphene device (blue, yellow, green and red). Dashed lines of slightly different color are solutions to Eq. 7.3 for  $D^{\delta}=4\cdot 10^{-5}\,\text{cm}^2/\text{s}$  as explained in the text. Solutions for lower values of  $D^{\delta}$  are shown as grey lines. Right panel: Li density profiles across the bilayer at different times (black lines), with measured values shown as colored dots. Grey lines show the density profile for the same lower  $D^{\delta}$  values as in the left panel

the electrolyte as expected. The data is numerically evaluated according to the procedure described in the previous Sect. 7.3, which has—in view of the very fast transport kinetics—the advantage that unavoidable preceding transients can be implicitly taken account of. The numerical solutions  $n_{1i}(x, t)$  to Eq. 7.2 for  $x = x_1$ ,  $x = x_2$ , and  $x = x_3$  are displayed as dashed lines (yellow, green, red, respectively) for  $D^{\delta} = 4 \cdot 10^{-5} \,\mathrm{cm}^2/\mathrm{s}$ . The experimentally extracted density  $n_{\mathrm{Li}}(x_0, t)$  (blue) at  $x = x_0$  serves as a boundary condition for solving Eq. 7.2 numerically. In order to illustrate how variations of the diffusion coefficient affect the time-dependent evolution of Li densities, solutions for  $n_{Li}(x_3, t)$  at  $x_3 = 60 \,\mu\text{m}$  are also plotted for  $D^{\delta} = 1 \cdot 10^{-5} \,\mathrm{cm^2/s}$  and  $D^{\delta} = 1 \cdot 10^{-6} \,\mathrm{cm^2/s}$  (dark and light grey, respectively). These lower values of  $D^{\delta}$  lead to a clear discrepancy with the experiment. In the right panel of Fig. 7.5, the density profiles along the device  $n_{Li}(x, t)$  (black) are plotted at different times t = 0 s, 3 s, 6 s, 9 s, and 12 s for  $D^{\delta} = 4 \cdot 10^{-5}$  cm<sup>2</sup>/s. For the sake of comparison, the experimentally measured densities have been superimposed. The striking agreement between the numerical solution and experiment corroborates further our extracted value of  $D^{\delta}$  and the overall validity of our approach. Solutions  $n_{\text{Li}}(x, t = 12 \text{ s})$  for  $D^{\delta} = 1 \cdot 10^{-5} \text{ cm}^2/\text{s}$  and  $D^{\delta} = 1 \cdot 10^{-6} \text{ cm}^2/\text{s}$  have been included in the right panel of Fig. 7.5 as well (dark and light grey lines, respectively) and confirm a significant deviation from experiment as  $D^{\delta}$  is lowered from the best fit value.

A closer inspection between the solution for  $D^{\delta} = 4 \cdot 10^{-5} \,\mathrm{cm}^2/\mathrm{s}$  and the measurement reveals that within the time frame displayed in Fig. 7.5, good agreement is achieved at intermediate densities while at both the lower and the upper density end the agreement is less convincing. The disagreement at the low density end, i.e., the case of very dilute intercalation, can be understood in terms of the small van der Waals gap between the graphene layers imposing a high activation energy for Li diffusion [23]. This effectively implies the need for a reduction of the chemical diffusion coefficient  $D^{\delta}$  to achieve a better match between the numerical solution and the measurement for this initial intercalation stage. With more Li entering in between the two graphene layers, the activation energy for diffusion decreases as the van der Waals gap is widened.  $D^{\delta}$  consequently increases (for intermediate densities in Fig. 7.5) until interactions between intercalated atoms make themselves felt by reducing it again. This density dependence as well as other influences making  $D^{\delta}$  concentration dependent have not been taken account in Eq. 7.2. As mentioned above, experimental and theoretical studies on graphitic carbon suggest a lowering of  $D^{\delta}$  as  $n_{\text{Li}}$  increases as the general trend [9, 14]. However, its actual dependence bears a certain complexity as it involves possible competition between ordered intercalate phases. Our experimental findings indicate a decrease in  $D^{\delta}$  at the high density end in Fig. 7.5. It is also important to note that the evaluated  $D^{\delta}$  is distinctly higher than the surface diffusion coefficient [24], thus ruling out intercalation to happen by surface diffusion followed by vertical intercalation.

Apart from the above considerations, the kinetics is bound to also depend on the specific intercalation history [17]. During the first lithiation cycle, the solidelectrolyte interphase (SEI) is formed between bilayer graphene and the polymer electrolyte to establish a proper pathway for intercalation of Li into the bilayer (see

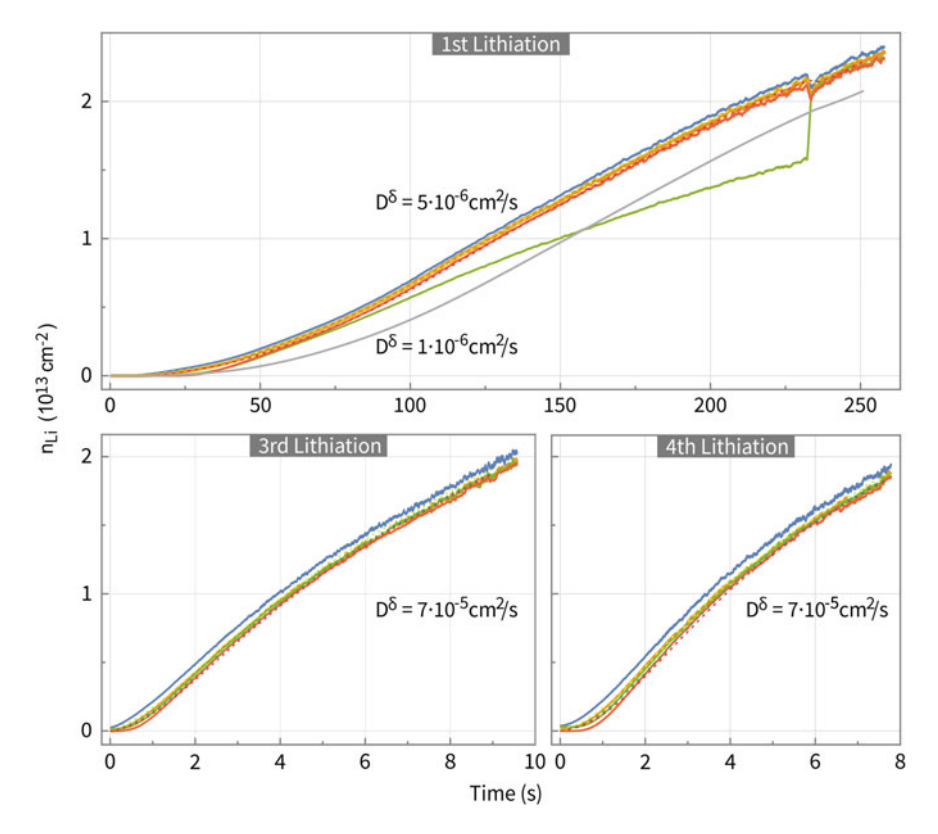


Fig. 7.6 Li diffusion in the bilayer graphene device shown in Fig. 7.5: 1st, 3rd and 4th lithiation. The yellow, green and red dashed lines are numerical fits to the data (solid lines) measured at  $x_1=20\,\mu\text{m}$ ,  $x_2=40\,\mu\text{m}$  and  $x_3=60\,\mu\text{m}$ , respectively. In the upper panel, the measured Li concentration at  $x_2=40\,\mu\text{m}$  (green solid line) shows an unexpected time dependence, presumably due to a local restraint on Li accumulation suddenly loosening at  $t\approx230\,\text{s}$ .  $n_{\text{Li}}(x=60\,\mu\text{m},t)$  calculated for  $D^\delta=1\cdot10^{-6}\,\text{cm}^2/\text{s}$  is plotted as a solid grey line

Sect. 3.1.2). This is why we chose the second lithiation cycle for the preceding analysis. Li diffusion may also be hampered by the presence of adsorbates or residues (e.g., from nanofabrication processes requiring resists), folds, wrinkles or other microscopic imperfections of the device. Some of these may be relieved at higher lithiation cycle numbers while others may potentially inflict a complete blocking of Li diffusion.

In Fig. 7.6, the time-dependence of the Li density  $n_{\rm Li}(x,t)$  is displayed for the first, third, and fourth lithiation. Again the data (colored, solid lines) were extracted from simultaneous Hall measurements at the same four positions  $x_i$  with  $i = \{0, 1, 2, 3\}$  outside the electrolyte and spaced apart by  $20 \,\mu\text{m}$ . For the third lithiation (lower left panel), good agreement with a numerical solution to Fick's second law can be obtained for  $D^{\delta} \approx 7 \cdot 10^{-5} \, \text{cm}^2/\text{s}$ . For the fourth lithiation (lower right panel),

this value even seems to underestimate the fast Li diffusion measured in the experiment. Intercalate diffusion is slower during the very first lithiation (top panel). Here,  $n_{\rm Li}^{\rm meas}(x_2,t)$  (green solid line) also shows unexpected behavior which may be attributed to the sudden loosening of a local restraining condition on Li accumulation at  $t \approx 230\,\mathrm{s}$  (such as residues located on top of the bilayer or possibly a wrinkle, locally blocking Li atoms from entering a certain region). After the first lithiation, intercalate diffusion seems to be more reproducible with a tendency to become more facile at higher lithiation cycle numbers.

In Fig. 7.1, we compare the Li in-plane diffusion coefficient obtained here on freely exposed bilayer graphene with the experimental values reported for the chemical diffusion coefficient in bulk graphite. The room temperature diffusion coefficients extracted in this work exceed all these values by one order of magnitude. They are in fact even higher than  $D^{\delta} = 1.6 \cdot 10^{-5} \, \mathrm{cm^2/s}$  for NaCl in water [20]. In bulk graphite a comparably high diffusivity of Li has before only been observed in high-temperature studies, see Refs. [21, 23].

#### 7.5 Summary

The intercalate diffusion in graphitic carbon can be described by Fick's laws of diffusion. In the presence of a concentration gradient, the chemical diffusion coefficient  $D^{\delta}$  characterizes the mobility of the diffusing species. Experimentally determined room-temperature values of  $D^{\delta}$  describing Li diffusion in graphitic carbon spread over several orders of magnitude,  $D^{\delta} \approx 10^{-12} - 10^{-5} \,\mathrm{cm}^2/\mathrm{s}$ . This is due to the highly anisotropic nature of the diffusion process in bulk graphite, its concentration dependence, and to experimental difficulties to reliably access and extract the diffusion coefficient. We demonstrate that bilayer graphene devices can serve as a powerful platform to study the intercalate diffusion. Using time-resolved in situ Hall measurements, we monitor the temporal evolution of the Li concentration  $n_{Li}$  at different locations along a bilayer graphene device during several lithiation/delithiation cycles. Combined with a numerical solution to Fick's second law of diffusion, we get unprecedented direct access to the Li-diffusion kinetics in bilayer graphene. We extract record in-plane chemical diffusion coefficients for Li at room temperature, up to  $D^{\delta} = 7 \cdot 10^{-5} \,\mathrm{cm^2/s}$ , beyond the upper limit of values reported from studies on bulk graphite [5–14].

#### References

- Kanter, M.A.: Diffusion of carbon atoms in natural graphite crystals. Phys. Rev. 107, 655–663 (1957)
- 2. Van der Ven, A., Bhattacharya, J., Belak, A.A.: Understanding Li diffusion in Li-intercalation compounds. Acc. Chem. Res. 46, 1216–1225 (2013)

- Maier, J.: Size effects on mass transport and storage in lithium batteries. J. Power Sources 174, 569–574 (2007)
- Mehrer, H.: Diffusion in solids. Springer Series in Solid-State Sciences, vol. 155. Springer, Berlin (2007)
- 5. Yazami, R., Touzain, P.: A reversible graphite-lithium negative electrode for electrochemical generators. J. Power Sources **9**, 365–371 (1983)
- Takami, N., Satoh, A., Hara, M., Ohsaki, T.: Structural and kinetic characterization of lithium intercalation into carbon anodes for secondary lithium batteries. J. Electrochem. Soc. 142, 371–379 (1995)
- Levi, M.D., Aurbach, D.: Diffusion coefficients of lithium ions during intercalation into graphite
  derived from the simultaneous measurements and modeling of electrochemical impedance and
  potentiostatic intermittent titration characteristics of thin graphite electrodes. J. Phys. Chem.
  B 101, 4641–4647 (1997)
- 8. Funabiki, A., et al.: Impedance study on the electrochemical lithium intercalation into natural graphite powder. J. Electrochem. Soc. **145**, 172–178 (1998)
- 9. Yu, P., Popov, B.N., Ritter, J.A., White, R.E.: Determination of the lithium ion diffusion coefficient in graphite. J. Electrochem. Soc. **146**, 8–14 (1999)
- Piao, T., Park, S.-M., Doh, C.-H., Moon, S.-I.: Intercalation of lithium ions into graphite electrodes studied by AC impedance measurements. J. Electrochem. Soc. 146, 2794–2798 (1999)
- Ong, T.S., Yang, H.: Lithium intercalation into mechanically milled natural graphite: electrochemical and kinetic characterization. J. Electrochem. Soc. 149, A1–A8 (2002)
- Yang, H., Bang, H.J., Prakash, J.: Evaluation of electrochemical interface area and lithium diffusion coefficient for a composite graphite anode. J. Electrochem. Soc. 151, A1247–A1250 (2004)
- Levi, M.D., Markevich, E., Aurbach, D.: The effect of slow interfacial kinetics on the chronoamperometric response of composite lithiated graphite electrodes and on the calculation of the chemical diffusion coefficient of Li ions in graphite. J. Phys. Chem. B 109, 7420–7427 (2005)
- 14. Persson, K., et al.: Lithium diffusion in graphitic carbon. J. Phys. Chem. Lett. **1**, 1176–1180 (2010)
- Persson, K., Hinuma, Y., Meng, Y.S., Van der Ven, A., Ceder, G.: Thermodynamic and kinetic properties of the Li-graphite system from first-principles calculations. Phys. Rev. B 82, 125416 (2010)
- 16. Berry, V.: Impermeability of graphene and its applications. Carbon 62, 1–10 (2013)
- 17. Magerl, A.: Intercalate diffusion. In: Zabel, H., Solin, S.A. (eds.) Graphite Intercalation Compounds I. Springer Series in Materials Science, vol. 14, pp. 221–246. Springer, Berlin (1990)
- Yao, F., et al.: Diffusion mechanism of lithium ion through basal plane of layered graphene. J. Am. Chem. Soc. 134, 8646–8654 (2012)
- Fan, X., Zheng, W.T., Kuo, J.-L.: Adsorption and diffusion of Li on pristine and defective graphene. ACS Appl. Mater. Interfaces 4, 2432–2438 (2012)
- Cussler, E.L.: Diffusion: mass transfer in fluid systems. Cambridge Series in Chemical Engineering. Cambridge University Press, Cambridge (1997)
- 21. Magerl, A., Zabel, H., Anderson, I.S.: In-plane jump diffusion of Li in LiC<sub>6</sub>. Phys. Rev. Lett. **55**, 222–225 (1985)
- Kim, H.J., et al.: Li diffusion in stage 2 Li-graphite intercalation compounds studied with quasielastic neutron scattering. In: Bernier, P., Fischer, J.E., Roth, S., Solin, S.A. (eds.) Chemical Physics of Intercalation II. NATO ASI Series. Series B: Physics, vol. 305, pp. 355–360. Springer Science+Business Media, New York, USA (1993)
- 23. Jungblut, B., Hoinkis, E.: Diffusion of lithium in highly oriented pyrolytic graphite at low concentrations and high temperatures. Phys. Rev. B 40, 10810–10815 (1989)
- 24. Mandeltort, L., Yates, J.T.: Rapid atomic Li surface diffusion and intercalation on graphite: a surface science study. J. Phys. Chem. C 116, 24962–24967 (2012)

# Appendix A

# **Notes on the Tight-Binding Approach**

Following a tight-binding approach, the band energies  $E_j$  in single layer graphene and bilayer graphene can be calculated by solving the secular equation

$$\det(H - E_i S) = 0, (A.1)$$

where H and S are the transfer and overlap integral matrices of the system, respectively, and det is the determinant of the matrix.

For single layer graphene (SLG) [1, 2],

$$H_{\text{SLG}} = \begin{pmatrix} \epsilon_A & -\gamma_0 f(\mathbf{k}) \\ -\gamma_0 f^*(\mathbf{k}) & \epsilon_B \end{pmatrix} \quad \text{and} \quad S_{\text{SLG}} = \begin{pmatrix} 1 & s_0 f(\mathbf{k}) \\ s_0 f^*(\mathbf{k}) & 1 \end{pmatrix} \quad (A.2)$$

where

$$f(\mathbf{k}) = \sum_{l=1}^{3} e^{ik\delta_l} = e^{ik_y a/\sqrt{3}} + 2e^{-ik_y a/2\sqrt{3}} \cos(k_x a/2), \tag{A.3}$$

describes nearest-neighbor hopping and  $\epsilon_A = \epsilon_B = 0$  for intrinsic graphene.  $\gamma_0$  parametrizes nearest-neighbor hopping and  $s_0$  parametrizes the overlap between orbitals on adjacent sites.

For bilayer graphene (BLG), the transfer integral matrix can be written as [2]

$$H_{\text{BLG}} = \begin{pmatrix} \epsilon_{A1} & -\gamma_0 f(\mathbf{k}) & \gamma_4 f(\mathbf{k}) & -\gamma_3 f^*(\mathbf{k}) \\ -\gamma_0 f^*(\mathbf{k}) & \epsilon_{B1} & \gamma_1 & \gamma_4 f(\mathbf{k}) \\ \gamma_4 f^*(\mathbf{k}) & \gamma_1 & \epsilon_{A2} & -\gamma_0 f(\mathbf{k}) \\ -\gamma_3 f(\mathbf{k}) & \gamma_4 f^*(\mathbf{k}) & -\gamma_0 f^*(\mathbf{k}) & \epsilon_{B2} \end{pmatrix}, \tag{A.4}$$

where  $\gamma_0, \dots \gamma_4$  follow the notation of Slonczewski, Weiss, and McClure [3, 4], and where

$$\epsilon_{A1} = \frac{1}{2}(-U + \delta_{AB}),\tag{A.5}$$

$$\epsilon_{B1} = \frac{1}{2}(-U + 2\Delta' - \delta_{AB}),\tag{A.6}$$

$$\epsilon_{A2} = \frac{1}{2}(U + 2\Delta' + \delta_{AB}),\tag{A.7}$$

$$\epsilon_{B2} = \frac{1}{2}(U - \delta_{AB}). \tag{A.8}$$

Here, U is the interlayer asymmetry,  $\Delta'$  describes the energy difference between dimer and non-dimer sites, and  $\delta_{AB}$  accounts for an energy difference between the sublattices A and B on each layer.

Within the simplified description of the bilayer graphene electronic states, introduced in Sect. 2.2, one can derive an expression for the density of states (DOS) [5]

$$DOS(E) = \frac{g_v g_s}{2\pi\gamma^2} \left[ \frac{\gamma_1}{2} + E + \Theta(E - \gamma_1) \left( E - \frac{\gamma_1}{2} \right) \right]$$
(A.9)

where  $\Theta$  is the Heaviside step function,  $\gamma = \sqrt{3}a\gamma_0/2$ ,  $g_s = 2$  is the spin degeneracy, and  $g_v = 2$  is the valley degeneracy.

#### References

- 1. Wallace, P.R.: The band theory of graphite. Phys. Rev. 71, 622 (1947)
- McCann, E., Koshino, M.: The electronic properties of bilayer graphene. Rep. Prog. Phys. 76, 056503 (2013)
- 3. Slonczewski, J.C., Weiss, P.R.: Band structure of graphite. Phys. Rev. 109, 272 (1958)
- 4. McClure, J.W.: Theory of diamagnetism of graphite. Phys. Rev. 119, 606 (1960)
- Ando, T.: Bilayer graphene with long-range scatterers studied in a self-consistent Born approximation. J. Phys. Soc. Jpn. 80, 014707 (2010)